Laser applications to the characterization of semiconductor nanostructures: Coherent control and spin dynamics of elementary electronical excitations

By

Atef GADALLA ABDALLA

Dissertation submitted to

University of Strasbourg, France

For the degree of

Ph.D. in Physics

(Docteur de l'Université de Strasbourg)

Jury Committee

Prof. Dr. Bernd HÖNERLAGE	Thesis director
Prof. Dr. Jan VALENTA	External referee
Prof. Dr. Jean OBERLE	External referee
Prof. Dr. Philippe TUREK	Internal referee
Dr. Mathieu GALLART	Invited

Institut de Physique et Chimie des Matériaux de Strasbourg (IPCMS)
Département d'Optique ultrarapide et de Nanophotonique (DON)

(2010)

Acknowledgements

First and foremost I want to thank my parents, my wife, my brothers and sisters who always supported me during the years of my studies.

Special thanks go to my supervisor Prof. Dr. ***Bernd HÖNERLAGE****, who invested a lot of time into this work and into all the discussions to understand the results and he always had an open ear for all my questions.*

The author would like to thank Dr. ***Pierre GILLIOT****, for suggesting the point of research, fruitful discussion, guidance and support through the work of this thesis and also for his personal advices and helps.*

I am very grateful to Dr. ***Mathieu GALLART****, for his appreciated help for the measurements and analysis of the GaN/AlGaN QW part and for his advices through the thesis work.*

It gives me great pleasure to express my deep thanks to Eng. ***Olivier CREGUT****, for his continuous help and guidance during the experimental part of this work.*

Thanks to the members of Groupe d'Optique Nonlinéaire et Optoélectronique (DON) at IPCMS; Dr. ***Christelle BRIMONT****, Eng.* ***Marc ZIEGLER****,* ***Jean BESBAS****,* ***Bertrand kei YUMA,*** *and* ***Thomas GELOT****, thank you for the good time.*

Thanks to my friends and colleagues who encouraged me during the work of this thesis; Dr. ***Anwar KIDDIS****, Dr.* ***Noshi WAHBA****, Dr.* ***Mansour BEKHIT****, Dr.* ***Cherif YOUSSEF****, Dr.* ***Ihab ATTALAH****,* ***Amani ZAGDOUD****, and* ***Walid BAAZIZ****.*

Further I want to thank Dr. ***Eric BEAUREPAIRE****, Dr.* ***Martin BOWEN*** *and* ***Jean-Baptiste BEAUFRAND****, DMONS-IPCMS, for the preparation of Phthalocyanine (Pc) thin films, Dr.* ***Samy BOUKARI*** *for the preparation of Pc in solution form and useful discussion for the structural analysis of the prepared films.*

I would also like to thank Dr. ***Guillaume ROGEZ*** *for optical measurements of the Pc films, Dr.* ***Guy SCHMERBER*** *for the XRD measurements, Eng.* ***Jacques FAERBER*** *for SEM analysis, Eng.* ***Gilles VERSINI*** *, Eng.* ***Sophie BARRE*** *for the AFM analysis and Eng.* ***Dominique QUINCE*** *for his appreciated help when I had a software problem in my computer.*

The author would like to thank Dr. ***Martin BRINKMANN****, ICS-UdS, for the TEM measurements and helpful discussion.*

Finally, I would like to take this opportunity to express my deep gratitude and appreciation to the ***Egyptian ministry of high education*** *and* ***NILES*** *at Cairo University in Egypt for their support to get the grant for my PhD in Strasbourg, France.*

Preface

The main work in this thesis has been carried out at the laboratory of the Department of Ultrafast Optics and Nanophotonics (DON), Institute of Physics and Chemistry of Materials in Strasbourg (IPCMS), University of Strasbourg, France.

List of publications:

+ Atef Gadalla, Olivier Crégut, Mathieu Gallart, Bernd Hönerlage, Jean-Baptiste Beaufrand, Martin Bowen, Samy Boukari, Eric Beaurepaire, and Pierre Gilliot ¨ **Ultrafast Optical Dynamics of Metal-Free and Cobalt Phthalocyanine Thin Films**¨ *J. Phys. Chem. C, 114, 4086 (2010).*

+ Christelle Brimont, Mathieu Gallart, Atef Gadalla, Olivier Crégut, Bernd Hönerlage, and Pierre Gilliot ¨ **Dislocation density and band structure effects on spin dynamics in GaN**¨ *J. Appl. Phys., 105, 023502 (2009).*

Publications in Progress:

+ Atef Gadalla, Jean-Baptiste Beaufrand, Martin Bowen, Samy Boukari, Eric Beaurepaire, Olivier Crégut, Mathieu Gallart, Bernd Hönerlage, and Pierre Gilliot ¨**Ultrafast optical dynamics of metal free and cobalt phthalocyanine thin films II: Study of excited states dynamics**¨. Submitted to "*Journal of Physical Chemistry C* " accepted (Sept. 2010)

+ A. Gadalla, J. Besbas, M. Gallart, O. Crégut, B. Hönerlage, and P. Gilliot ¨ **Spin relaxation of free excitons in narrow GaN/AlGaN quantum wells**¨. Submitted for publication to "*Physical Review B* " (2010)

Publications not included in the thesis:

+ Sylvie Bégin-Colin, Atef Gadalla, Gérard Le Caër, Olivier Humbert, Fabien Thomas, Odile Barres, Frédéric Villiéras, Laura F. Toma, Ghislaine Bertrand, Orfan Zahraa, Mathieu Gallart, Bernd Hönerlage, Pierre Gilliot ¨ **On the Origin of the Decay of the Photocatalytic Activity of TiO_2 Powders Ground at High Energy** ¨ *J. Phys. Chem. C, 113, 16589 (2009).*

Résumé

Cette thèse aborde des problématiques de physique des excitations élémentaires dans la matière condensée dans le contexte de la spintronique. En utilisant la spectroscopie optique résolue en temps, nous étudions la dynamique des populations ainsi que l'orientation optique des états électroniques excités dans des semiconducteurs sous forme de film minces et de nanostructures. Un premier sujet concerne des matériaux semiconducteurs organiques (Phthalocyanines) sous forme de couches minces sur substrats de silice fondue, préparés par la technique d'évaporation thermique sous ultravide. Un deuxième travail étudie la dynamique de relaxation de spin des excitons dans un puits quantique (QW) de GaN/AlGaN, préparé par épitaxie en phase vapeur d'organométalliques (EPVOM) sur un substrat de saphir. Nous appliquons une technique pompe-sonde résolue en temps et spectralement, à l'aide d'une source laser femtoseconde (fs) Ti: Saphir accordable en fréquence.

Les propriétés structurales des films de phtalocyanine (H_2Pc) sans incorporation de métal et de phtalocyanine de cobalt (CoPc) de 170 nm d'épaisseur ont été étudiées. Les mesures basées sur la diffraction des rayons X, la microscopie électronique à balayage et la microscopie à force atomique ont indiqué que les deux types de films sont polycristallins avec la même granularité moyenne et qu'ils ont une structure orthorhombique de phase (α). L'absorption optique linéaire des films de H_2Pc et CoPc présente plusieurs bandes de forte absorption. La bande (Q), dans la région visible, possède deux composantes. Elles sont attribuées à la première transition π-π^* du macrocycle de la phthalocyanine. Les bandes d'absorption de l'échantillon CoPc sont décalées d'environ 20-30 meV vers les hautes énergies par rapport à l'échantillon H_2Pc. Dans la région UV, la bande de Soret (bande B) est située autour de 3,756 eV et la bande (N) à 4,426 eV pour CoPc et similairement pour H_2Pc.

En utilisant des impulsions laser femtoseconde avec une durée de 70 fs et une largeur spectrale de ~ 26 meV, nous avons d'abord effectué des expériences pompe-sonde dégénérées à une énergie de photon de 2,066 eV qui se trouve dans la bande (Q). Nous avons d'abord mesuré l'intensité des impulsions sondes transmises par l'échantillon, avec et sans excitation par l'impulsion pompe, en fonction de l'énergie des photons de la

sonde. À partir de ces données, nous avons calculé la transmission différentielle ($\Delta T(t)/T$) en fonction du retard (t) entre la pompe et la sonde [Gadalla10]. Ces valeurs expérimentales ont été ajustées en utilisant une fonction qui inclut une contribution constante et une décroissance exponentielle simple pour le H_2Pc et une décroissance bi-exponentielle dans le cas de la CoPc. Nous constatons que les états excités du H_2Pc relaxent *via* deux processus : un processus lent sur une échelle de temps de quelques dizaines de picosecondes (ps) et un processus très lent avec un temps caractéristique de plusieurs centaines de ps (considéré comme constante à l'échelle de temps de notre expérience). Cependant, les états excités de la CoPc relaxent beaucoup plus rapidement grâce à plusieurs processus : un processus ultra-rapide sur une échelle de temps fs, un rapide (sur une échelle ps), et un dernier avec une durée de vie de population plus longue de l'ordre de quelques centaines de picosecondes. Nous avons également étudié $\Delta T(t)/T$ à des intensités d'excitation différentes à l'énergie de photon de 2,066 eV (600 mn) afin d'identifier l'origine de l'augmentation du taux de relaxation dans le cas de CoPc. Les résultats montrent que le maximum de signal de $\Delta T(t)/T$ varie linéairement en fonction de l'intensité d'excitation [Gadalla10]. Ceci indique que l'intensité du faisceau de pompe n'est pas suffisamment élevée pour donner lieu à des collisions exciton-exciton observées dans d'autres films de métal-phthalocyanines [Mi03, Zhou04].

Pour obtenir un aperçu plus clair de la dynamique de relaxation des films de H_2Pc et de CoPc, nous avons réalisé une expérience pompe-sonde non-dégénérée avec des énergies d'excitation par la pompe de 1,823 eV et 2,032 eV, qui correspondent aux deux maxima d'absorption de la bande (Q). En utilisant la sonde, on effectue des mesures spectrales (de 1,57 eV à 2,47 eV) de la transmission différentielle $\Delta T(t)/T$ en fonction du retard entre les impulsions pompe et sonde (0-50 ps). Nous avons observé que, en fonction de la position spectrale sondée, la transmission différentielle passe d'une saturation d'absorption à une absorption induite pour les films de H_2Pc ainsi que pour les films de CoPc. De plus, l'introduction de cobalt dans la molécule de phthalocyanine conduit à la création de nouvelles voies de relaxations efficaces et favorise une relaxation très rapide des états excités. Nous attribuons la dynamique ultrarapide observée, par rapport aux films H_2Pc, à la présence des atomes de Co, qui peuvent coupler les molécules planaires à l'intérieur du film mince et donner lieu à des processus efficaces de transfert de charge (CH). En outre, lorsqu'on excite à 2,032 eV (610 nm), nous observons autour de l'énergie de photon de la pompe une résonance de type Fano [Fano61], observable sur une échelle de temps de plusieurs dizaines de ps. Elle est attribuée à la présence d'un continuum d'états d'excitons à transfert de charge qui est dégénéré avec la bande inhomogènement élargie des excitons moléculaires, qui forment la bande (Q) et sont excités en résonance. Les deux systèmes sont fortement couplés dans le cas de la CoPc ce qui modifie les transitions optiques dans le voisinage de l'énergie de photon du laser [Gadalla10a].

La deuxième partie de notre travail est une étude de la dynamique de relaxation des excitons polarisés en spin dans un puits quantique étroit de GaN/AlGaN wurtzite de haute qualité. Nous avons effectué des expériences pompe-sonde résolues en temps [Gadalla10b]. Le spectre de réflectivité linéaire peut se diviser en trois régions différentes: des structures à 3,49 eV sont liées aux excitons (A et B) dans la couche tampon de GaN, deux structures (le premier trou lourd HH_1 et le trou léger LH_1) caractéristiques des excitons du puits quantique, sont centrées à 3,54 eV et la troisième région est due à la barrière AlGaN. Le spectre d'excitation de la photoluminescence (PLE) enregistré à l'énergie de photoluminescence (PL) de l'exciton HH_1 présente les signatures des excitons HH_1 et LH_1 ainsi que celui de la barrière. Ceci révèle qu'il n'y a pas d'états excitoniques supplémentaires confinés dans le QW.

La durée de vie des excitons a été mesurée en utilisant l'expérience pompe-sonde avec des impulsions linéairement polarisées. Lorsque les excitons sont créés dans la barrière, les signaux du HH_1 et LH_1 présentent un temps de montée caractéristique de la relaxation des excitons depuis la barrière vers le puits quantique tandis que dans le cas d'une excitation résonante du puits ce temps de montée est uniquement limité par la durée de l'impulsion pompe. Dans les deux cas, la décroissance de la PL est mono exponentielle pour les deux excitons HH_1 et LH_1 avec une constante de temps égale à 230 ps.

Lorsque l'échantillon est excité par des impulsions pompe circulairement polarisées, le remplissage des états dans l'espace des phases est responsable d'un signal non-linéaire. L'amplitude de ce signal doit dépendre de la polarisation de la sonde. Le spectre de réflectivité différentielle $(\Delta R(\omega)/R(\omega))$ pour les deux hélicités possibles de la sonde est mesuré simultanément pour chaque retard pompe-sonde. L'amplitude de

ΔR(ω)/R(ω) pour les deux résonnances excitoniques dépend de l'hélicité de la sonde comme attendu dans le cas où la population d'exciton est effectivement polarisée en spin. La différence entre les deux spectres disparaît à plus grand retard pompe-sonde. *ΔR(ω)/R(ω)* montre une structure à 10 meV en dessous de la résonance excitonique HH_1. Celle-ci peut être attribuée à une transition induite exciton-biexciton [Stokker08]. En configuration $\sigma^+\sigma^-$ le signal atteint un maximum après un temps de montée de 0,8 ps. Pour une séquence d'impulsions de polarisation $\sigma^+\sigma^+$, il augmente progressivement tandis le signal dans la configuration $\sigma^+\sigma^-$ diminue. Les deux signaux s'égalisent après 4 ps. Selon les règles de sélection optique, la création d'un biexciton à partir d'un exciton $|+1>_{HH1}$ peut être fait par l'absorption d'un photon de sonde σ^- ou par un processus de retournement du spin suivi par l'absorption d'un photon σ^+. Par conséquent, le signal *ΔR(t)/R* pour la sonde σ^+ (σ^-) est proportionnel à la population de l'état excitonique |-1> (|+1>). L'évolution temporelle de ces signaux prouve que la population excitonique $|+1>_{HH1}$ alimente directement l'état $|-1>_{HH1}$ via le retournement simultanée des spins de l'électron et du trou. Autrement dit, le mécanisme prépondérant dans la dynamique de relaxation de spin est le retournement en bloc du spin de l'exciton [Soleimani04]. Ce temps est caractéristique d'excitons libres qui relaxent leur pseudo-spin sur une échelle de quelques ps tandis qu'une petite partie des excitons localisés conserve son orientation optique pendant un plus long délai.

Des fonctions *ΔR(t)/R* intégrées spectralement ont été mesurés pour des intensités différentes d'excitation par la pompe et nous avons observé qu'il n'y a pas de changement dans la dynamique du taux de polarisation circulaire en fonction de la densité des excitons. Seule la valeur initiale du taux de polarisation est affectée, montrant que les collisions exciton-exciton ne sont pas responsables de la relaxation de spin. Le taux de polarisation circulaire du signal de réflectivité différentielle pour l'exciton HH_1 atteint 80% quand il est excité en résonance. Cette valeur est plus élevée que dans le matériau massif (~ 50% dans le cas du meilleur échantillon de la ref. [Brimont09]) et diminue en quelques ps. C'est l'indication que, même si les excitons sont confinés dans la direction de croissance, leur propagation dans le plan du puits quantique les rend très sensibles aux processus de collision qui sont responsables du déphasage des excitons et, par conséquent, de la relaxation de spin. Des expériences en fonction de la température de l'échantillon ont montré que la relaxation de spin présente une forte dépendance en température. La durée de vie du spin reste pratiquement constante jusqu'à 80 K, puis décroît rapidement. Ceci pourrait être due à une fuite thermique des excitons depuis le puits quantique de GaN vers la barrière d'AlGaN donnant lieu à une relaxation du spin. Toutefois, par rapport à GaN massif, l'orientation optique est conservée jusqu'à 100 K.

Thesis Abstract

This thesis addresses important topics in the field of spintronics by using time resolved spectroscopy techniques. We study the population dynamics and optical orientation of excited electronic states in semiconductors thin films and nanostructures. One subject concerns the phthalocyanine, an organic compound semiconductor, in thin film form prepared by thermal evaporation technique under ultra high vacuum on fused silica substrates. A second work studies the spin relaxation dynamics of free excitons in a narrow GaN/AlGaN quantum well, grown by metal organic vapour phase epitaxy (MOVPE) on *c*- plane sapphire substrate. We apply a temporally and spectrally resolved femtosecond (fs) pump-and-probe technique using a tuneable Ti: Sapphire laser source.

Structural properties of metal-free phthalocyanine (H_2Pc) and cobalt phthalocyanine (CoPc) films of the same thicknesses (~ 170 nm) have been studied. X-ray diffraction, scanning electron microscopy and atomic force microscopy measurements indicate that both types of films are polycrystalline with nearly the same average grain size and that they have orthorhombic α-phase structure. Optical linear absorptions of H_2Pc and CoPc films present several strong absorption bands. The Q- band in the visible region is split into two components and this is attributed to the first π–π^* transition on the phthalocyanine macrocycle. The absorption bands of the CoPc sample are shifted by about 20-30 meV to higher energies with respect to the H_2Pc sample. In the near UV region, the Soret band (B- band) shows up around 3.756 eV and the N- band shows up at 4.426 eV for CoPc and similarly for H_2Pc.

Using femtosecond laser pulses with pulse duration close to 70 fs and a spectral width ~ 26 meV, we first performed degenerate pump-and-probe experiments exciting at a photon energy of 2.066 eV, which lies in the Q- absorption band. We first measure the transmitted intensity of the probe pulses with and without exciting the sample by the pump pulses as a function of probe photon energy. We then calculate the differential transmission rate ($\Delta T(t)/T$) as a function of time delay (t) between the pump and probe pulses [Gadalla10]. By fitting the experimental data of the differential transmission using a constant contribution and a single exponential decay fit for the H_2Pc and a double exponential decay for the CoPc, we find that the excited states for H_2Pc film decay through two processes: a slow process on a time scale of tens of picoseconds (ps) and a very slow process with a recovery time of several hundreds of ps (giving rise to the constant contribution on the experimental time scale). On the contrary, the excited states of CoPc decay much faster through several processes: an ultrafast process on a fs time scale, a fast one (on a ps time scale), and a long-living population with recovery time of hundreds of picoseconds. We have also studied the $\Delta T(t)/T$ at different excitation intensities in order to identify the origin of the increase of the relaxation rate in the case of CoPc at photon energy 2.066 eV (600 nm). The results show that the peak signal of $\Delta T(t)/T$ varies linearly as a function of the excitation intensity [Gadalla10]. This indicates that the intensity of the pump beam is not high enough to give rise the exciton-exciton interaction as observed in other metal phthalocyanine films [Mi03, Zhou04].

To get a closer insight into the relaxation dynamics of both H_2Pc and CoPc, we performed a non-degenerate pump-and-probe experiment with excitation pump at photon energies 1.823 eV and 2.032 eV, which correspond to the two absorption maxima of the Q- band. By using the probe beam, we measure the spectrally (in the range from 1.570 eV to 2.470 eV) resolved differential transmission $\Delta T(t)/T$ as a function of the time delay between the pump and the probe pulses (0-50 ps). We observed that the differential transmission rate varies from absorption bleaching to induced absorption for both H_2Pc and CoPc depending on the spectral position of the probe beam. In addition, the introduction of cobalt into the phthalocyanine molecules leads to the creation of new efficient relaxation channels for the electronic excitations and enhances the relaxation very rapidly after the pump pulse for CoPc. We attribute the observed ultrafast dynamics, when compared to the H_2Pc films, to the presence of the Co atoms, which may couple the planar molecules within the film and give rise to efficient charge transfer processes. In addition, when exciting at 2.032 eV (610 nm), we observe around the photon energy of the pump beam a Fano-type resonance [Fano61], whose properties evolute on a time scale of several tenths of ps. It is tentatively attributed to the presence of a continuum of charge transfer excitons that is degenerated with the inhomogeneously broadened band of Pc molecular excitons, which form the Q- band and are resonantly excited. Both systems are strongly coupled in CoPc and modify the optical transitions in the vicinity of the laser photon energy [Gadalla10a].

The second part of our work deals with the relaxation dynamics of spin-polarized excitons in a wurtzite high quality narrow GaN/AlGaN quantum well (QW) that we studied by time-resolved pump-and-probe experiments [Gadalla10b]. The linear reflectivity spectrum shows three different regions: sharp structures at 3.49 eV are related to the A- and B- excitons in the GaN buffer layer, two structures (first heavy hole HH_1 and light hole LH_1) characteristic for QW excitons are centered at 3.54 eV above the GaN band gap and the third region is due to the AlGaN barrier which presents a reflectivity signature at 3.59 eV. The photoluminescence excitation (PLE) spectrum, recorded at the HH_1- exciton PL energy, exhibits the signatures of the HH_1 and LH_1 excitons as well as that of the barrier and reveals that no additional confined excitonic states are present in the QW.

The exciton lifetime has been measured by using the pump-and-probe setup with linearly polarized beams. When the excitons are created in the barrier, the HH_1 and LH_1 signals present a rise time characteristic of the relaxation from the barrier towards the quantum well while in the case of resonant excitation, the risetime is nothing more than the duration of the pump pulse. Whatever the excitation conditions (resonant or non-resonant), the decay is monoexponential for both HH_1 and LH_1 excitons with a time constant equal to 230 ps.

When exciting the sample with circularly polarized pulses, phase space filling is responsible for a non-linear response of the sample. This non-linear signal is expected to depend on the probe polarization. The differential reflectivity spectra ($\Delta R(\omega)/R(\omega)$) for the two different probe helicities are measured simultaneously at different pump-probe delays. At the excitonic resonances, the amplitude of $\Delta R(\omega)/R(\omega)$ depends on the probe helicity as a consequence of optical orientation of excitons. This difference disappears at longer time delays. $\Delta R(t)/R$ shows a feature about 10 meV below the HH_1 excitonic resonance. This is characteristic of an induced exciton-biexciton transition in the GaN QW [Stokker08]. The corresponding signal reaches a maximum in the $\sigma^+\sigma^-$ configuration after a risetime of ~ 0.8 ps. For a $\sigma^+\sigma^+$ polarization sequence, it progressively increases when the $\sigma^+\sigma^-$ $\Delta R(t)/R$ signal decreases. The two signals are equal after 4 ps. According to the optical selection rules, the creation of a biexciton starting from a $|+1>_{HH1}$ exciton can be done by the absorption of a σ^- probe photon or by a spin-flip process followed by the absorption of a σ^+ photon. Consequently, the *ΔR(t)/R* signal for σ^+ (σ^-) probe is proportional to the |-1> (|+1>) population, respectively. The time decays evidence that the $|+1>_{HH1}$ excitonic population directly feeds the $|-1>_{HH1}$ pseudo-spin state via a simultaneous spin-flip of electron and hole. This indicates that the time needed for the two signals to be equalled corresponds to the relaxation time of the exciton spin as a whole [Soleimani04]. It can be mainly attributed to originate from free excitons that relax their pseudo-spin within a few ps while only a small portion of localized excitons keeps its optical orientation on a longer timescale.

Spectrally integrated *ΔR(t)/R* functions were measured for different excitation pump intensities. We have observed that there is no change in the dynamics for the circular polarization rate as a function of exciton density, but only the initial value of the polarization rate depends on the excitation intensity. We conclude that exciton-exciton collisions are not responsible for the spin relaxation. The circular polarization rate of the differential reflectivity signal for the HH_1 exciton reaches 80% when it is resonantly excited which is larger than that in bulk material (~ 50% in the case of the best sample of ref. [Brimont09]) and it decays on a few ps timescale. This is an indication that, even if the excitons are confined in the growth direction, their propagation in the well plane makes them very sensitive to scattering processes which are responsible for exciton dephasing and, therefore, for an efficient spin-relaxation. The spin relaxation presents also a strong temperature dependence. The spin lifetime remains almost constant up to 80 K and then decreases rapidly. This can be due to a thermal escape of excitons from the well towards the AlGaN barrier, giving rise to spin relaxation. In contrast to bulk GaN, however, the optical orientation is preserved up to 100 K.

Contents

1.0 Introduction

1.1 Introduction……………………………………………………………….1
1.2 Outline of the thesis ……………………………………………………….3

2.0 Material Description

2.1 Phthalocyanine (Pc)………………………………………………………7
  2.1.1 Orbital states of transition metal phthalocyanine molecules……………….8
  2.1.2 Sample preparation……………………………………………………...10
    2.1.2.a Purification of organic molecules………..…………...…………...10
    2.1.2.b Deposition of thin film...………………………………...…........11
    2.1.2.c Phthalocyanine samples……..………..………………………..…...12

2.1.3 Film characterization

    2.1.3.a Structural study of thin films..………..………………………..…....12
      (a) X-ray diffraction (XRD)..………..……………………….….......12
      (b) Scanning electron microscopy (SEM)….……………………...13
      (c) Atomic force microscopy (AFM)……….………….……….…13
      (d) Transmission electron microscopy (TEM)..…………………….…14
    2.1.3.b Optical study of thin films………..……………....……….…..….......14
      (a) Uv-Vis absorption and reflection…….…………………...…....14

2.2 Gallium Nitride (GaN)

  2.2.1 Crystallographic structure……………………………..……………..…15
    2.2.1.a Cubic GaN ……………………………….……….……….…….17
    2.2.1.b Hexagonal GaN.………………………….……….……….….…18
  2.2.2 Excitons…………………………………………….……….……….…21
  2.2.3 Quantum Well (QW)….………………………………….……….…….…..23

2.2.4 Exciton fine structure in QW……………………….……….…….….……24

2.2.5 Optical selection rules…………………………….……….…….…………25

2.2.6 Reflectivity .………………………………………….…….…….………..26
2.2.6.a Differential reflectivity.……………………………….…….….……28

2.2.7 Spin relaxation…………………………………….…….…….………..29
2.2.7.a Spin relaxation mechanisms…………………………..………..30

3.0 General Experimental Methods

3.1 Pump-probe spectroscopy……………………….…….…….….…......33
3.1.1 Transmission / Reflection spectroscopy….……..………………………..34

3.2 Laser sources……………………………….……………………………34
3.2.1 Femtosecond laser oscillator with a regenerative amplifier ……………..35
3.2.1.a Diode-pumped laser ……..……………………….……………......35
3.2.1.b Laser oscillator…...……….……………………….…………...36
3.2.1.c Regenerative amplifier (RegA)..…………………….…………..36
3.2.1.d Optical parametric amplifier (OPA).……………….…………...38

3.3 Group velocity dispersion compensation.……………….…………....39

3.4 Temporal and spectral characterization of laser pulses….…………....40

3.5 Cryostat.……..………………………….……………..……….....43

3.6 Photoluminescence excitation spectroscopy (PLE) spectroscopy...…..44

3.7 Experimental setup for measuring differential transmission of phthalocyanine films……………………..…….………………..45

3.8 Experimental setup for measuring differential reflectivity of GaN/AlGaN QW……………..……………..……………………..46

4.0 Results and discussion (part I): Phthalocyanine Films

4.1 Structural parameters……………………………………………………..50

4.1.1. X-Ray diffraction (XRD)………………………………………………50

4.1.2. Scanning electron microscopy (SEM)……………………………………52

4.1.3. Atomic force microscopy (AFM)…………………………………………52

4.1.4. Transmission electron microscopy (TEM)………………………………..52

4.2 Optical parameters……………………………………………………..54

4.2.1 Linear absorption and reflection spectra……………………………….....54

4.3 Pump-and-probe measurements……………………………………………..57

4.3.1 H_2Pc: Pump photon energy at 1.823 eV……………………………………63

4.3.2 H_2Pc: Pump photon energy at 2.032 eV……………………………………..65

4.3.3 CoPc: Pump photon energy at 1.823 eV……………………………………...67

4.3.4 CoPc: Pump photon energy at 2.032 eV……………………………………...70

4.4 Comparison between H_2Pc and CoPc relaxation dynamics…………..72

4.5 Conclusion (Part I)……………………………………………………………78

5.0 Results and discussion (Part II): GaN/AlGaN Quantum Well

5.1 Sample characteristics………………………………………………………..85

5.1.1 Linear spectroscopy…………………………………………………………..85

5.1.2 Photoluminescence excitation spectroscopy (PLE)…………………………88

5.2 Exciton lifetime…………………………………………………………………...91

5.3 Introduction to spin dynamics measurements…………………………….92

5.3.1 Principle of the polarized pump-probe experiment………………………...92

5.3.2 Four level exciton model ……………………………………………………94

5.3.3 The role of biexcitons…. ……………………………………………………95

5.4 Optical orientation experiments ……………………………………………...96

5.4.1 Differential reflectivity spectra………………………………………………96

5.4.2 Model for the amplitude of the ΔR/R signals…...……………………..100
5.4.3 Dynamics of the circular degree of polarization…..….………………...101

5.5 Optical orientation using selective excitonic excitation..…………..104
5.6 Power and temperature dependence…..………………………...…....106
5.6.1 Power dependence……………………………………………...…106
5.6.2 Temperature effect……………………………………………..…108

5.7 Discussion…..……..……………………………………………….…111

5.8 Conclusion (Part II)…………………………………………….…114

6.0 General Conclusion……………………………………….………..117

References…………………………………………..…………………...121
List of Abbreviations……………………………..……………………..131
List of Figures………………………..…………………………………...135
List of Tables…………………………..………………………………….140

Chapter
1
Introduction and Thesis Outline

Chapter 1

1.1 Introduction

Semiconductors can be broadly classified into two main groups as organic and inorganic semiconductors. Inorganic semiconductors are used extensively in electronic devices. Now it is expected that the organic semiconductors will be suitable candidates for future electronics as they are widespread and not expensive which makes them good candidates for commercial applications as well as those of inorganic semiconductors like Gallium nitride (GaN) and its related compounds are promising materials for spintronic applications as we will see in the following.

The organic molecule phthalocyanine (Pc) finds potential use in the technological areas due to their high chemical and thermal stability and interesting electronic properties. Several well known devices, such as light-emitting diodes [Tang87, Zhou01, Zhou02], solar-cells [Tang86], field effect transistors [Dimitra02, Collet00], and recordable CD's [Mckeown98] designed entirely on the basis of organic materials have been successfully demonstrated. The metallophthalocyanines (MPcs) family is a versatile class of the metal-organic compounds, which have attracted considerable attention in nano-science and material engineering [Prince01, Ribeiro00].

Furthermore, the large optical nonlinearity of the transition-metal phthalocyanines, arising from their two dimensional conjugated π-electron system, recommends them as candidates for various photonic devices, such as optical switches and optical limiting filters [Collier00, Kornilovich01, Stewart04]. In particular, cobalt phthalocyanine (CoPc) is often used in gas sensing [Gould01] and optoelectronic [Miller06] systems. Additionally, because of the magnetic properties of the Co ion, CoPc is considered for applications as a low dimensional molecular magnet [Harutyunyan95, Harutyunyan99]. A recent study of spin transport across single CoPc molecules has been done by using low-temperature spin-polarized scanning tunneling microscopy (SP-STM) [Iacovita08].

The relaxation mechanisms of photoinduced excitation are one of the most important factors that determine the performance of devices in such applications. Thus, a detailed knowledge of photoexcitation dynamics in MPcs is required in view of their applications in the photonic field. MPcs are very special organic systems in that they offer tremendous opportunities in tailoring their physical and chemical properties over a wide range either by substituting different metal atoms into the phthalocyanine ring or by altering peripheral and axial functionalities of the molecules.

Phthalocyanines can play host to over 70 different metallic and non-metallic ions in its central cavity. It is possible to incorporate a variety of peripheral substituents around the phthalocyanine core as well as to replace some of the isoindole units by other heterocyclic moieties giving rise to different phthalocyanine analogues [Venugopal02]. We are interested in CoPc for its wide range of applications, and we use the metal-free phthalocyanine (H_2Pc) for comparison to study the influence of the 3d Co metal ion on the relaxation dynamics of the thin Pc films.

Wide band gap semiconductors and specifically gallium nitride (GaN) and its related alloys have emerged as one of the most successful systems for optoelectronics in the UV-Visible spectral range. Nowadays, remarkable efforts have been devoted to the understanding of the spin relaxation processes between all excitonic features [Ishiguro07, Brimont08] arising from the valence band splitting due to crystal-field and spin-orbit interactions. GaN has a wide band gap (~3.5 eV) and their weak spin-orbit coupling and large exciton binding energy (~17 meV and ~26 meV in bulk GaN, respectively), enable the manipulation and control of the exciton spin, which makes them promising candidates for spintronic applications.

Aluminium gallium nitride (AlGaN) is a semiconductor material. It is an alloy of aluminium nitride (AlN) and gallium nitride (GaN). AlGaN is used to manufacture light-emitting diodes operating in the blue to ultraviolet region. It is also used in blue semiconductor lasers and in UV radiation detectors. AlGaN is often used together with gallium nitride or aluminium nitride, forming heterojunctions. AlGaN layers can be also grown on sapphire.

Spin relaxation in bulk GaN was investigated by time-resolved spin-dependent pump-and-probe reflectance measurements and by using spectrally resolved four-wave mixing techniques [Ishiguro07]. Exciton-spin dynamics in wurtzite epitaxial GaN has been studied using nondegenerate spectrally and temporally resolved pump-and-probe experiments [Brimont08].

Time-resolved photoluminescence experiments were carried out along the thickness gradient of GaN/AlGaN quantum well (QW) with low Al content (5 %) in the barrier. Well- resolved A- end B- excitonic resonances in the reflectivity spectra of the QW are observed [Stokker08, Stokker09]. A recent work by Brown et al. [Brown08] was devoted to spin dynamics in InGaN/GaN QW and InGaN epilayers. The spin lifetime was shown to lie in the picosecond time scale.

The present work aims to study the relaxation dynamics of both H_2Pc and CoPc thin films, as well as the relaxation dynamics of spin-polarized excitons in a high quality GaN/AlGaN QW by spectrally and temporally resolved nondegenerate pump-and-probe experiments

1.2 Outline of the thesis

Having discussed the goal of this work, we now proceed with a detailed description of the separate six chapters of this thesis. The first chapter gives an introduction to the molecular organic system and the spin relaxation dynamics of GaN/AlGaN QW, which are important subjects in the field of spintronics.

Chapter 2: This chapter is dedicated to material description of phthalocyanine and GaN/AlGaN quantum well samples. Starting with phthalocyanine: Its molecular structure, orbital states of transition-metal phthalocyanines and then sample preparation are first discussed. It follows a description of the deposition method of molecules and of the setup which used for this purposes. Film characterization are performed using different instruments such as X-ray diffraction (XRD), scanning electron microscope (SEM), Atomic force microscope (AFM), transmission electron microscope (TEM), and a double-beam spectrometer for measuring the absorption and reflection of the prepared phthalocyanine films. The basics of these techniques, together with their specific use for the case of molecular systems are briefly presented. Also Gallium Nitride (GaN) characteristics and its crystallographic cubic and hexagonal structures are discussed. Excitons, quantum wells, exciton fine structure in a QW, optical selection rules in hexagonal GaN, reflectivity and finally spin relaxation and its mechanisms are also briefly discussed.

Chapter 3: The experimental approaches of this thesis are discussed in this chapter. We start with an introduction to the pump-and probe spectroscopy and a description of the femtosecond laser source used in our measurements The basic physics and the implementation of this laser system such as: optical parametric amplifier(OPA), group velocity dispersion (GVD), temporal and spectral characterization of laser pulse are discussed. Photoluminescence excitation (PLE) spectroscopy and the setup used for PLE measurements are shown. We describe, in more detail, the experimental setup used for measuring the differential transmission ($\Delta T/T$) for phthalocyanine films, and also the optical setup used for the temporally and spectrally resolved differential reflectivity ($\Delta R/R$) measurements of a GaN/AlGaN quantum well.

Chapter 4: This chapter is devoted to the results and discussion obtained for the metal-free phthalocyanine (H_2Pc) and the Cobalt phthalocyanine (CoPc) samples. Structural measurements by XRD, SEM, AFM, and TEM allow us to characterize the crystallographic phase, grain size and the roughness of both films. Optical parameters have been investigated by measuring the absorption and reflection of the prepared films and compared to those in solution forms to specify in which spectral region it is interesting to excite by the laser source. This chapter discusses also the pump-and probe results by measuring the $\Delta T/T$ variation for a broad absorption band when exciting at two different laser photon energies which lie in the Q- band. We study the relaxation dynamics of the films (H_2Pc and CoPc) by measuring the spectrally and temporally variation for different time delays and probe photon energies, respectively, when exciting at two different photon energies. We compare the relaxation dynamics for both films and introduce a model which describes the induced absorption and induced transmission. Finally, we explain how the metal-ions of CoPc molecules affect the relaxation dynamics when compared to H_2Pc molecules.

Chapter 5: This chapter is dedicated to study the spin-relaxation dynamics of free excitons for a high quality narrow GaN/AlGaN QW. First, we present a sample characterization and a study on the linear reflectivity, photoluminescence (PL) and PLE. We then use the pump-and-probe experimental setup with linearly polarized beams to measure the exciton lifetime. Optical orientation and spin relaxation are also investigated: We present a simple model of three excitonic levels in order to explain the spin dynamics of the photo-created excitons population. By this the temporal evolution of the two excitonic levels ($|+1>$ and $|-1>$) can be measured. Differential reflectivity (*ΔR/R*) spectra, for the same and opposite circular polarizations of the probe pulses with respect to the circularly polarized pump beam, covering the GaN buffer layer and the QW regions are also demonstrated. Before presenting results on the exciton-biexciton transition, which is noticeable 10 meV below the HH_1 excitonic resonance, we show the biexcitons can be created from the excitonic level $|+1>_{HH1}$, by the absorption of a σ^- probe photon. If a spin-flip takes place, this transition can take place by the absorption of σ^+ photon. We have been able to excite selectively the excitonic transition by using pump pulses spectrally filtered through a Fabry-Perot interferometer filter. We also discuss the power and temperature dependences in order to gain more information on the relaxation process.

Chapter 6: The main body of the thesis ends with general conclusion of the thesis work in chapter six, which is then followed by the bibliography, lists of abbreviations, figures and tables.

Chapter
2
Material Description

Chapter 2

Material Description

This chapter includes a description of molecular structure of phthalocyanine (Pc), sample purification and preparation and an introduction to the experimental methods used for structural and optical analysis for the different prepared phthalocyanine (H_2Pc and CoPc) samples and finally a description of crystallographic structure of Gallium Nitride (GaN), GaN/AlGaN quantum wells, optical selection rules and different spin relaxation mechanisms.

2.1 Phthalocyanine (Pc)

The word ¨Phthalocyanine¨ is derived from the Greek terms *naphtha* (rock oil) and *cyanide* (dark blue). The first phthalocyanine was produced accidentally in 1907 by Braun and Tcherniac during a study of the properties of 1, 2-cyanobenzamide. The structure of this metal free, unsubstituted phthalocyanine was determined later by Linstead [Leznoff89].

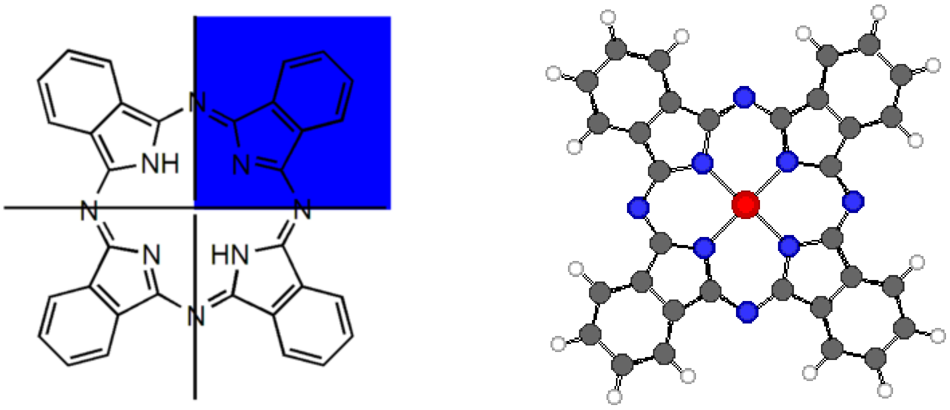

(a) H_2Pc (b) CoPc

Fig. 2.1. *Molecular structure of* (a) H_2Pc *and* (b) CoPc.

The chemical structure of metal free phthalocyanine (H_2Pc) is $C_{32}H_{18}N_8$. H_2Pc molecule is a symmetrical 18 π-electron aromatic macrocycle composed of four isoindole groups, each consisting of a pyrole group coupled to a benzene ring. These four isoindole groups are in turn connected via bridging nitrogen to form a ring-like structure as shown in Fig. 2.1a. The void left in the center of the molecule can be filled with metal atoms, which are strongly bound to the Pc ring and the substituted phthalocyanine molecules with metal atoms are known as metallophthalocyanines (MPcs). The substituted metal in our samples is cobalt and the substituted molecule with cobalt is cobalt phthalocyanine (CoPc) with its chemical structure $C_{32}H_{16}N_8Co$ (see Fig. 2.1b).

The Pc's are characterized by high polarizability and high chemical and thermal stability. The low vapor pressure of the molecules (10^{-14} Torr at room temperature) makes them suitable for sublimation in UHV, allowing a controlled deposition onto the surface in a clean environment. Pc's crystallize by forming molecular stacks where the interaction between molecules is mediated by van der Waals forces [Iwatsu88]. These columns cohere to form a crystal.

The most common polymorph structures of Pcs are α and β, each characterized by a typical angle between the normal to the molecular plan and the stacking direction. A difference in the molecular stacking is associated with a different intermolecular interaction within the stack. This results in a modification of the electronic structure, leading to optical and photoconductive properties that are characteristic for each polymorph [Mizugushi95]. Pc's are reported to be both insulators and semiconductors [Dufour94, Ottaviano97].

2.1.1 Orbital states of transition metal phthalocyanine molecules

Phthalocyanines containing certain transition metals have complex electronic structures because the open (n-1) d- orbitals of the metal may result in a number of energetically close-lying electronic states [Liao01]. Figure 2.2 illustrates the energies of the upper occupied (HOMO) and lower vacant (LUMO) molecular orbitals for the ground states of a group of metal-phthalocyanines.

The HOMO in H_2Pc consists of the π-electrons in the isoindole group, and the LUMO is an excited state of these electrons [Alfredsson05, Orti92]. If the center of the molecule contains a metal atom, the HOMO can be located on the metal (3d) or on the PC ring [Liao01].

CoPc has a complex electronic structure, where the metal $3d_\pi$ -like orbitals lie between the Pc HOMO (a_{1u}) and LUMO ($2e_g$). For such systems, there are extra absorption features that may arise from charge transfer (CT) transitions. The spectra of MPc contain two principal visible region features labeled as Q- band: $a_{1u} \rightarrow 2e_g$ transition and B- bands: $a_{2u} \rightarrow 2e_g$ transitions.

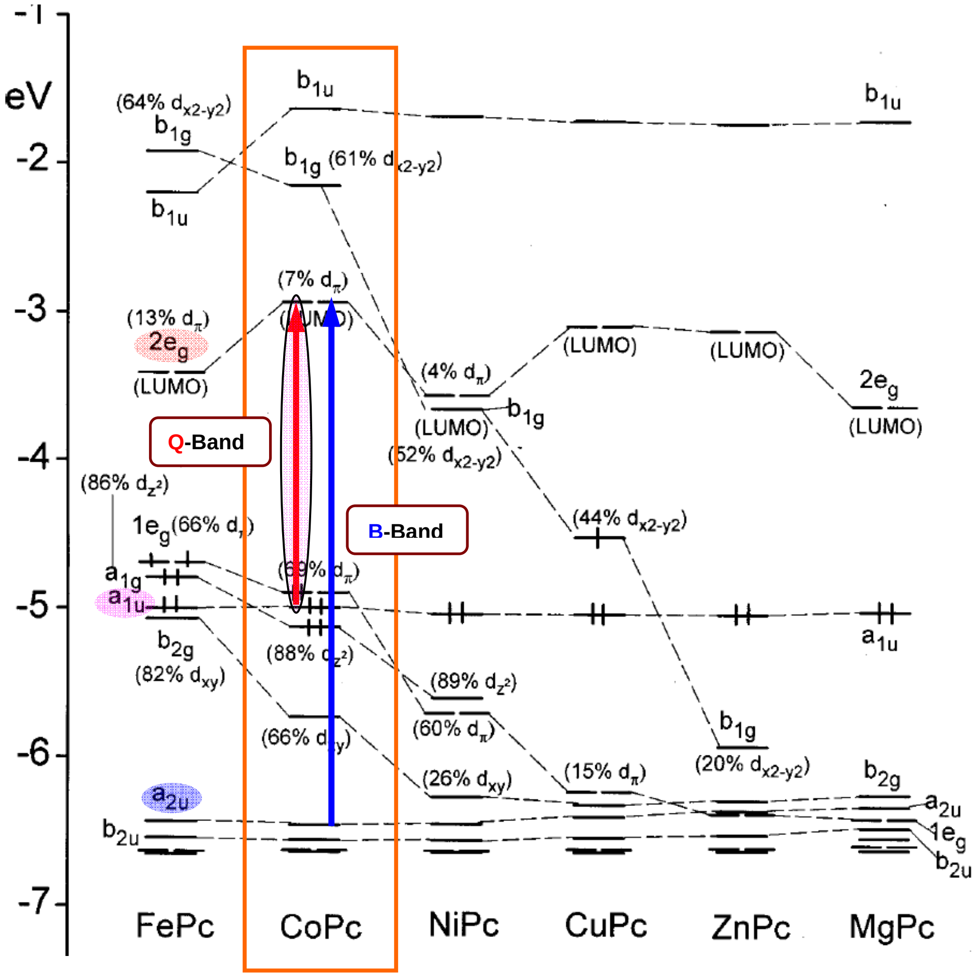
eV
-1
-2
-3
-4
-5
-6
-7
FePc
CoPc
NiPc
CuPc
ZnPc
MgPc
Q-Band
B-Band
b1u
b1g
(64% dx2-y2)
b1g (61% dx2-y2)
(7% dπ)
(LUMO)
(13% dπ)
2eg
(4% dπ)
(52% dx2-y2)
(86% dz²)
1eg (66% dπ)
a1g
a1u
b2g
(82% dxy)
(69% dπ)
(88% dz²)
(66% dxy)
(44% dx2-y2)
(89% dz²)
(60% dπ)
(26% dxy)
(15% dπ)
(20% dx2-y2)
a2u
b2u
1eg

Fig. 2.2. *Orbital energy levels for outer orbitals in different metal-phthalocyanines* [Liao01].

The band between B-and Q- bands has been assigned to a metal-to-Pc-ligand charge transfer (MLCT) or simply (M → L) band from Co e_g to ligand b_{1u} orbital.

Another ligand (Pc) to metal (L → M) CT transition involving $a_{2u} \rightarrow 1e_g$ can occur between the Q- and B- bands.

2.1.2 Sample preparation

This section describes sample preparation methods like purification of the organic molecules (H_2Pc and CoPc) before making thin film deposition under ultra high vacuum. These films are prepared by *DMONS* group at IPCMS.

2.1.2.a Purification of organic molecules

Purification of the source material (organic molecules) is essential for assuring that the grown thin films are reasonably free of impurities. Furthermore, purification is required to prevent the contamination of the prepared films as the insertion of impurities can cause significant problems in the crystals like disturbance to the stacking tendency, reduction in the charge carrier mobility, film disorder etc. Hence, the impurity incorporation rate should be substantially less than the film growth rate.

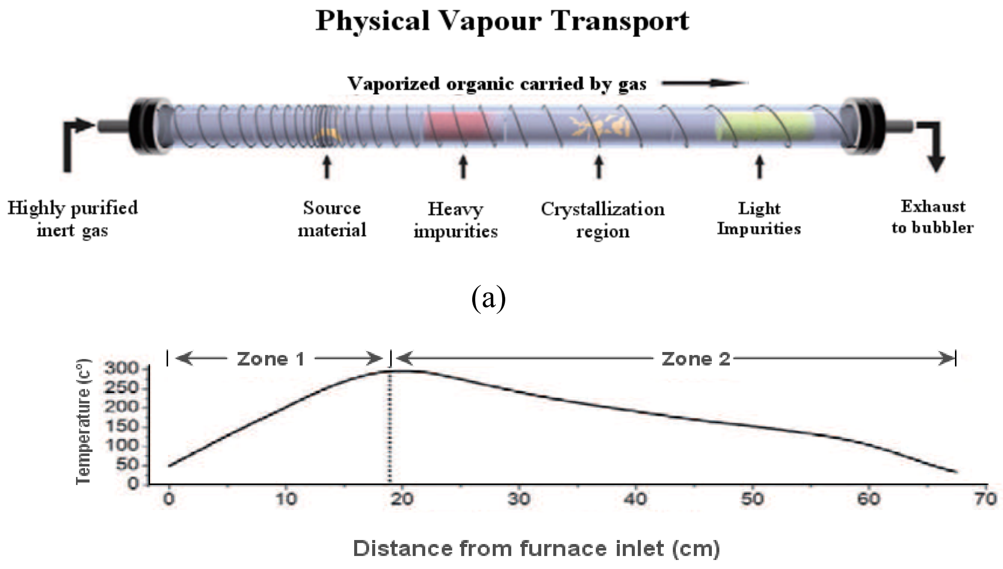
Physical Vapour Transport
Vaporized organic carried by gas
Highly purified inert gas
Source material
Heavy impurities
Crystallization region
Light Impurities
Exhaust to bubbler
Zone 1
Zone 2
Temperature (c°)
300
250
200
150
100
50
0
0
10
20
30
40
50
60
70
Distance from furnace inlet (cm)

(a)

(b)

Fig. 2.3. (a) S*ublimation system setup;* (b) *Temperature distribution along the heated tube.*

The purity of commercial phthalocyanine (H_2Pc, CoPc) in the powder form is 97%, which is not sufficient to make a high optical quality thin layer. The method used to purify it is the sublimation under flow of inert gas [Wagner82]. The sublimation system setup is shown in Fig. 2.3a. The material to be purified is placed into a glass tube, which is approximately 700 mm long and has a diameter of 25 mm. Pyrex glass is sufficient (as sublimation temperature of phthalocyanine is 400 to 500°C), because this type of glass has a softening temperature above 580 °C. The tube is placed into a furnace and arranged to keep the tube in the center of it. The glass tube is isolated from the atmosphere and is circulated with a constant flow of N_2-gas, which improves the heat flow in the glass tube and helps to transport the sublimed vapour towards the cooled end. A good separation of purified materials and non-volatile impurities in the pyrex tube is obtained with a constant temperature gradient along the heated tube, i.e. the temperature drops with the distance from the heater bands as depicted in Fig. 2.3b.

2.1.2.b Deposition of thin films.

In order to make depositions in thin film layers, we use a vacuum chamber under ultra-high vacuum (~ 10^{-9} mbar). The chamber is equipped with two evaporation cells, one for metals (Co in our case) and the other for the organic molecules. The fused silica substrates have to be fixed onto a heater during the deposition in order to control the morphology of the prepared thin films. There is a quartz micro-balance which allows the calibration of the flow of particles emitted by the cell, in order to check the filling duration and to obtain the required film thickness.

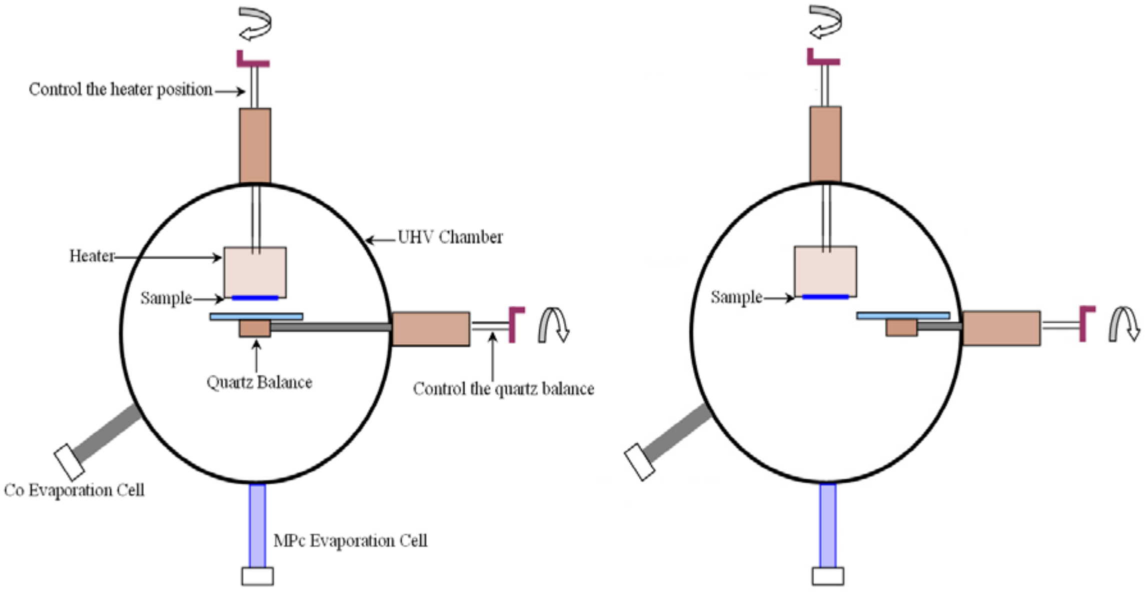

(a) *Calibration position* (b) *Film deposition*

Fig. 2.4. *Schematic diagram of the thermal evaporation technique.*

To avoid film defects, the substrates of suitable dimensions were carefully cleaned using acetone and ethanol. Then the cleaned substrates are inserted into the vacuum chamber and one starts pumping until the vacuum in the chamber reaches the order of 10^{-9} mbar. The first step is the position of calibration (see Fig. 2.4a) by which the temperature of the cells is increasing until a stream of the evaporated material is reached. The second step is to calibrate the flow, to determine the time of filling, depending on the required film thickness. Once the calibration has been done, we switch to the position of film deposition (Fig. 2.4b) for the deposition time necessary.

2.1.2.c Phthalocyanine samples

The fused silica substrates were kept at room temperature during the deposition and the prepared films of H_2Pc and CoPc are of thickness ~170 nm. We prepared also the same molecules in solution form by using 1-Chloronaphthalene as a solvent, in order to compare its optical properties in the Q-band with those in thin film form. We have used 1-Chloronaphthalene solvent because the two molecules (H_2Pc and CoPc) are simply dissolved in it which was not the case when we have used the tetrahydrofuran (THF).

2.1.3 Film characterization

2.1.3.a Structural studies of thin films

(a) X-Ray diffraction (XRD)

X-ray diffraction (XRD) is a technique, which is widely used in many fields of science. However, a brief description of XRD is given in the following; the Bragg-equation: $n\lambda = 2d_{\mathrm{hkl}} \sin(\theta_B)$ relates the lattice spacing (d_{hkl}) of a set of net planes with Miller indices (hkl) to the scattering angle (θ_B) for a certain X-ray wavelength (λ) and n is an integer number determined by the order given. Depending on the measurement geometry the structural order of thin organic films perpendicular and parallel to the film surface can be investigated with XRD. XRD measurements have been performed using a Siemens D5000 apparatus with a monochromatic Cu $K\alpha_1$ (λ= 1.54056 Å) radiation.

(b) Scanning electron microscopy (SEM)

The phthalocyanine samples were characterized with a field emission scanning electron microscope (SEM, JEOL JSM-6700 F) operating with an accelerating voltage of 3 kV to provide information on the morphology of the materials.

(c) Atomic force microscopy (AFM)

Atomic force microscope (AFM) measurements were done using a Veeco Dimension 3100 tapping mode system. Tapping mode AFM operates by scanning a tip attached to the end of an oscillating cantilever across the sample surface and then measuring the force between the sample surface and a sharp probe (see Fig. 2.5a). A probe used in AFM is a sharp tip located at the free end of a flexible cantilever plate. The probe tip interacting with the sample surface is scanned over the surface and the interaction force between the tip and the sample surface causes the cantilever plate to deflect. The deflection of the cantilever is measured by means of a laser beam, which is focused on the cantilever.

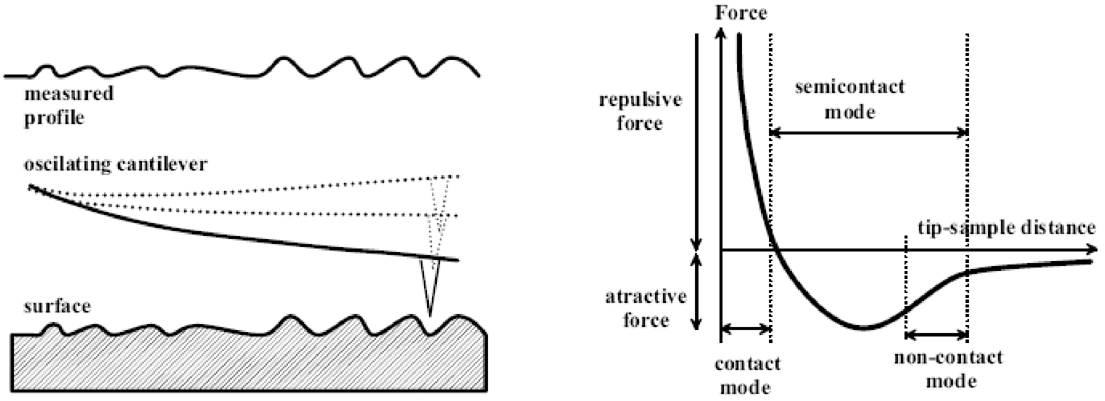
measured profile
oscilating cantilever
surface
Force
repulsive force
atractive force
semicontact mode
tip-sample distance
contact mode
non-contact mode

(a) (b)

Fig. 2.5. (a) *Basic principle of the AFM technique* (b) *Schematic diagram showing the force between the tip and the sample and the regions used for different operating AFM modes.*

Depending on the distance between the tip and surface, i.e. on the interaction strength between the two, AFM can be divided in three main operation modes: (1) contact (2) non-contact and (3) semi-contact, which is a transition mode between the contact and non-contact modes (see Fig. 2.5b). The cantilever oscillates vertically at its resonance frequency or close to it (typical values are found in the range of 50 kHz to 500 kHz). Mechanical oscillations of the cantilever are excited by the piezo-driver that has a direct contact with the cantilever substrate. The particular feature of this mode is that the oscillating tip slightly knocks the sample surface during the scanning only in the lowest point of its amplitude. In the same time, during the most of its oscillation period the cantilever does not touch the surface and their interaction level is relatively low. The vertical position of the scanner at each (x, y) data point in order to maintain a constant ¨setpoint¨ amplitude is stored by the computer to form the topographic image of the sample surface.

(d) Transmission electron microscopy (TEM)

For the TEM study, the phthalocyanine thin films were coated with a thin carbon film, floated off on a diluted aqueous hydrofluoric (HF) solution (5% in weight) and then transferred onto copper microscope grids. The films were studied in a bright field and diffraction modes with a 120 kV Philips CM12 electron microscope equipped with a MVIII CCD camera.

2.1.3.b Optical study of thin films

(a) UV-Vis absorption and reflection.

The UV-Vis measurements of absorption and reflection spectra for the prepared films of H_2Pc and CoPc were measured at room temperature. The absorption measurements in the range of 1.2 – 6.2 eV under normal incidence and the reflectance was measured at an angle of incidence of 8° for the same spectral range. Both measurements have been done using a double-beam spectrometer (Perkin Elmer Lambda 950 UV/Vis).

2.2 Gallium Nitride (GaN)

The III-V nitrides are characterized by large bandgaps which make them suitable for optoelectronic applications covering most of the visible range of the electromagnetic spectrum. GaN and related compounds have emerged as one of the most successful systems for optoelectronic applications in the UV-Vis spectral range [Mohammed92, Edgar94, Majewski96]. Figure 2.6 shows the energy gap versus the lattice constant for several compound semiconductors. The weak spin-orbit coupling and large exciton binding energy of the III-V nitrides (~ 17 meV and ~ 26 meV in bulk GaN, respectively), allowing the control of the exciton spin, even at high temperature, make them promising candidates for spintronics. Previous works, in bulk material spin-physics, have shown that spin lifetimes of free excitons in GaN epilayers are in the picosecond range [Kuroda04, Otake06, Tackeuchi06, Ishiguro07].

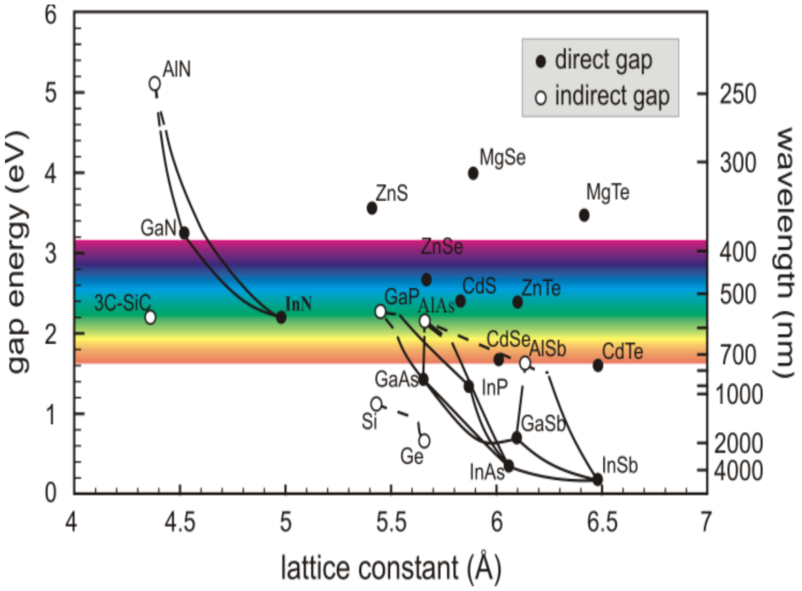

Fig. 2.6. *Energy gap of different compound semiconductors as a function of lattice constant* [Ibach03].

2.2.1 Crystallographic structure

Gallium nitride and its related compounds can crystallize both in the zinc blende (Fig. 2.7a) as well as in the wurtzite structure (Fig. 2.7b); however, the wurtzite is more common. The electronic properties of wurtzite and zinc blende modifications of GaN, InN, and AlN are related, but show significant differences.

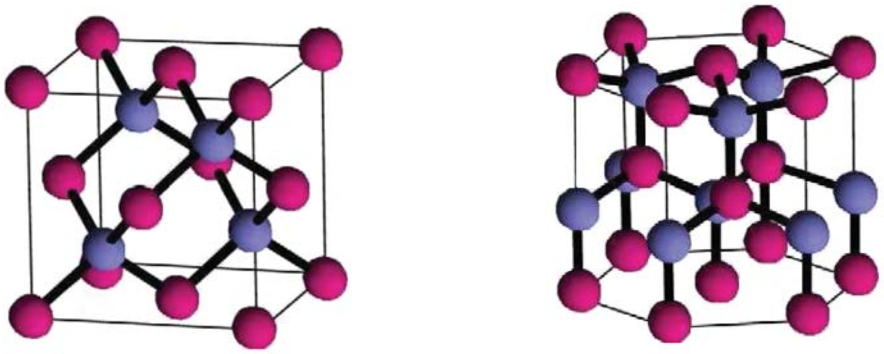

(a) (b)

Fig. 2.7. *Crystallographic structure of* (a) *Zinc Blende and* (b) *Wurtzite.*

Crystallographically, the zinc blende structure and wurtzite structure are very closely related. The Bravais lattice of the wurtzite structure is hexagonal close-packed, and the axis perpendicular to the hexagons is usually labelled as the c-axis. Along the c-axis the structure can be thought of as a sequence of layers of atoms of the same element (e.g. all Ga or all N), built up from regular hexagons.

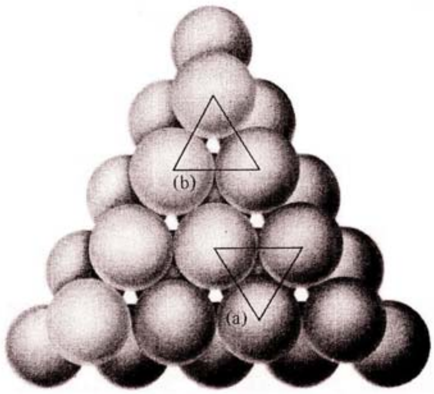

Fig. 2.8. *View from above of the first two layers in a stack of cannonballs. The first layer is arranged in a plane triangular lattice. Balls in the second layer are placed above alternate interstices in the first. The third layer can be arranged by putting balls in the equivalent positions* (a) *or* (b)*. The resulting structure will be close-packed hexagonal for position* (a) *and face centered cubic for position* (b).[Ashcroft76]

If we denote the initial layer of spheres by *A*, the next layer (*B*) is placed above interstices in the first. For the layer as shown in Fig. 2.8, there are two possible ways in placing the atoms, either above layer as shown in position (a) of Fig. 2.8 where balls in the fourth layer are placed directly above those in the second, etc. The resulting structure will be close-packed hexagonal with stacking sequence …….*ABABABABAB*…...or the balls in the third layer are placed directly above those interstices in the first that were not covered by balls in the second, at sites of the type shown in position (b) of Fig. 2.8. Balls in the fourth layer placed directly above those in the first, balls in the fifth directly above those in the second, etc., the resulting structure will be face centered cubic and then the stacking of layers is.......*ABCABCABCABC*......for zinc blende lattice [Ashcroft76, Vainshtien82].

The most important property of both, wurtzite and cubic GaN, is its direct band gap allowing efficient light emission and being useful for laser applications. The band structure of wurtzite material is quite close to that of direct band gap zinc blende semiconductors such as GaAs, but there are significant differences. One key difference is that the valence band degeneracy is lifted in GaN by the crystal field interaction, and consequently there are three band gap excitons, usually labelled A-, B-, and C- exciton.

2.2.1.a Cubic GaN

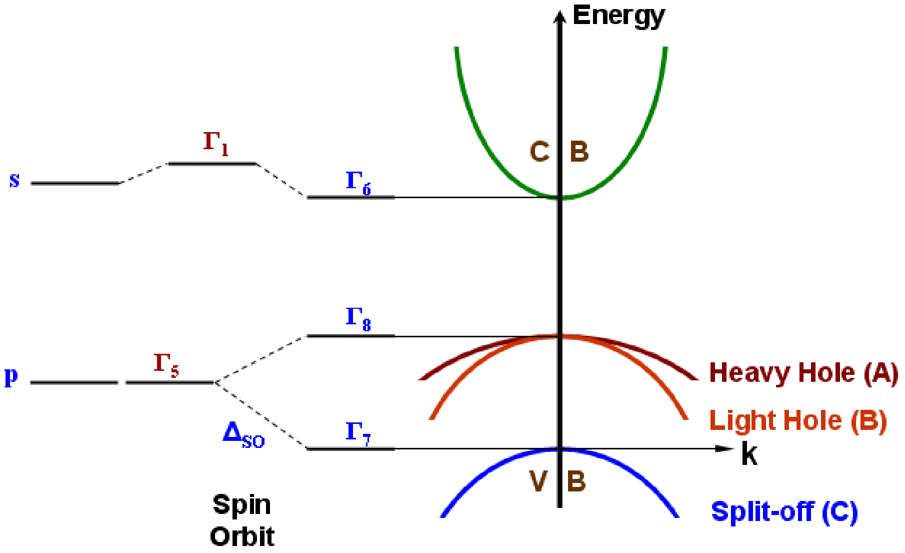

Fig. 2.9. *Band structure and symmetry of the valence band of cubic GaN at Γ- point.*

In the cubic (zinc-blende) structure, the spin-orbit interaction splits, at the Γ-point, the valence band into two levels. The first having Γ_8 symmetry corresponds to bands of heavy holes (HH) and light holes (LH), while the second (Γ_7), is shifted by Δ_{SO}, which is the band called "split-off " (see Fig. 2.9). Each of these bands is doubly degenerate and is characterized by its total angular momentum, $J=L+S$, and its projection along the z-direction, J_z [Long68].

2.2.1.b Hexagonal GaN

Neglecting the electron spin, triplet valence band in the case of hexagonal (wurtzite) structure is split into a doublet Γ_5 and a singlet Γ_1 which are induced by the crystal field, Δ_{Cr}. Including the spin and taking the effect of spin-orbit interaction into consideration, the Γ_5 in the valence band splits into two levels Γ_9 and Γ_7 (as shown in Fig. 2.10) corresponding to heavy holes (HH) and light holes (LH) and the singlet Γ_1 becomes Γ_7 which is called "split-off ".

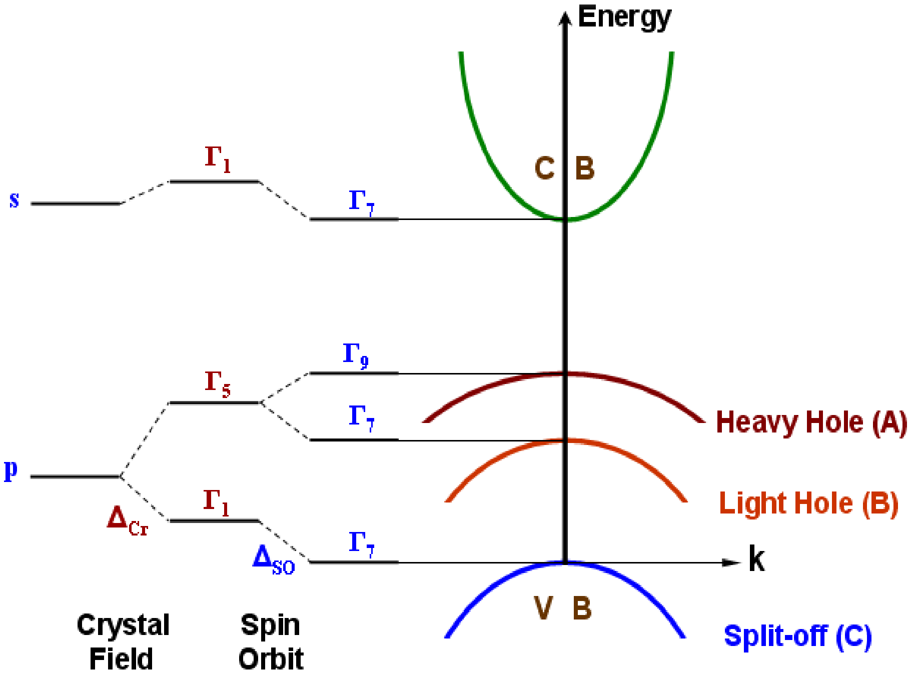

Fig. 2.10. *Band structure and symmetry of the valence band of hexagonal GaN at Γ-point.*

The structure of the valence band is essential for the interpretation of our experimental data. In the crystals of zinc blende type, the valence band dispersion u(**k**) close to the Γ-point can be described using the Hamiltonian of Luttinger-Kohn [Luttinger55]. For the wurtzite structure, one has to consider three parabolic bands.

Direct optical transitions at or near the Γ-point (k = 0) are important for light emitting diodes and laser devices based on GaN. This transition is between the uppermost valence band states and the lowest conduction band minimum. The band gap of wurtzite GaN is higher than that of zinc-blende GaN. Different data for the band gaps are compared in Table 2.1.

The electronic band structure and dielectric functions of zinc-blende (cubic) and wurtzite (hexagonal) GaN films have been compared using ellipsometry spectroscopy and theoretically by Petalas et al. [Petalas95]. The relationships between the band gaps of wurtzite and zinc blende semiconductors have been considered in detail by Yeh et al. [Yeh94]. Time resolved photoluminescence of an ensemble self-organized cubic GaN/AlN quantum dots have been studied by Lagarde et al. [Lagarde08]

Table 2.1. *Comparison of values for the fundamental band gap of zinc blende and wurtzite GaN* [Petalas95].

Wurtzite GaN E_g (eV)	Zinc-blende GaN E_g (eV)	Technique
3.44	3.17	Ellipsometry
-	3.23	Modulated Photoreflectance
3.54	3.37	Reflection
3.45	3.21	Cathodoluminescence
3.44	3.28	Photoluminescence

Let us consider the uppermost valence bands of the wurtzite GaN. According to G. L. Bir and W. Kohn [Bir72], the Hamiltonian for the wurtzite structure, can be written as a matrix 6 × 6. The matrix can be written according to the following basis [Suzuki95, Dietl08]:

$$(1/\sqrt{2})\left|(X+iY),\uparrow\right\rangle,(1/\sqrt{2})\left|(X+iY),\downarrow\right\rangle,$$

$$\left|Z,\uparrow\right\rangle,\left|Z,\downarrow\right\rangle,$$

$$(1/\sqrt{2})\left|(X-iY),\uparrow\right\rangle,(1/\sqrt{2})\left|(X-iY),\downarrow\right\rangle,$$

Where $\left|X\right\rangle$, $\left|Y\right\rangle$, and $\left|Z\right\rangle$ are Bloch functions at the Γ-point, transforming like x, y, and z, respectively, and $\left|\uparrow\right\rangle$ and $\left|\downarrow\right\rangle$ indicate spin states corresponding to spin-up and spin-down, respectively. Using the above six basis functions, the Hamiltonian is explicitly expressed as

$$H(k)=\begin{bmatrix} F & 0 & -H^* & 0 & K^* & 0 \\ 0 & G & \Delta & -H^* & 0 & K^* \\ -H & \Delta & \lambda & 0 & I^* & 0 \\ 0 & -H & 0 & \lambda & \Delta & I^* \\ K & 0 & I & \Delta & G & 0 \\ 0 & K & 0 & I & 0 & F \end{bmatrix}, \tag{2.1}$$

Where F, G, H, I, K, Δ, λ, and θ are defined by

$$\begin{aligned} &F=\Delta_1+\Delta_2+\lambda+\theta, \\ &G=\Delta_1-\Delta_2+\lambda+\theta, \\ &H=iA_6k_zk_+-A_7K_+, \\ &I=iA_6k_zk_++A_7K_+, \\ &K=A_5{k_+}^2,\ \Delta=\sqrt{2}\Delta_3, \\ &\lambda=A_1{k_Z}^2+A_2(k_x^2+k_y^2), \\ &\theta=A_3{k_Z}^2+A_4(k_x^2+k_y^2), \\ &k_\pm\equiv k_x\pm ik_y \, . \end{aligned} \tag{2.2}$$

where A_i, i=1,…..6 represent the effective mass parameters, , A_7 is the weighting factor for the k- linear term and Δ_i , I =1,2,3 denote the parameters characterizing energy splitting at k=0. Δ_1 corresponds to the energy splitting induced by the hexagonal symmetry, and Δ_2 and Δ_3 correspond to those by spin-orbit interaction. The energy levels $E(k)$ in the effective-mass approximation can be obtained by solving the following secular equation:

$$D(k)=\det\left|H(k)-E(k)I\right|=0, \tag{2.3}$$

where I is the 6 x 6 unit matrix.

The analytical solution of the Hamiltonian gives the energy levels at k = 0 as follow:

$$E^0(\Gamma_{9v})=\Delta_1+\Delta_2 \tag{2.4}$$

$$\Delta E^0(\Gamma_{7v})=\frac{\Delta_1-\Delta_2\pm\sqrt{(\Delta_1-\Delta_2)^2+8\Delta_3^2}}{2}, \tag{2.5}$$

Band	Bloch Waves	Atomic notation $\lvert J,J_z\rangle$
Γ_7	$u_1 = \lvert S\uparrow\rangle$ $u_2 = \lvert S\downarrow\rangle$	$\lvert 1/2,1/2\rangle$ $\lvert 1/2,-1/2\rangle$
Γ_9	$u_3 = -\frac{1}{\sqrt{2}}\lvert (X-iY)\uparrow\rangle$ $u_4 = -\frac{1}{\sqrt{2}}\lvert (X+iY)\downarrow\rangle$	$\lvert 3/2,3/2\rangle$ $\lvert 3/2,-3/2\rangle$
Γ_7	$u_5 = \frac{1}{\sqrt{2}}\gamma\lvert (X+iY)\downarrow\rangle + \delta\lvert Z\uparrow\rangle$ $u_6 = \frac{1}{\sqrt{2}}\gamma\lvert (X-iY)\uparrow\rangle + \delta\lvert Z\downarrow\rangle$	$\lvert 3/2,1/2\rangle$ $\lvert 3/2,-1/2\rangle$
Γ_7	$u_7 = \frac{1}{\sqrt{2}}\delta\lvert (X+iY)\downarrow\rangle - \gamma\lvert Z\uparrow\rangle$ $u_8 = \frac{1}{\sqrt{2}}\delta\lvert (X-iY)\uparrow\rangle - \gamma\lvert Z\downarrow\rangle$	$\lvert 1/2,1/2\rangle$ $\lvert 1/2,-1/2\rangle$

where

$$\begin{aligned} \gamma &= [2/(2+B_0^2)]^{1/2} \\ \delta &= B_0/(2+B_0^2)^{1/2} \\ B_0 &= -2+3\Delta_1/\Delta_{SO}\,, \end{aligned} \tag{2.6}$$

Δ_{SO} is the energy splitting induced by the spin-orbit interaction. We have used the notations introduced by K. Cho [Cho76]. It turns out that the coupling between light-hole bands and split-off is depending on the ratio between crystal field and spin-orbit interaction.

2.2.2 Excitons

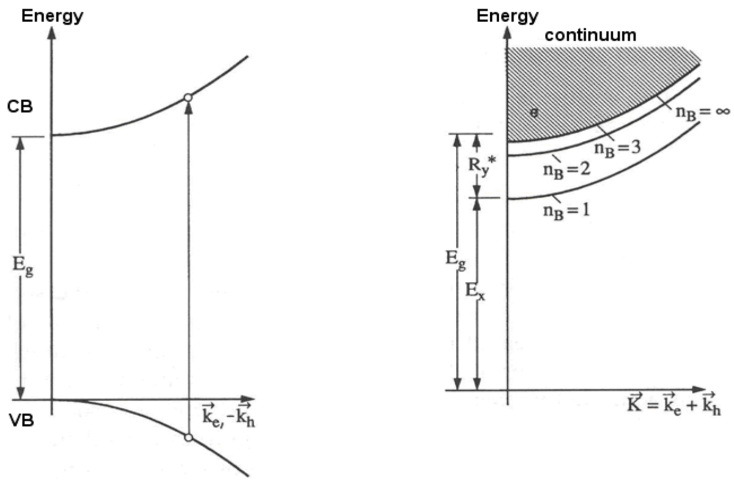

(a) (b)

Fig. 2.11. *A pair excitation in the scheme of valence and conduction band* (a) *and in the exciton picture of a direct band gap semiconductor* (b).

In a semiconductor the number of electrons in a band remains constant in the case of optical excitations with photon energies below the energy of the band gap. To excite an electron-hole pair in a semiconductor, it is necessary to consider the Coulomb attraction between the conduction-band electron and the valence-band hole. The inclusion of the Coulomb interaction results in the formation of bound electron-hole pairs, which are called *excitons* [Knox63, Klingshirn97]. Figure 2.11a shows electron-hole pair in the scheme valence and conduction band with a Coulomb potential term:

$$-e^2/(4\pi\varepsilon_0\varepsilon|r_e - r_h|).$$

where ε_0 is the vacuum permittivity, ε the relative dielectric constant, and r_e, r_h the position of the electron and hole, respectively.

Excitons in semiconductors form, to a good approximation, a hydrogen or positronium like series of states below the gap. For simple parabolic bands and a direct-gap semiconductor one can separate the relative motion of electron and hole and the motion of the center of mass. This leads to the dispersion relation of excitons as depicted in Fig. 2.11b.

$$E_{ex}(n_B,\mathrm{K}) = Eg - R_y^* \frac{1}{n_B^2} + \frac{\hbar^2 K^2}{2M} \tag{2.7a}$$

with

$n_B = 1,2,3,...$ Principal quantum number,

$R_y^* = 13.6eV \frac{\mu}{m_0}\frac{1}{\varepsilon^2}$ Exciton binding energy,

$M = m_e + m_h$, $\boldsymbol{K} = \boldsymbol{k}_e + \boldsymbol{k}_h$ translational mass and wave vector of the exciton (2.7b)

and

$\mu = \frac{m_e m_h}{m_e + m_h} m_0$ is a reduced mass, (2.7c)

$a_B^{ex} = a_B^H \varepsilon \frac{m_0}{\mu}$ excitonic Bohr radius. (2.7d)

The kinetic energy term in (2.7a) involves the translational mass M and the total wave vector $\boldsymbol{K}$ of the exciton. The radius of the exciton equals the Bohr radius of the H-atom again modified by ε and μ. Using the material parameters for typical semiconductors one finds $1meV \le R_y^* \le 200meV << E_g$ and $50nm \ge a_B \ge 1nm > a_{lattice}$. This means that the excitonic Rydberg energy R_y^* is much smaller than the width of the forbidden gap and the Bohr radius is larger than the lattice constant. In this case, the orbits of the electron and hole around their common center of mass average over many unit cells. These excitons are called Wannier excitons [Wannier37]. In insulators or in organic crystals excitons also exist with electron-hole pair wavefunctions confined to one unit cell and the e-h pairs are strongly bound. These excitons are called Frenkel excitons [Frenkel31].

2.2.3 Quantum Well

A quantum well (QW) is a potential well that confines particles, which were originally free to move in three dimensions, to two dimensions, forcing them to occupy a planar region. It consists of a sandwich structure with a thin layer of narrower band gap semiconductor in the middle of two layers of wider band gap semiconductor, called barriers.

If the motion of the particles is restricted by a square potential well in one dimension to a distance comparable to or smaller than the Bohr radius of the exciton, quasi two dimensional electron and hole systems can be created. For typical semiconductors this limit is reached for widths of the constraining potential well l_z below a few tens of nm [Klingshirn97].

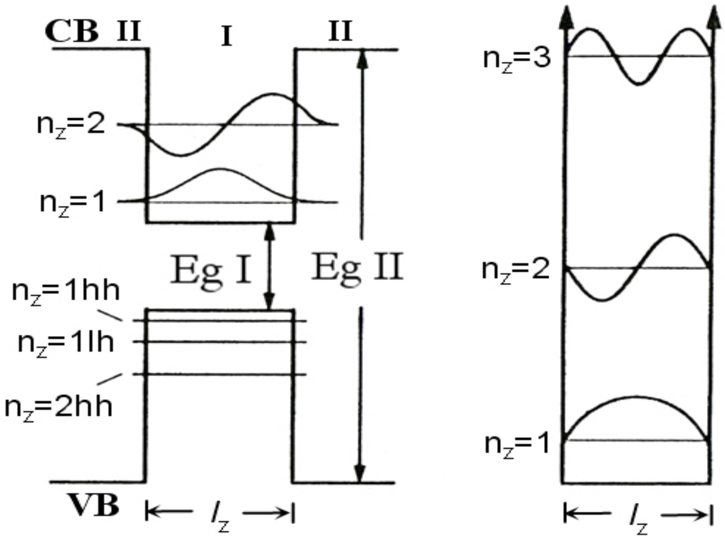

(a) (b)

Fig. 2.12. *A single quantum well* (a) *and energy levels of an idealized quantum well* (b).

The most widely applied method is to use two heterojunctions with a certain separation l_z fulfilling the above condition, which results in a potential well of rectangular shape. As shown in Fig. 2.12a, a single band in the three-dimensional material yields a limited number of subbands with dispersion relation:

$$E(k) = E_{n_z} + \frac{\hbar^2 (k_x^2 + k_y^2)}{2m_{e,h}}, \tag{2.8}$$

where each subband has its constant density of states.

Figures 2.12b show a single idealized potential well with infinitely high barriers on both sides. In this case the quantization energies E_{n_z} are given by

$$E_{n_z} = \frac{\hbar^2 \pi^2}{2m_{e,h} l_z^2} n_z^2, \qquad n_z = 1,2,3,\ldots. \tag{2.9}$$

The wave functions are standing waves with amplitudes = 0 on the walls of the quantum well. This means that the probability to find e-h within the barriers is = 0, which is not the case in real quantum well with finite barrier height. According to equation (2.9) for $l_z \rightarrow 0$, E diverges. For a real quantum well, one finds only a limited number of bound states and these states converge for $l_z \rightarrow 0$ to the Bloch states of the barrier material.

In the case of narrow GaN/AlGaN quantum wells, the large exciton binding energy of (> 30 meV), makes them good candidates to be used at room temperature in spintronic applications [Stokker08a].

2.2.4 Exciton fine structure in a QW.

The conduction band at Brillouin-zone center has s-orbital character with a two-fold degeneracy due to the electron's spin (s = ½) for cubic symmetry bulk GaN. The valence band has p-orbital character and the top valence is four fold degenerate ($J = 3/2$) due to spin-orbit interaction. In axial symmetry like III-V heterostructures, the valence band is further split into heavy hole (HH) with $m_j = \pm 3/2$ and light hole (LH) with $m_j = \pm 1/2$, each two-fold degenerate.

The fine structure of excitons is resulting from these symmetry considerations and from the exchange interaction. The splitting of HH-LH is large, so that the interaction between them can be neglected. This results in a two-fold degenerate light HH exciton with $J_z = \pm 1$ which is dipole allowed. It is separated from a nearly two fold degenerate dipole-forbidden dark HH exciton state by $3\Delta_z/2$ where Δ_z is the z-component of the exchange energy as shown schematically in Fig. 2.13 [Shah96].

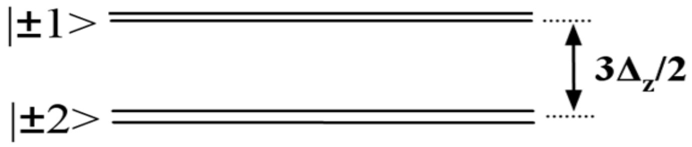

Fig. 2.13. *Fine structure for HH-exciton states in a quantum well.*

2.2.5 Optical selection rules

When an electron-hole pair is created, the kinetic momentum of the absorbed photon is transferred to the exciton. The angular momentum is distributed between the electron and hole according to the selection rule imposed by the band structure of the semiconductor. Thus, the state is optically active if

$$J_z^e + J_z^h = \pm 1 \tag{2.10}$$

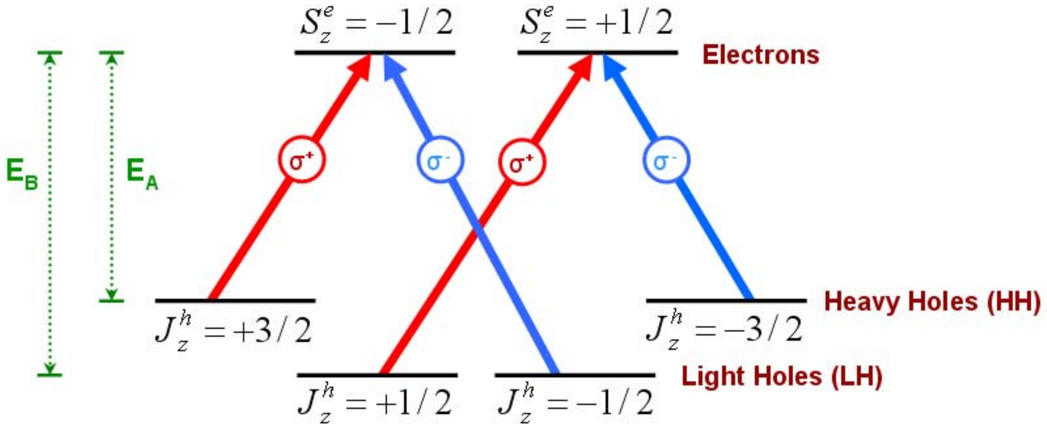

Fig. 2.14. *Optical selection rule in hexagonal GaN.*

In the conduction band, the *z*-component of the electron's angular momentum is represented by S_z with spin S_z^e = ± 1/2 as their orbital momentum is zero. On the contrary, in the valence band, holes are quasi particles with the projection of the total angular momentum on to the *z*- axis can take the values J_z^h = ± 3/2 for the heavy-holes (HH) and J_z^h = ± 1/2 for the light-holes (LH). From the states S_z^e = ± 1/2 and J_z^h = ±3/2, we can build four excitons with total kinetic momentum ± 1 and ± 2:

$$
\begin{aligned}
&\left|+1\right\rangle = \left|-1/2,+3/2\right\rangle && (2.11)\\
&\left|-1\right\rangle = \left|+1/2,-3/2\right\rangle\\
&\left|+2\right\rangle = \left|+1/2,+3/2\right\rangle\\
&\left|-2\right\rangle = \left|-1/2,-3/2\right\rangle
\end{aligned}
$$

Among these four states, only the excitons of angular momentum $\left|\pm 1\right\rangle$ are optically active. We have used spectrally filtered pump pulses by using a Fabry-Perot cavity to achieve a resonant optical pumping of the heavy-hole (HH) excitonic transition with total angular momentum $\left|\pm 1\right\rangle_A$ for A-exciton and exclude the light-hole (LH) excitonic transition as it has different energy.

The selection rules therefore discriminate optical transitions between these levels according to the sense of circular polarization of the excitation photon. In other words, the application of optical selection rules and the use of circularly polarized light create carriers in a particular spin state. Similarly, the analysis of the polarization of light transmitted, reflected or emitted by a semiconductor can determine the spin state of electrons and holes participating in the spin-polarized exciton. We use these two properties in our experiment to create and detect a population of spin-polarized excitons. The possible transitions are shown in Fig. 2.14.

2.2.6 Reflectivity

As explained in more detail in Ref. [Klingshirn97], the reflectivity *R* probes the density of states of a material. In semiconductors, there is not only one type of oscillator and one type of resonance frequency ω_0, but many of them like phonons, excitons etc.

Therefore, the dielectric function $\varepsilon(\omega)$ is given by sum over all resonances which results in the so-called Helmholtz-Ketteler formula:

$$\varepsilon(\omega) = 1 + \sum_{j} \frac{f_j^{'}}{\omega_{0j}^2 - \omega^2 - i\omega\gamma_j} \tag{2.12}$$

The contribution of an isolated resonance at $\omega_{0j'}$ in eq. (4.12) is constant for $\omega << \omega_{0j'}$ and allows some simplification.

$$\varepsilon(\omega) = \varepsilon_b \left(1 + \frac{f_{j'}}{\omega_{0j'}^2 - \omega^2 - i\omega\gamma_{j'}} \right) \tag{2.13}$$

where ε_b is the background dielectric constant. It is unity for the highest resonance in the sum of eq. (2.12) and $f_{j'} = f_{j'}^{'}\varepsilon_b^{-1}$

The equation (2.13) can be separated into real and imaginary parts

$$\varepsilon(\omega) = \varepsilon_b \left(1 + \frac{f(\omega_0^2 - \omega^2)}{(\omega_0^2 - \omega^2)^2 + \omega^2\gamma^2} + i\frac{\omega\gamma f}{(\omega_0^2 - \omega^2)^2 + \omega^2\gamma^2} \right) = \varepsilon_1(\omega) + i\varepsilon_2(\omega) \tag{2.14}$$

The complex index of refraction is connected to the dielectric function via

$$\tilde{n} = n(\omega) + ik(\omega) = \varepsilon^{1/2}(\omega) \tag{2.15}$$

and consequently

$$\varepsilon_1(\omega) = n^2(\omega) - k^2(\omega) \tag{2.16}$$

$$\varepsilon_2(\omega) = 2n(\omega)k(\omega) \tag{2.17}$$

or

$$n(\omega) = \left(\frac{1}{2} \left\{ \varepsilon_1(\omega) + [\varepsilon_1^2(\omega) + \varepsilon_2^2(\omega)]^{1/2} \right\} \right)^{1/2} \tag{2.18}$$

$$k(\omega) = \left(\frac{1}{2} \left\{ -\varepsilon_1(\omega) + [\varepsilon_1^2(\omega) + \varepsilon_2^2(\omega)]^{1/2} \right\} \right)^{1/2} \tag{2.19}$$

Knowing $\tilde{n}(\omega)$, the reflectivity $R(\omega)$ at normal incidence is given by

$$R(\omega) = \frac{I_r}{I_i} = \frac{[n(\omega) - 1]^2 + k^2(\omega)}{[n(\omega) + 1]^2 + k^2(\omega)} \tag{2.20}$$

2.2.6.a Differential reflectivity

In our measurements, we analyse separately the two orthogonal polarization components of linearly or circularly polarized probe pulses. For each time delay with respect to the pump pulse, the two reflected probe spectra are recorded in the presence and then in the absence of the excitation pump pulse and the two ΔR/R spectra are calculated according to the following equation:

$$\frac{\Delta R}{R} = \frac{R_{with\_pump} - R_{without\_pump}}{R_{without\_pump}}$$

As an example, the reflectivity spectra with and without excitation by the pump pulses are shown in Fig. 2.15a. Then by applying the above equation, the differential reflectivity ΔR/R as a function of photon energy is shown in Fig. 2.15b.

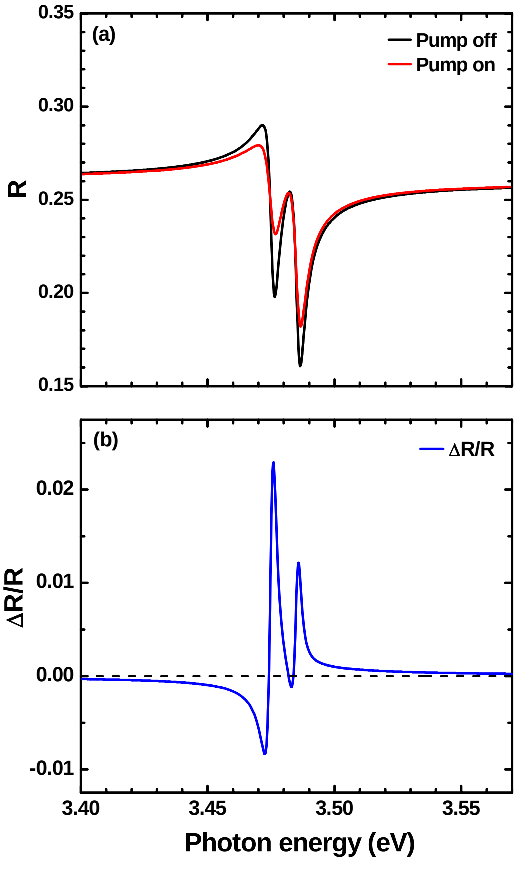

Fig. 2.15. *Reflectivity spectra with and without the pump pulses (a) and the differential reflectivity (b) as a function of photon energy for a given polarization of the probe pulses.*

2.2.7 Spin relaxation

Spin relaxation is a process that leads to equilibrium spin polarization and has great importance for spintronics. Spin relaxation can be generally understood as a result of the action of magnetic fields fluctuating in time. In most cases, these are not real magnetic fields, but rather effective magnetic fields originating from the spin-orbit, or sometimes, exchange interactions or from the finite wave vector of the excitons. A randomly fluctuating magnetic field is characterized by two important parameters: its amplitude and its correlation time τ_c, i.e. the time during which the field may be considered as being constant. Instead of the amplitude, it is more convenient to use the average spin precession frequency ω in this random field, and the angle of spin precession during the correlation time, is given by $\omega\tau_c$.

The physical picture of spin relaxation can be imagined as follows: the spin makes a precession around the random direction of the effective magnetic field with a typical frequency ω and during a typical time τ_c. After a time τ_c the direction and the absolute value of the field change randomly, and the spin starts its precession around the new direction of the field. After a certain number of such steps the initial spin orientation will be completely forgotten.

There are two limiting cases to be considered:

- If $\omega\tau_c << 1$, which is usually the case, the precession angle is small, so that the spin vector experiences a slow angular diffusion. During a time interval t, the number of random steps is t/τ_c, and for each step the squared precession angle is equal $(\omega\tau_c)^2$. These steps are not correlated, so that the total squared angle after time t is $(\omega\tau_c)^2 t/ \tau_c$. The spin relaxation time τ_s may be defined as the time at which this angle becomes of the order of unity: $1/ \tau_s \sim \omega^2\tau_c$.

- If $\omega\tau_c >> 1$, a spin will make many rotations around the direction of the magnetic field during the correlation time. During the time on the order of $1/\omega$ the spin projection transverse to the random magnetic field is completely destroyed, while its projection along the direction of the field is conserved. After time τ_c the magnetic field changes its direction, and the initial spin polarization will disappear and the spin relaxation time is of the order of the correlation time [Dyakonov04].

2.2.7.a Spin relaxation mechanisms

If spin up electrons are injected into a metal at time t = 0 creating a spin imbalance, at a later time, t = τ_S (spin relaxation time), the balance is restored by a coupling between spin and orbital degree of freedom. We consider the five most important carrier spin relaxation mechanisms for bulk materials and heterostructures as follow:

(a) Elliott-Yafet mechanism.

In the Elliott-Yafet mechanism [Fabian99, Elliott54, Meier84] electron spins relax because the electron wave functions normally associated with a given spin have an admixture of the opposite-spin state, due to the spin-orbit interaction induced by the lattice ions. The spin-orbit coupling is much smaller than a typical band width ΔE and can be treated as a perturbation. Switching on the spin-orbit interaction adiabatically, an initially spin-up (down) state acquires a spin-down (up) component with amplitude *b*. Since *b* is small, the resulting states can be still named up and spin down according to their largest spin component.

Elliott noticed that an ordinary (spin-independent) interaction with impurities, boundaries, interfaces, and phonons can connect spin up with down electron states, leading to spin relaxation whose rate $1/\tau_s$ is proportional to b^2/τ (τ being the momentum relaxation time determined by up to down scattering). Additional spin-flip scattering is provided by the spin-orbit interaction of the impurities, and by the phonon-modulated spin-orbit interaction of the lattice ions. The latter should be taken together with Elliott's phonon scattering to get the correct low-temperature behaviour of $1/\tau_S$. Yafet showed that it follows the temperature dependence of resistivity: $1/\tau_s \sim T$ at temperature T above the Debye temperature T_D, and $1/\tau_s \sim T^5$ at very low temperature [Elliott54].

(b) D'yakonov-Perel mechanism.

This mechanism explains spin dephasing in solids without a center of symmetry. Spin dephasing occurs because electrons feel an effective magnetic field, resulting from the lack of inversion symmetry and from the spin-orbit interaction, which changes in random directions every time the electron scatters to a different momentum state. This mechanism of spin relaxation of the conduction band electrons was found by D'yakonov and Perel [Zutic04, D'yakonov71]. Without inversion symmetry the momentum states of the spin-up and spin-down electrons are not degenerate: $E_{k\uparrow} \neq E_{K\downarrow}$.

(c) Bir-Aronov-Pikus mechanisms.

The Bir-Aronov-Pikus (BAP) [Bir76] mechanism has its origin in the electron-hole exchange interaction. This interaction depends on the spins of interacting electrons and holes and acts on electron spins as some effective magnetic field. The spin relaxation takes place as electron spins precess along this field. This mechanism dominates at low temperatures for p-doped semiconductors.

(d) Spin relaxation mechanisms in symmetric and asymmetric quantum wells.

In two-dimensional systems the relative importance of the above mechanisms changes dramatically because of the lifting of the degeneracy in the energy spectrum and because of spin-orbit interaction. A two-dimensional size-quantization suppresses the spin-orbit interaction for holes and increases its strength for electrons.

(e) Hyperfine interaction.

The hyperfine interaction [Zutic04], which is the magnetic interaction between the magnetic moments of electrons and nuclei, provides an important mechanism (D’yakonov and Perel) for ensemble spin dephasing and single-spin decoherence of localized electrons, such as those confined in quantum dots or bound on donors. This interaction is too weak to cause effective spin relaxation of free electrons in metals or in bulk semiconductors, as it is strongly dynamically narrowed by the itinerant nature of electrons. In addition to spin dephasing, the hyperfine interaction is relevant for spintronics as a means to couple, in a controlled way, electron and nuclear spin.

Chapter
3
Experimental Methods

Chapter 3

General Experimental Methods

In this chapter we will initially describe the operation of the laser source. Subsequently we will describe all experiments which have been applied to determine the ultrafast dynamics of absorption changes of cobalt phthalocyanine thin films (CoPc) and compare to metal free phthalocyanine H_2Pc by measuring the differential transmission ($\Delta T(t)/T$). Then, the study of spin relaxation of free excitons in narrow GaN/AlGaN quantum wells by measuring the differential reflectivity ($\Delta R(t)/R$) through a technique called "pump-probe experiment" will be discussed.

3.1 Pump-probe spectroscopy

Femtosecond pump-probe spectroscopy is a well known form of ultrafast spectroscopy. In order to obtain synchronized pulses in the pump-probe system, laser pulses are divided into two parts, the pump, which is the more intense of the two and the probe pulse, which is much weaker in order to produce the minimum disturbance of the sample. The separated beams follow different optical paths with one having a variable path length by using a precise motorized translational stage. This is necessary because of the extreme accuracy required for temporal resolution. Varying the path length will in effect vary the time delay between the pump and probe pulses. Following the different optical paths the pump and probe beams are then directed and focused onto the same spatial area on the sample, always taking care that the probe beam is completely covered by the excitation beam.

The transmitted (reflected) beam is then detected with a photodiode or directed onto the entrance slit of a spectrometer attached to a two dimensional charge coupled device camera (CCD). To improve the sensitivity of the experiment in many cases a lock-in amplifier is utilized along with an optical chopper. The chopper is normally placed in the path of the pump beam, which modulates the excitation thus giving a synchronization signal to the lock-in amplifier.

In the case of phthalocyanine samples, where wavelengths selectivity is required, we have used a super-continuum generation from one of the two optical parametric amplifiers (OPAs). The white light source generated in this way (a continuum of wavelengths) provides a large spectrum from which the wavelengths desired for the pump and probe can be selected. Typically, part of the fundamental intense laser pulse is used as the pump whereas the weak probe is chosen from the white light continuum. This will allow the selection of the excited states being probed.

3.1.1 Transmission / Reflection spectroscopy

For the pump-probe transmission spectroscopy, one generally measures the change in the transmitted probe pulse intensity at a given photon energy induced by the pump pulse as a function of the time delay between the pump and the probe pulses. The time resolution is provided by the delay between the pump and the probe pulses, so the transmitted probe intensity can be spectrally and temporally resolved. The data are presented in the form of normalized Differential Transmission (DT) given by $\Delta T(t)/T(t) = (T\,(t)\text{-}\,T_0)/T_0$, i.e. the change in transmission $\Delta T(t) = T(t)\text{-}\,T_0$ induced by the pump pulse divided by the transmission of the probe in the absence of the pump, T_0. The Differential Transmission Spectrum (DTS) can be obtained either by varying the wavelength of a monochromatic probe laser or by spectrally analyzing the transmitted probe energy with a spectrometer in case of using broadband probe (white light continuum).

For the pump-probe reflection spectroscopy, the data are presented in the form of normalized Differential Reflection (DR) given by $\Delta R(t)/R(t) = (R(t)\text{-}\,R_0)/R_0$. The change in reflection $\Delta R(t) = R(t)\text{-}\,R_0$ induced by the pump pulse is divided by the reflection of the probe in the absence of the pump, R_0.

3.2 Laser sources

The study of relaxation phenomena of electronic excitations in semiconductors requires ultra-short pulses of the order of hundred femtoseconds. Pulses of such short duration can be used to achieve a remarkable time-resolution of processes occurring in semiconductors.

3.2.1 Femtosecond laser oscillator with a regenerative amplifier.

The femtosecond laser source we use consists of three parts: an oscillator, pumped by a cw diode-pumped laser (Verdi), producing ultrashort laser pulses, a regenerative amplifier (RegA) which increases the pulse energy by several orders of magnitude and finally a stage of generation of pulses with tunable wavelengths. They are obtained by using two optical parametric amplifiers (OPAs) as schematically shown in Fig. 3.1.

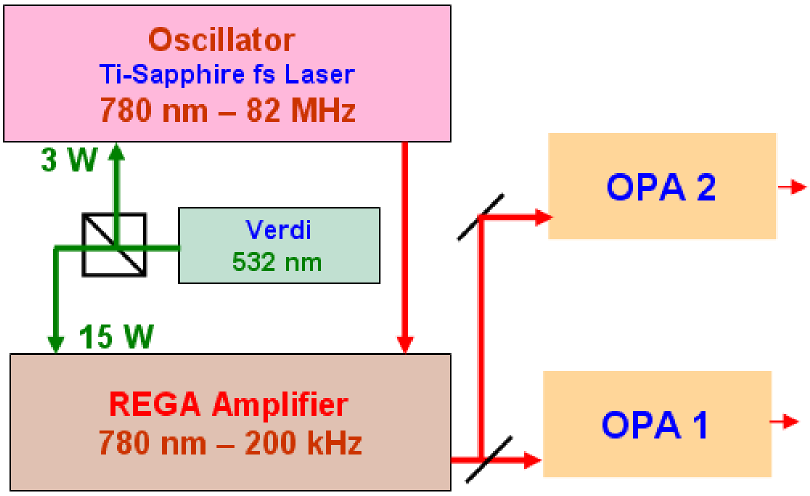

Fig. 3.1. *The different components of the Ti:Sapphire laser source*

3.2.1.a Diode-pump laser (Verdi)

The Verdi laser system is a compact solid-state diode-pumped, frequency-doubled Nd: YVO_4 (Neodymium doped Yttrium Orthovanadate) that provides single-frequency green emission (532 nm) with an output power 18 W. The gain medium employed in Verdi is (Nd: YVO_4). Neodymium ions doped into a vanadate host exhibit a comparatively large absorption coefficient centered at a wavelength convenient for diode-pump lasers.

The characteristic lasing wavelength of neodymium-doped vanadate is nominally 1064 nm, which is the fundamental wavelength of the Verdi resonator. The multilayer dielectric coatings of the four mirrors that define the ring resonator are designed to provide high reflectance centered at 1064 nm to sustain circulating infrared radiation whose power levels that typically exceed 100 watts. Converting a fraction of this circulating power into visible light is accomplished via the process of non-resonant, intracavity, second harmonic generation (SHG). The nonlinear optical medium used for SHG in the Verdi is the birefringent crystal lithium triborate (LBO). The 18 W output power generated by the Verdi laser is split by a beam splitter, into 3 W to pump the oscillator and 15 W to pump the regenerative amplifier.

3.2.1.b Laser oscillator

The femtosecond oscillator, used to produce a train of ultrashort pulses, is a homemade Titanium: Sapphire laser source. It produces pulses within a sufficiently broad spectral range (750 to 850 nm) to excite a high number of longitudinal modes in the laser cavity. The compensation of the group velocity dispersion is ensured by a set of two prisms producing a negative dispersion of the group velocity. When the optical beam passes through the Ti: Sapphire crystal, a self-focusing phenomenon is produced by the optical Kerr effect. The total length of the laser cavity is about 3 meter and produces 80-femtosecond pulses with a repetition rate of 82 MHz.

3.2.1.c Regenerative amplifier (RegA)

For our experiments, we need femtosecond pulses in the visible and ultraviolet spectral range. As our Ti: Sapphire laser oscillator source emits in the infrared with an energy of the order of a few nanojoule per pulse, we use optical parametric amplifiers (OPAs). Since the pulse energy of the oscillator is not sufficient for the operation of our OPAs in order to obtain pulses with higher energies, we use a commercial optical amplifier RegA 9000 (COHERENT). The optical layout of the RegA is shown in Fig. 3.2.

The laser beam coming from the laser oscillator is directed into the RegA head with two mirrors shielded with dust covers and beam tubes. The input beam passes through a Faraday isolator and a single pulse is injected into the RegA by a TeO_2 acousto-optic Cavity dumper (CD). Amplification over 20 to 30 round trips allows the group velocity dispersion (GVD) in the TeO_2 Q-switch to expand this pulse into 30 ps length.

The Cavity Dumper then extracts a single pulse of several μJ energy and this returns through the Faraday Isolator and is separated from the input beam bath by a polarizer. The pulses are then compressed and the final stage in the RegA head allows the high energy compressed pulses to be used to generate broadband white-light. The laser beam can be directed out of the exit port of the RegA head. The output pulses of the RegA have energies of several μJ and pulse duration shorter than 200 fs with a repetition rate 200 kHz.

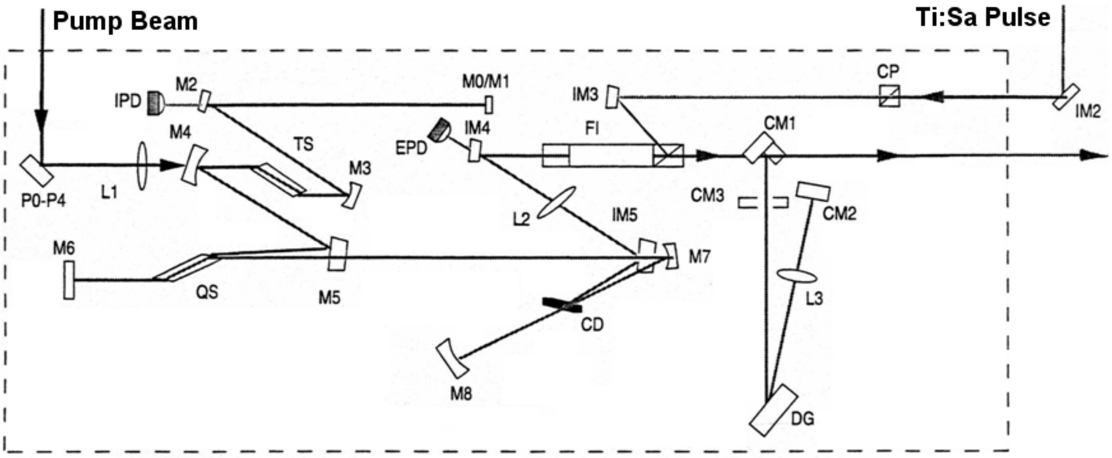

IB:	Ion Beamsplitter	WX:	White-Light Crystal
IPD:	Injection Photodiode	M0 - M8:	Cavity Optics
EPD:	Ejection Photodiode	IM1- IM5:	Injection Optics
QS:	Q-Switch	CM1 - CM3:	Compressor Optics
CD:	Cavity Dumper	WM1 - WM2:	White light Optics
FI:	Faraday Isolator	L0 - L5:	Lenses
CP:	Cube Polarizer	P0 - P4:	Pump Optics
DG:	Diffraction Grating	TS:	Ti: Sapphire Crystal

Fig. 3.2. *Optical scheme of the regenerative amplifier (RegA 9000).*

3.2.1.d Optical parametric amplifier (OPA)

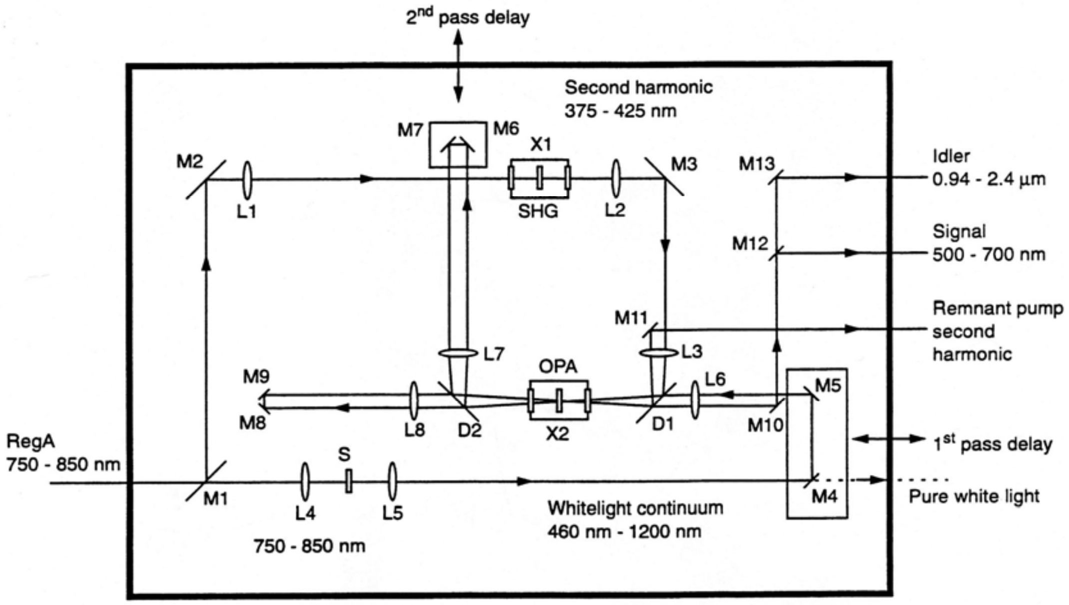
2nd pass delay
Second harmonic
375 - 425 nm
M7
M6
X1
M2
L1
SHG
L2
M3
M13
Idler
0.94 - 2.4 µm
M12
Signal
500 - 700 nm
M11
Remnant pump
second
harmonic
L7
OPA
L3
L6
M9
M5
M8
L8
D2
X2
D1
M10
RegA
750 - 850 nm
S
1st pass delay
M1
L4
L5
M4
Pure white light
Whitelight continuum
460 nm - 1200 nm
750 - 850 nm

M: Mirror **L**: Lens

D: Dichroic Mirror **S**: Sapphire Crystal

OPA BBO: Optical Parametric Amplifier Beta Barium Borate Crystal

SHG BBO: Second Harmonic Generation Beta Barium Borate Crystal

Fig. 3.3. *Optical scheme of the optical parametric amplifier (OPA).*

The optical parametric amplifiers (OPAs) are used to extend the wavelength coverage of the regenerative amplifier. Microjoule pulses from the RegA are split into two beams as depicted in Fig. 3.3:

- The first part, 25%, is focused on a Sapphire crystal to produces white-light continuum seed pulses.

- The second part, 75%, is frequency doubled by focusing on a second harmonic generation BBO crystal. The pulses then have a wavelength of 400 nm.

Then the white-light continuum pulses and the frequency doubled beam undergo a process of parametric conversion in the second BBO crystal of the optical parametric amplifier. In this way it amplifies certain frequencies of the continuum. Multiple outputs are available and all beams are inherently synchronized, because they originate from the same pump pulse. Tuning involves a simple manual adjustment of the OPA crystal and the delay line. The main outputs consist of a signal beam tunable from 500-700 nm, and an idler beam tunable from 940-2400 nm.

For our experiments, we use only the signal beam whose wavelength we can change and generate two pulse trains of different wavelengths (from the two OPAs) with pulse duration of 200 fs and with energies of hundreds of nanojoule.

3.3 Group velocity dispersion compensation (GVD)

In order to successfully generate ultrashort laser pulses, the modes must retain their phase relationship over a long time so that the mode-locking is stable. This requires that all modes experience the same cavity round-trip time, or, equivalently, that the optical length of the cavity is independent of frequency.

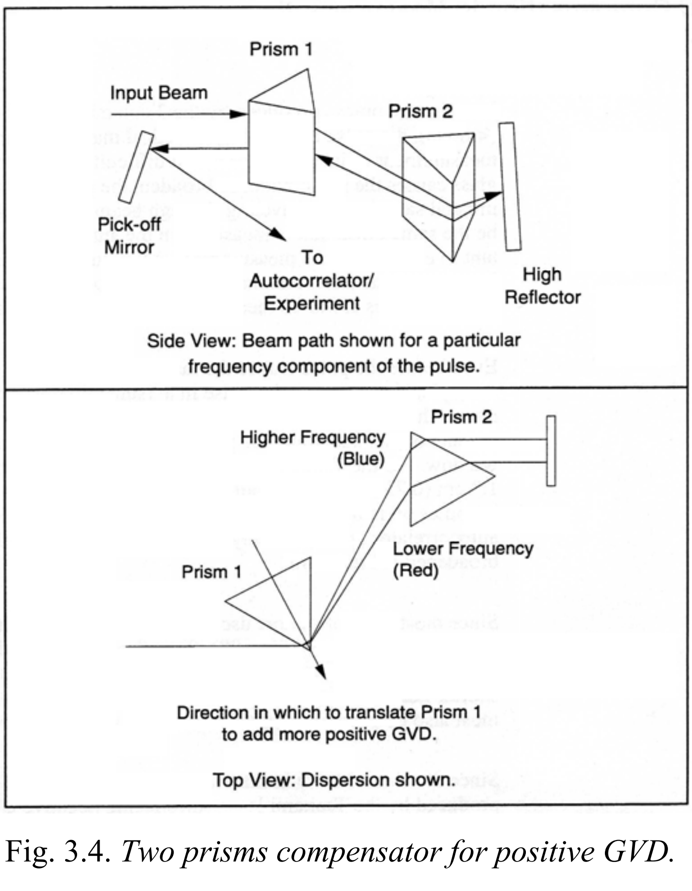
Prism 1
Input Beam
Prism 2
Pick-off Mirror
To Autocorrelator/ Experiment
High Reflector
Side View: Beam path shown for a particular frequency component of the pulse.
Prism 2
Higher Frequency (Blue)
Lower Frequency (Red)
Prism 1
Direction in which to translate Prism 1 to add more positive GVD.
Top View: Dispersion shown.

Fig. 3.4. *Two prisms compensator for positive GVD.*

In general, group velocity dispersion is detrimental to the stability of a short pulse system, since it introduces a phase delay between the different radiation modes and, therefore, it tends to destroy (after a few round trips) the constructive interference.

Undesirable group velocity dispersion can be compensated in a number of ways. Group velocity dispersion compensation (GVD) is generally achieved by introducing a pair of prisms into the cavity, which compensates for normal group velocity dispersion, which leads to a delay of the red components of the pulse with respect to its blue components.

Figure 3.4 shows the layout (top and side views) for an easily built pre-compensation unit. The laser pulse travels through the first prism where different frequency components are spread spatially in different directions. Then the broadened pulse travels through the second prism, impinging on a highly reflecting mirror and is reflected back along its original path with one exception. The high reflector is slightly tilted in the plane perpendicular to the spectral spreading and causes the pulse to travel back through the prisms at a slightly different vertical height. After the beam returns through the first prism it is reflected by another mirror to an autocorrelator and/or the experiment.

3.4 Temporal and spectral characterization of the laser pulse

As electronic devices are too slow for temporal measurements of short pulses (~ 100 fs), nonlinear optical techniques have to be used for this purpose. The basic idea is to convert a measurement from the time domain into a measurement in the space domain by increasing the path of part of the optical pulse with respect to the other pulse, and to convert this path delay into an electric signal directly proportional to the path delay.

The most commonly used method is the autocorrelation technique based on second-harmonic generation. A transparent medium having no inversion symmetry generates light at the harmonic frequency 2ω, if it is irradiated with intense light at frequency ω. It is important to realize that this harmonic generation occurs only during the presence of radiation at ω. Light at frequency 2ω will be preferentially generated in certain directions that satisfy the phase-matching condition $n(\omega) = n(2\,\omega)$.

The phase-matching condition translates the fact that both beams with ω and 2ω propagate with the same phase velocity, so that energy transfer can occur constructively from the beam with frequencies ω and 2ω. If the phase matching condition is not satisfied, the harmonic generated light at a given location x in the crystal will interfere destructively with the harmonic generated light at location x+δ, where δ is the coherence length (defined as $\delta = 2\pi\Delta k$, where $\Delta k = k(2\,\omega) - 2k(\omega)$), with the net result that very little harmonic light will emerge from the crystal. To satisfy the phase-matching condition, one usually selects a birefringent crystal having two different refractive indices (the ordinary and extraordinary) for orthogonal polarization directions. One then chooses the incident light propagation vector such as that the ordinary index and the extraordinary index of the two fields are equal for components having crossed polarizations.

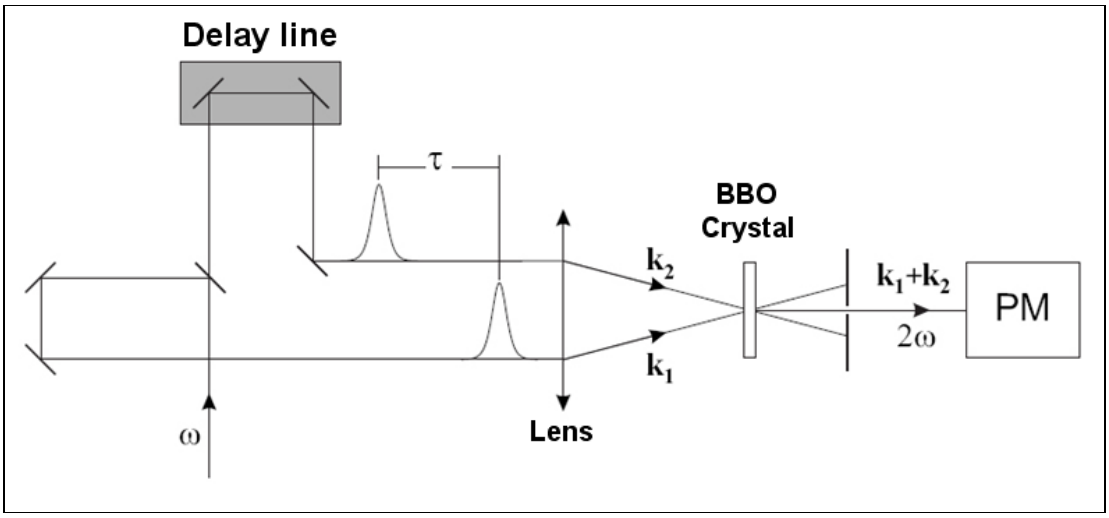

Fig. 3.5. *Schematic setup of an autocorrelation technique for measuring the pulse duration. Beams* $\mathbf{k_1}$ *and* $\mathbf{k_2}$ *are focused onto a second-harmonic generating crystal like BBO with a variable time delay.*

The principle of an autocorrelator is shown in Fig. 3.5. The optical pulse to be measured is divided into two pulses of equal intensity with wavevectors $\mathbf{k_1}$ and $\mathbf{k_2}$. After delaying one pulse with respect to the other, both pulses are recombined in a nonlinear crystal, transparent at both frequencies ω and 2ω. We usually choose a BBO crystal in our experiments that is oriented for phase matching. The second-harmonic light resulting from the time overlap between both pulses is emitted in the direction of $\mathbf{k_1} + \mathbf{k_2}$. It is spatially filtered and detected with a photodetector as a function of time delay. Figure 3.6a shows the autocorrelation signal of femtosecond laser pulses. We have thus pulse duration of 66 fs of pulses, after pulse compression by using the two prisms compensator, centred at photon energy 2.032eV with a spectral width (FWHM) of 26.7 meV as shown in Fig. 3.6b while in the case of GaN/AlGaN QW measurements, the pulse duration is estimated to be 200 fs and spectrally filtered by using a Fabry-Perot cavity a spectral width of 5.46 meV.

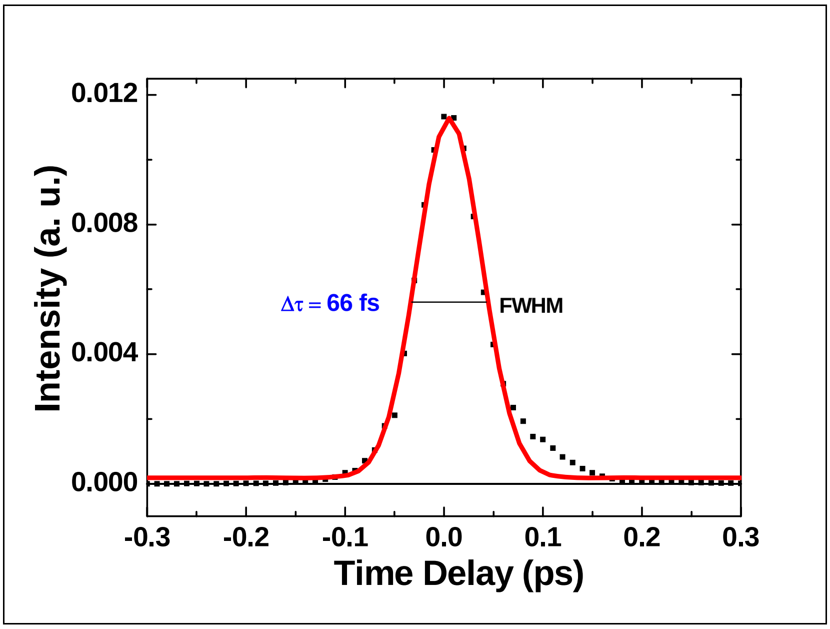

Fig. 3.6a. *Autocorrelation signal of femtosecond laser pulses. The measured pulse duration is 66 fs.*

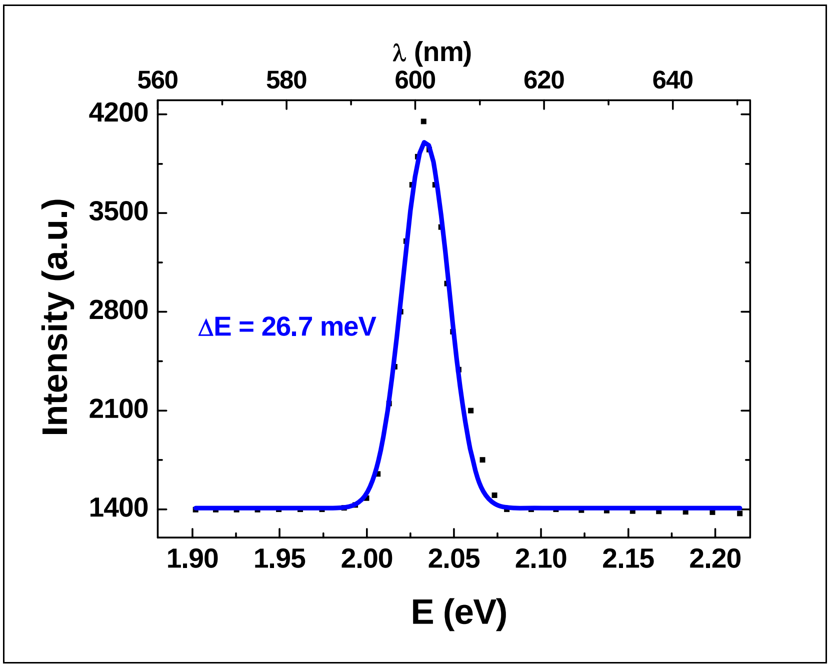

Fig. 3.6b. Spectral characterization of the femtosecond laser pulses. The spectral width (FWHM) of the pulses is 26.7 meV.

3.5 Cryostat

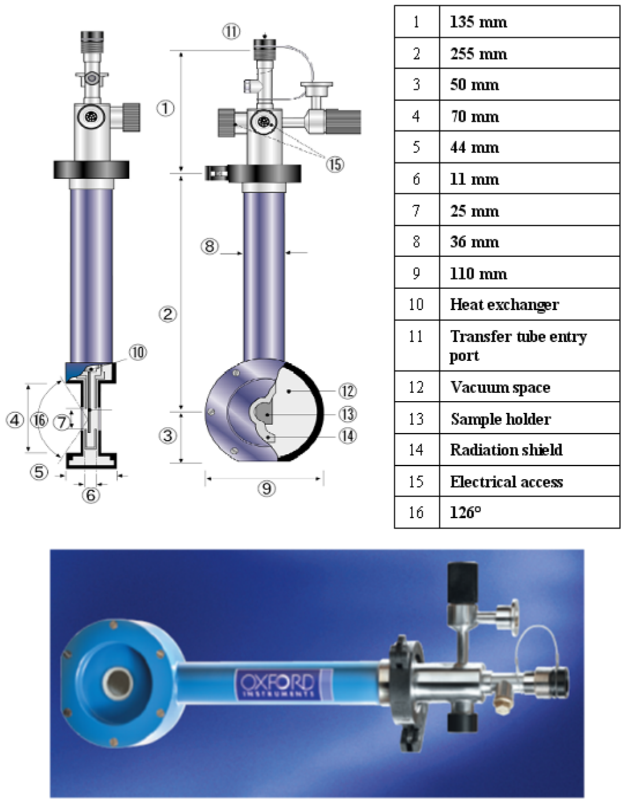

1	135 mm
2	255 mm
3	50 mm
4	70 mm
5	44 mm
6	11 mm
7	25 mm
8	36 mm
9	110 mm
10	Heat exchanger
11	Transfer tube entry port
12	Vacuum space
13	Sample holder
14	Radiation shield
15	Electrical access
16	126°

Fig. 3.7. *The vacuum loading Microstat He cryostat.*

Our experimental results of GaN/AlGaN quantum wells are measured at low temperature using a microstat « Oxford Microstat He » (see Fig. 3.7) with continuous He flow. The vacuum loading Microstat He cryostat is specifically designed for microscopy application requiring temperatures down to 2.2 K. The sample is positioned on the sample holder and liquid helium is transferred to the cryostat via a transfer tube entry which transfers liquid helium to a cold finger in contact with the sample through a thermal grease.

The cold finger provides heat transfer between liquid helium and the sample. The gas resulting from this heat exchange is then evacuated by a pump to get recovery of helium. Precise temperature control is obtained using a temperature controller; we can thus maintain a constant temperature of 4 K or higher. The sample chamber is highly evacuated to be isolated from the surrounding at room temperature. This chamber is pumped by a turbo-molecular pump coupled to a diaphragm pump. It can reach until a pressure of 10^{-7} Pa. Our cryostat, moreover, is mounted on a stand with three decks of translation to optimise the optical access of the cryostat for different samples and the optical access to the sample is possible through two windows.

3.6. Photoluminescence excitation (PLE) spectroscopy

The photoluminescence excitation (PLE) spectroscopy is a widely used tool for the characterization of optical transitions in semiconductors. Luminescence of semiconductors can be roughly divided into three stages. First, the sample is excited out of the ground state which is characterized by a completely filled valence band and empty conduction band. The excitation source creates electron-hole pairs via exciting electrons from the valence band into the conduction band. Second, the nonequilibrium electron and hole distributions tend to relax back to thermal equilibrium. Finally, the electron-hole pairs recombine radiatively under emission of light which is the photoluminescence process. In PLE spectroscopy, the spontaneous emission from the sample is detected at a fixed photon energy, typically at the lowest excitonic resonance in high-purity materials. The intensity of this signal is then recorded as a function of the excitation photon energy.

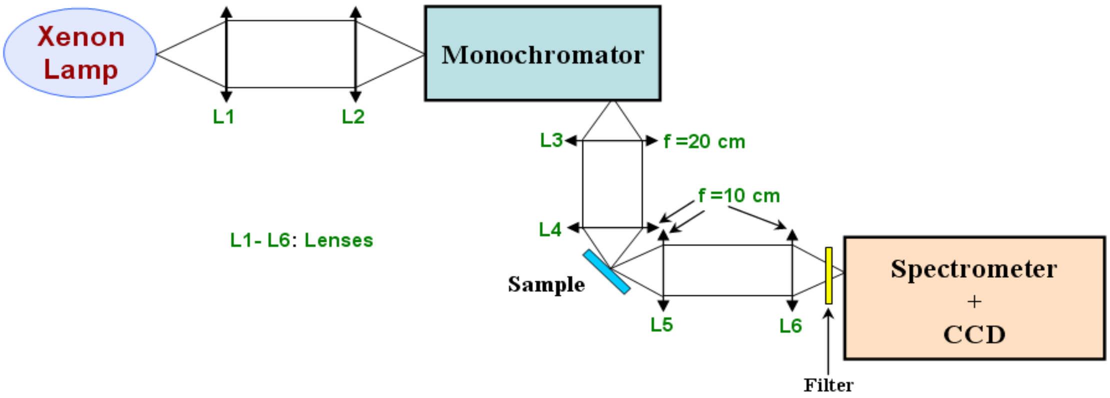

Fig. 3.8. *Scheme of the setup used in photoluminescence excitation experiments.*

The spectroscopic measurements of the PLE have been done following the schematic diagram in Fig. 3.8 by measuring the intensity of the emission spectra at a given photon energy depending on the excitation photon energy. We used an Oxford MG11 cryostat in which the sample was surrounded by cold He gas. The excitation source is a Xenon lamp with power 500W, spectrally filtered by a monochromator to obtain a tunable photon energy with a bandwidth of 4 meV. The GaN/AlGaN quantum well sample, the QW is then illuminated by a source of spectral range 3.52 - 3.62 eV photon energy. The GaN/AlGaN sample was kept at low temperature (7 K) in a cryostat during the PLE measurements. The photoluminescence measured is dispersed in a spectrograph and detected by a cooled charge-coupled device (CCD) camera.

3.7 Experimental setup for measuring differential transmission of phthalocyanine films

The ultrafast optical excited state dynamics of the phthalocyanine films were studied by time-resolved femtosecond pump-and-probe experiments. Femtosecond laser pulses were generated using a Titanium: Sapphire oscillator, which generates 80 fs pulses with a repetition rate of 82 MHz and passed further a regenerative amplifier. At the output, the repetition rate was reduced to 200 kHz. These pulses were sent into optical parametric amplifiers (OPAs), which generate pump and probe pulses.

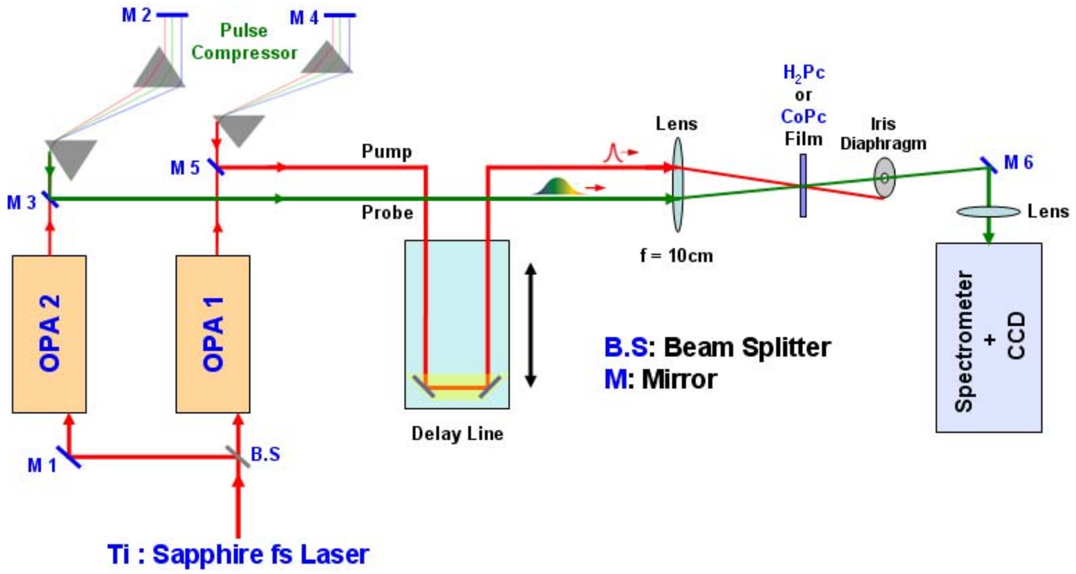
M 2
Pulse Compressor
M 4
H_2Pc
or
CoPc
Film
Lens
Iris Diaphragm
M 6
M 5
Pump
M 3
Probe
Lens
f = 10cm
OPA 2
OPA 1
B.S: Beam Splitter
M: Mirror
Spectrometer + CCD
Delay Line
M 1
B.S
Ti : Sapphire fs Laser

Fig. 3.9. *Optical setup of the temporally and spectrally resolved pump-probe experiment by measuring differential transmission of phthalocyanine films.*

The pump-and-probe experimental setup that we use is shown in Fig. 3.9. In the case of degenerate experiments, pump and probes pulses were generated from the output of the OPA, tuned close to 2.066 eV, i.e. nearly in resonance with the Q-band of H_2Pc and CoPc samples. The intensity of the pump pulses was set to ~ 6 GW/cm^2. For the spectrally resolved experiments, the supercontinuum generated in the OPA and covering the 1.033 – 2.695 eV spectral range was used as probe beam while the pump photon energy was tuned at two different values, 1.823 and 2.032 eV, corresponding to the maximum absorption peaks in the Q-band. Pulses were further compressed and spectrally filtered by optical compressors using a pair of prisms and a spatial filter. The remaining chirp of the probe pulses was measured and the experimental results corrected from these data.

The full width at half maximum (FWHM) of the pulses was close to 70 fs. They were nearly Fourier-transform limited and their spectral widths were close to 26 meV as previously explained in section 3.4 and the intensity of the pump pulses was set ~ 7.8 GW/cm^2. The pulses went through an optical delay line, controlled by a computer. The pump beam was chopped and the probe pulses were then detected at the chopping frequency of the pump beam. The two beams with parallel polarization were focused by a lens with a focal length $f = 10$ cm onto the sample within the same spot of around 100 μm diameter. The sample was kept at room temperature in all measurements.

In the case of degenerate pump-probe measurements, the transmitted probe beam, was collimated onto a photodiode, the signal was amplified by a lock-in amplifier, and monitored as a function of the time delay between the pump and the probe pulses. In the spectrally resolved measurements, the transmitted probe beam passed through a collimating lens and was directed onto the entrance slit of a spectrometer. The spectra were detected in the presence and then in the absence of the excitation pump pulses as a function of the pump-probe delay time, using a two dimensional charge coupled device camera (CCD) attached to the spectrometer as schematically shown in Fig.3.9.

3.8 Experimental setup for measuring differential reflectivity of GaN/AlGaN quantum well

For the study of GaN/AlGaN quantum well sample we have used the same Ti: Sapphire laser source as described in section 3.2.1 but in this case the OPAs were tuned close to the 1.770 eV (700 nm) to generate the pump and the probe pulses. Both of them are frequency doubled within two BBO crystals to reach the GaN exciton spectral region. The pump pulses are spectrally filtered by using a Fabry-Perot cavity to a spectral width of ΔE = 5.46 meV FWHM and are tuned, by minimizing the photoluminescence of the LH$_1$- exciton, to achieve a resonant optical pumping of the HH$_1$- exciton. They pass through an optical delay line and a quarter-wave plate. The pump is circularly polarized with helicity σ^+ and focused onto the sample surface within a spot of 100 microns diameter. The probe pulses, from the second OPA, are spectrally broad and cover the two excitonic transitions (HH$_1$ and LH$_1$). The probe beam is linearly polarized and focused on to the GaN/AlGaN quantum well sample surface into a spot of diameter less than that of the pump, allowing us to probe an area homogeneously excited by the pump beam. The sample was kept in a cold-finger cryostat at liquid helium temperature.

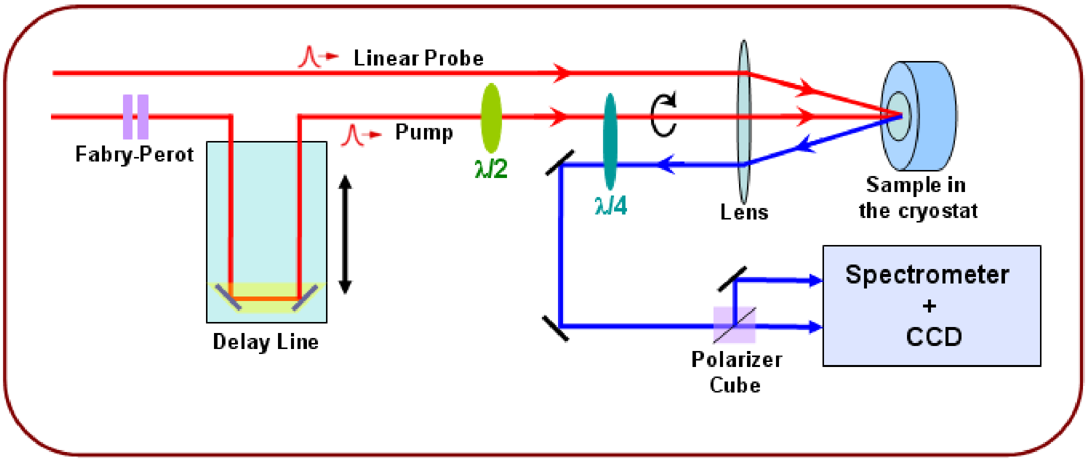

Fig. 3.10. *Optical setup of the temporally and spectrally resolved pump-probe experiment, measuring differential reflectivity of a GaN/AlGaN quantum well.*

The circularly polarized pump pulses selectively excite the HH$_1$ excitonic transition with total angular momentum $|+1>_{HH1}$. The probe beam reflected from the sample, passes through the lens and the quarter-wave plate as schematically shown In Fig. 3.10. The two circular components of the probe, transformed into two linear components by passing through the quarter-wave plate, are separated by a polarizer cube.

The two beams are directed at different heights onto the entrance slit of a spectrometer and are detected as two different spectra by the CCD camera. In this way, the two circular components of the probe pulses are detected simultaneously as a function of the time delay between the pump and the probe pulses. For each time delay, the two reflected probe spectra are recorded in the presence and then in the absence of the excitation pump pulse and the two *ΔR/R* spectra are calculated, one for each polarization ($\sigma^+$and σ^-).

Chapter
4
Results and Discussion
Part I
Phthalocyanine Films

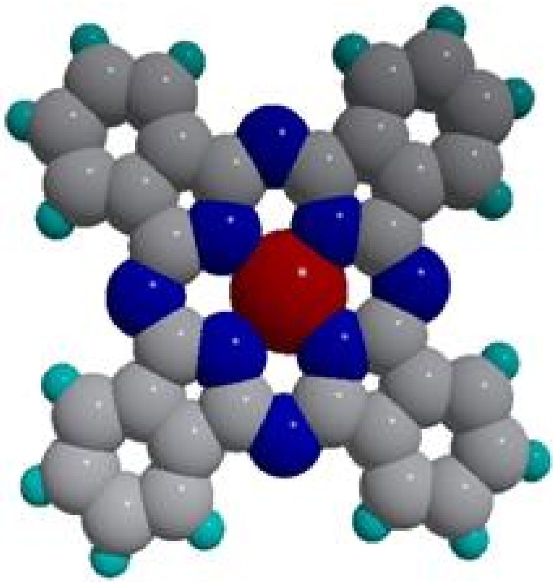

Phthalocyanine

Chapter 4

Results and discussion (Part I): Phthalocyanine Films

4.1 Structural parameters:

4.1.1 X-Ray diffraction (XRD)

The structures of most of metallophthalocyanines (MPcs) have been determined from X-ray diffraction measurements. The MPc molecules crystallize in α- and β-polymorphs. This can be characterized by a herringbone structure with the molecules stacked along the **b-**axis, but differentiated by the tilt angle, Φ, between the plane of the molecule and the stacking axis. The α- phase is generally obtained by growth at room temperature, whereas high temperature growth, or post-growth annealing, leads to the formation of β- films [Yim02]. Figure 4.1 shows the crystal structure of α- and β- phase of H_2Pc; the unit cell axes are labelled a, b, and c. Schematic of α- and β- H_2Pc molecules projected on the (100) and (001) planes, respectively is shown in Fig.4.1a. These planes correspond to the planes parallel to the substrate in thin film form. Schematic of the unit cells and molecular arrangement of α- and β- phase H_2Pc are shown in Fig. 4.1b.

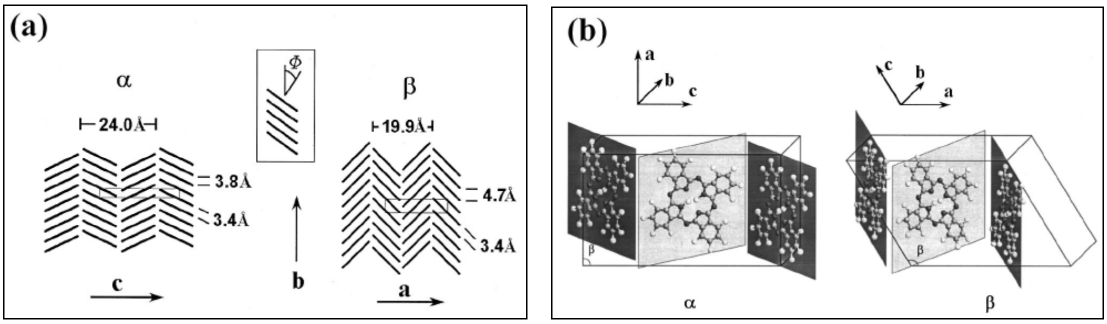

Fig. 4.1. *Crystal structures of α- and β- phase:* (a) *Schematic of α- and β- H_2Pc molecules projected on the (100) and (001) planes, respectively.* (b) *Schematic of the unit cells and molecular arrangement of α- and β- H_2Pc* [Yim02].

X-ray diffraction traces in the θ-2θ geometry for H_2Pc and CoPc films are shown in Fig. 4.2. The main peaks A_1 for H_2Pc and A_2 for CoPc films are nearly coincident at 2θ = 6.8°. Other peaks, less intense, are visible: the B_1 peak for the H_2Pc film is located at 13.60° and the B_2 peak for the CoPc film is located at 28.84°. The interplanar distances corresponding to these peaks are given in Table 4.1. The values for both H_2Pc and CoPc are consistent with the orthorhombic α-form structure previously observed on similar films [Karasek52, Shihub93, Joseph08].

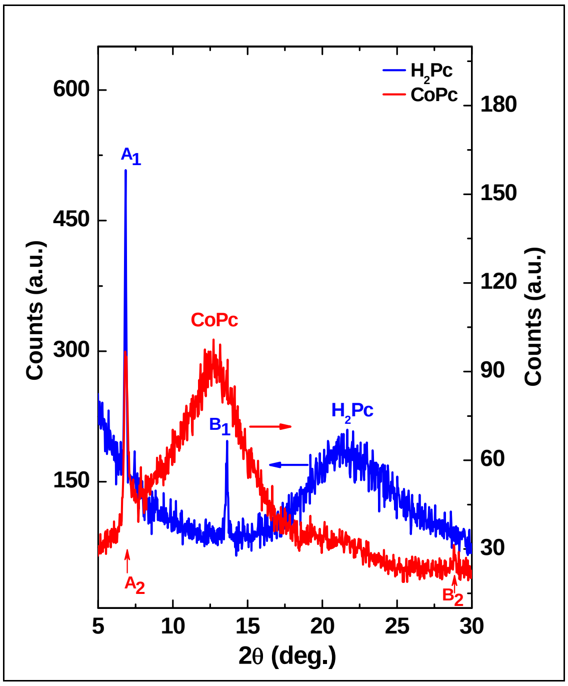

Fig. 4.2. *X-ray diffraction pattern of* H_2Pc *(blue line) and CoPc (red line) thin films.*

The broad peak around 21.4° for H_2Pc and around 12.8° for CoPc is attributed to the fused silica substrate. The intensity ratio between the peaks corresponding to reflection on (200) planes and (400) planes depends on the nature of the substituents in the center of the molecules and on the orientation of these molecules with respect to the surface planes [Liu08]. For CoPc, the (400) peak is almost absent leading to a small ratio of the peak intensities, whereas for H_2Pc, the ratio is much larger. In both cases, this is consistent with molecules standing almost perpendicularly on the surface planes. From the widths of the A_1 and A_2 peak, we deduce a coherence length of 40 nm for the H_2Pc film and 20 nm for the CoPc film, which are shorter but comparable to the film thicknesses of 170 nm.

Table 4.1. *Interplanar Distance of Molecules for* H_2Pc *and CoPc Thin Films with the Same Thickness ~ 170 nm.*

peak	(*hkl*)	d_{hkl} (nm)	2θ (°)
A_1 (H_2Pc)	200	1.2924	6.83
B_1 (H_2Pc)	400	0.6504	13.6
A_2 (CoPc)	200	1.2869	6.86
B_2 (CoPc)	313	0.3093	28.8

4.1.2 Scanning electron microscopy (SEM)

The scanning electron micrographs of H_2Pc and CoPc films are shown in Fig. 4.3. The film growth is found to be perpendicular to the substrate surface for both films. There is a change in the surface morphology between the two films. The average grain sizes of the H_2Pc and CoPc thin films are in the same order, with grain length ~ 100 nm and grain breadth ~ 100 nm.

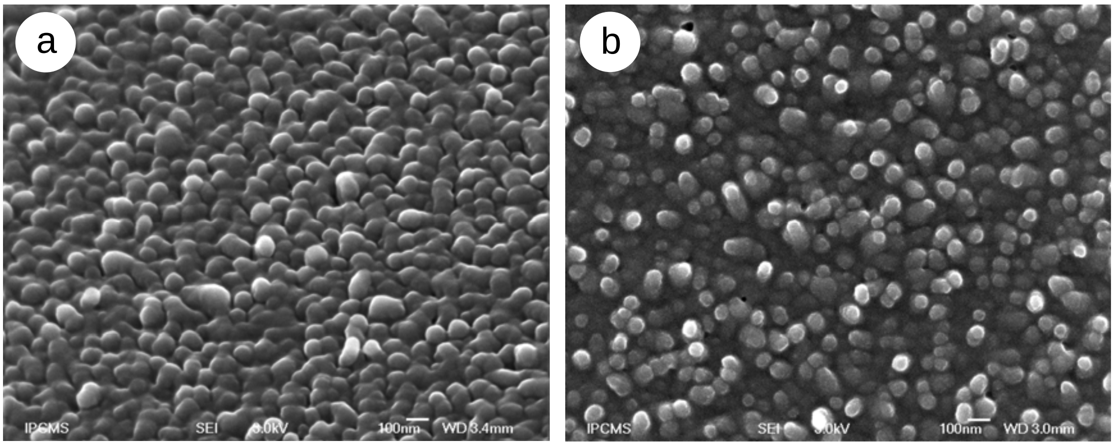
a
IPCMS SEI 5.0kV 100nm WD 3.4mm
b
IPCMS SEI 5.0kV 100nm WD 3.0mm

Fig. 4.3. *Scanning electron micrograph of (a) H_2Pc and (b) CoPc thin films of the same thickness ~ 170 nm.*

4.1.3 Atomic force microscopy (AFM)

The topography of the films observed by AFM shows that the average grain size of H_2Pc and CoPc films are 130 and 95 nm, respectively. At this stage, the root mean square (rms) roughness of the H_2Pc and CoPc films are 9 nm and 3.5 nm, respectively. This means that the surface roughness of the H_2Pc film is higher than that of CoPc as shown in Fig. 4.4a and b.

4.1.4 Transmission electron microscopy (TEM)

The electron diffraction (ED) patterns shown in Fig. 4.5a and b depict that both H_2Pc and CoPc films are α-polymorph with characteristic reflections at d_{002} = 1.18 nm, d_{004} = 0.59 nm, $d_{11\text{-}2}$ = 0.353 nm and $d_{11\text{-}3}$ = 0.327 nm for H_2Pc and reflections at d_{002} = 1.242 nm, d_{004} = 0.613 nm, $d_{11\text{-}2}$ = 0.353 nm and $d_{11\text{-}3}$ = 0.328 nm for CoPc films corresponding to the (002), (004), (11-2) and (11-3) planes [Heutz00]. The rings in the

ED pattern show that the films are textured. From the measured values of d_{200}, d_{002} and $d_{11\text{-}2}$ we can deduce the lattice parameters for the orthorhombic cell. We found *a* = 2.585 nm, *b* = 0.374 nm, *c* = 2.360 nm for H_2Pc and *a* = 2.566 nm, *b* = 0.372 nm, *c* = 2.484 nm for CoPc.

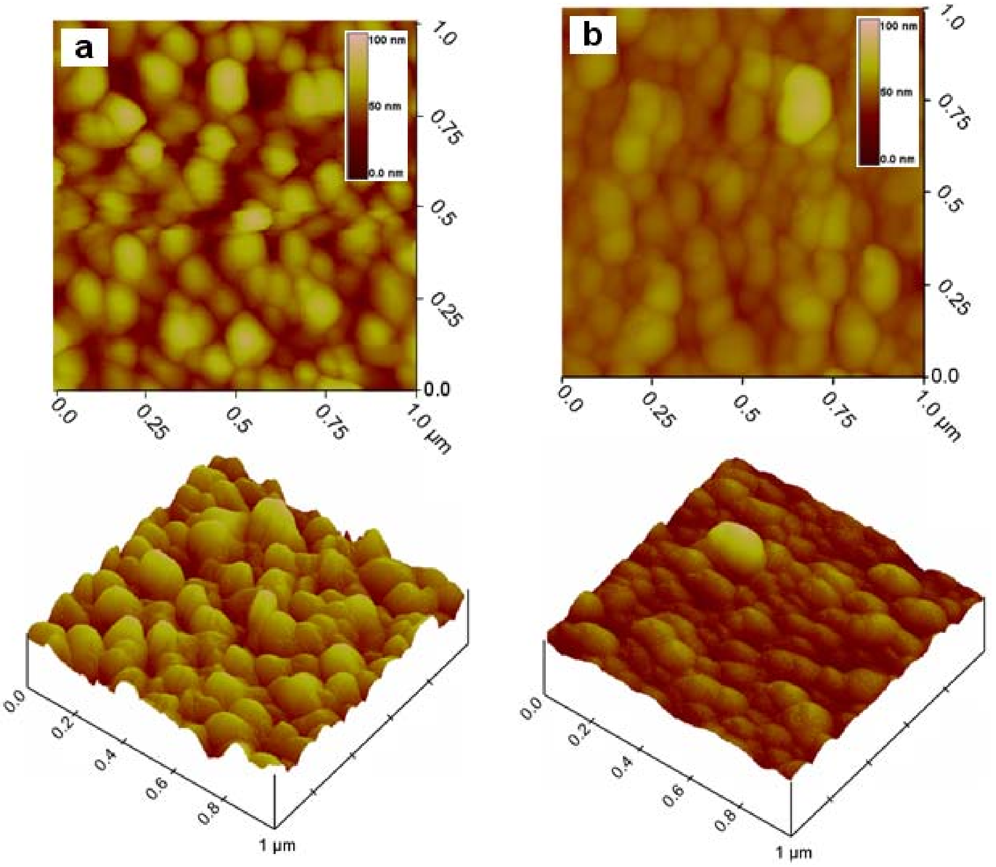
a
100 nm
50 nm
0.0 nm
1.0
0.75
0.5
0.25
0.0
0.0
0.25
0.5
0.75
1.0 µm
b
100 nm
50 nm
0.0 nm
0.0
0.2
0.4
0.6
0.8
1 µm

Fig. 4.4. *Tapping-mode AFM images of* (a) *H_2Pc and* (b) *CoPc films and their 3D images of the same thickness ~ 170 nm.*

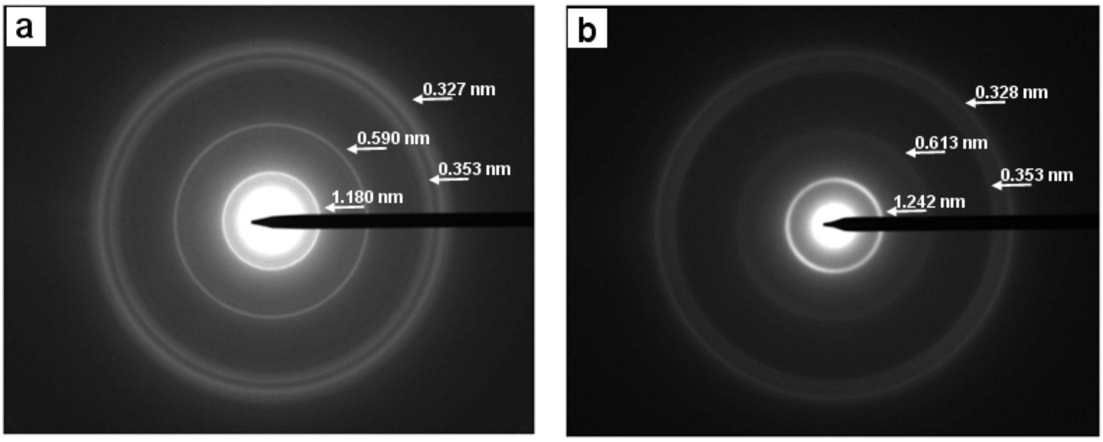
a
0.327 nm
0.590 nm
0.353 nm
1.180 nm
b
0.328 nm
0.613 nm
0.353 nm
1.242 nm

Fig. 4.5. *Electron diffraction patterns of* (a) *H_2Pc and* (b) *CoPc films.*

4.2. Optical parameters:

4.2.1 Linear absorption and reflection spectra

The absorption and reflection spectra of the H_2Pc and CoPc thin films at room temperature are shown in Fig. 4.6 Similar to many other observations [Gulbinas96], both phthalocyanine derivatives present several strong absorption bands. The Q-band in the visible region is split into two components with peaks located at 1.800 eV (688.8 nm) and 2.015 eV (615.3 nm) for H_2Pc and at 1.830 eV (677.5 nm) and 2.035 eV (609.3 nm) for CoPc. These values are comparable to those reported by Davidson [Davidson82].

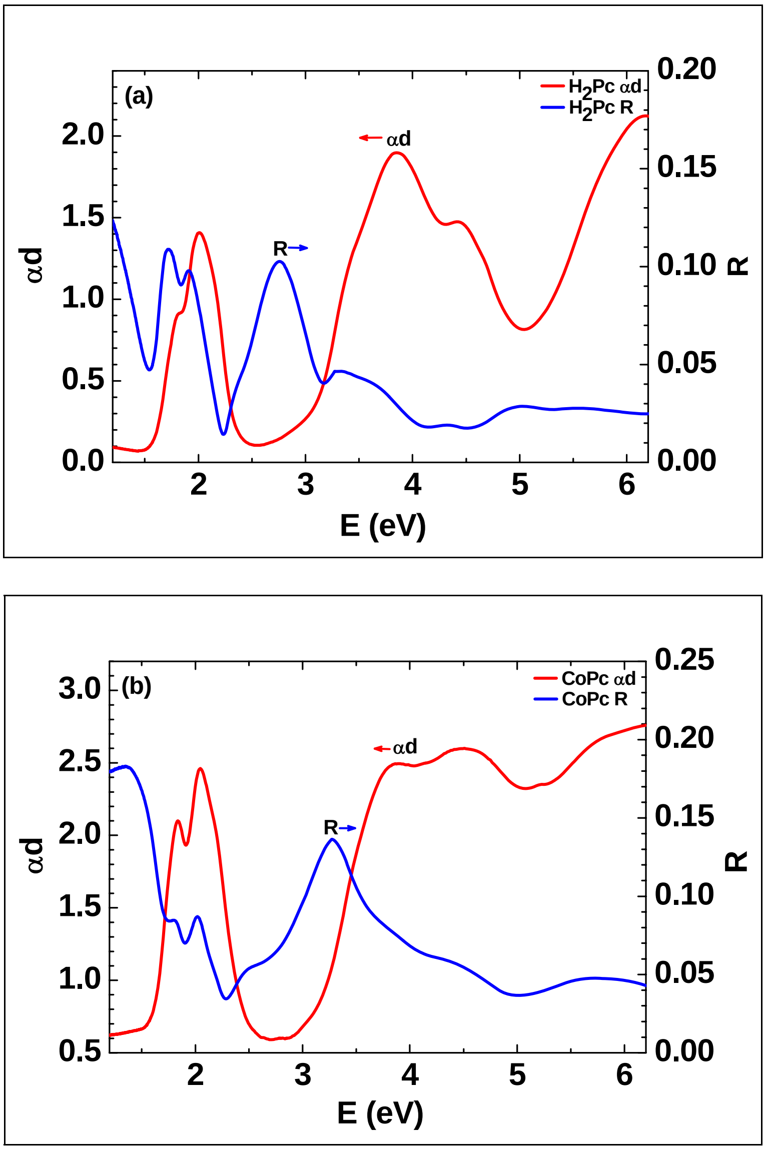

Fig. 4.6. *Absorption and reflection spectra of* H_2Pc (a) *and CoPc* (b) *films in the ultraviolet and visible regions.*

The bands are not at exactly the same positions, but those of the CoPc sample are shifted by about 20-30 meV to higher energies with respect to the H_2Pc sample. Two of these peaks are generally attributed to the first $\pi - \pi^*$ transition on the phthalocyanine macrocycle from the highest occupied molecular orbital (HOMO) to the lowest unoccupied molecular orbital (LUMO) band [Gulbinas96, Mizuguchi95, Williams92, Farag07].

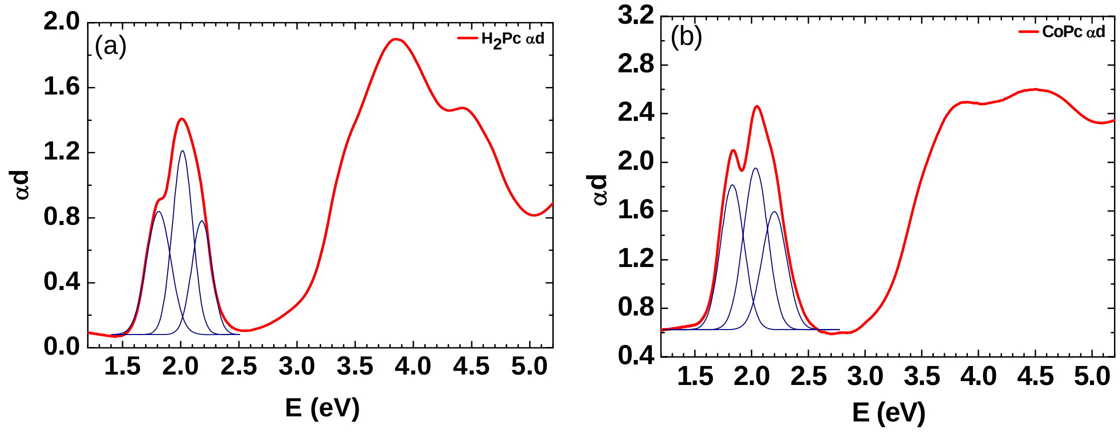

Fig. 4.7. *Absorption spectra of* H_2Pc (a) *and CoPc* (b) *films in the ultraviolet and visible regions. The Q-bands are adjusted using three Gaussian peaks.*

As discussed above, the Q-band in the visible region is split into two components with peaks located at 1.810 eV (685 nm) and 2.015 eV (615 nm) for H_2Pc and at 1.830 eV (677.5 nm) and 2.035 eV (609 nm) for CoPc. In contrast to other observations [Davidson82], the absorption spectra present, as shown in Fig. 4.7, an additional shoulder on the high energy side of the Q-bands. We have therefore fitted the Q-bands assuming the presence of 3 Gaussian peaks situated at 1.810, 2.015 and 2.180 eV (685, 615, and 577 nm) in the case of H_2Pc and at 1.830, 2.035 and 2.200 eV (677, 609, and 563 nm) for CoPc, respectively.

As shown in Fig. 4.8, the absorption spectrum of H_2Pc and CoPc in solution (using 1-chloronaphthalene, $C_{10}H_7Cl$ as a solvent) is quite different from that of the thin films in the Q-band region. H_2Pc presents two sharp peaks around 1.78 eV (696.5 nm) and 1.88 eV (659.5 nm), and CoPc presents only one at 1.84 eV (673.8 nm). All these structures are relatively narrow [Leznoff89] when compared with that of the thin solid film. The differences in the absorption position and line shape between the two molecules in solution indicate that the cobalt ion states strongly mix with the ligand π-orbitals.

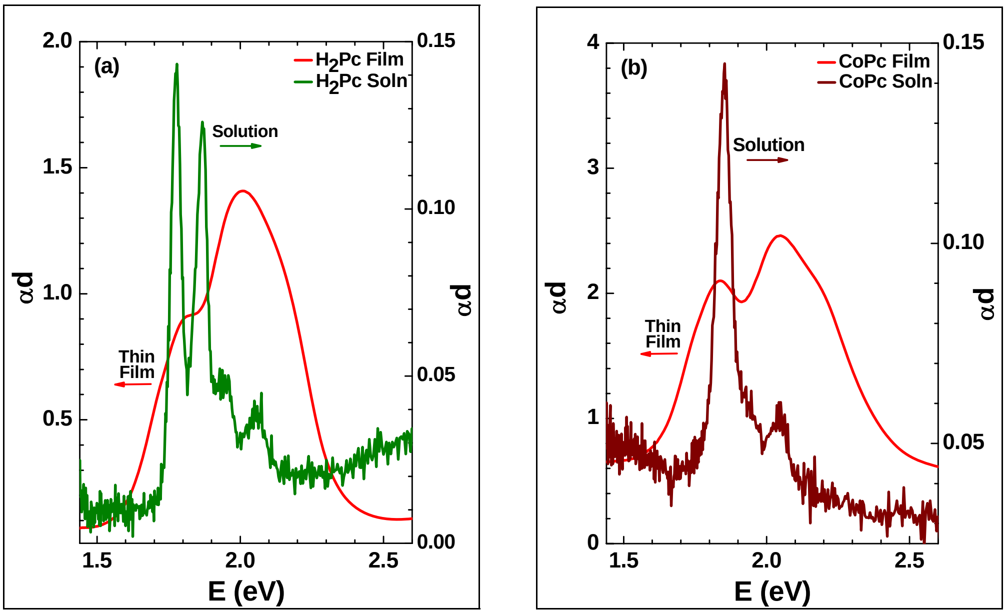

Fig. 4.8. *Absorption spectra in the Q-band region of* (a) *H_2Pc and* (b) *CoPc in solution compared to that of thin films.*

In the solid state, Pc molecules are aggregated and the Q-band becomes much broader than that of the monomer in solution [Tian98, Terasaki92, Chau93, Mizuguchi99, El-Nahas08]. This is due to strong intermolecular interactions which result in exciton coupling effects, which are present in all phthalocyanine derivatives [Chau93]. In addition, because of the interaction between molecules in the films or because of molecular distortion, the twofold degeneracy of the LUMO band is lifted into two bands with finite oscillator strength [Endo99]. Thus, transitions to both final states show up in optical measurements.

The bands are moreover strongly inhomogeneously broadened because of the molecular disorder in the layer. When substituting Co by other metal atoms, the spectral shape of the absorption remains similar with the actual metal, leading essentially to a global shift of the spectrum and some variation of the oscillator strengths of the respective transitions. The third band (corresponding to the high energy shoulders of the Q-bands) is usually assigned to be due to charge-transfer excitons (CTE) [Hirasawa04, Kobayashi04]. Its presence strongly depends on the preparation conditions of the films. In the near UV region the Soret band (B-band) shows up ~ 3.750 eV (330 nm) and the N-band at 4.420 eV (280 nm) for CoPc. These values are comparable to those reported in Ref. [Davidson82]. We will in the following restrict our studies to the spectral region of the Q-band.

4.3 Pump-and-probe measurements

As explained in section 3.7 about the setup used for the differential transmission $\Delta T(t)/T$ measurements of H_2Pc and CoPc films, we determine $\Delta T(t)/T$ for both degenerate and spectrally resolved pump-probe signals. For each time delay t between probe and pump pulses, we determined the differential transmission of the samples at room temperature. The time delays were usually varied between 0 and 50 ps, but we have also performed some measurements up to delays of 1 ns.

We measured the transmitted intensity of the probe pulses with excitation of the sample by the pump pulses ($I_t(t)$) and without excitation (I_t^0) as function of the probe photon energy. Since the spectral region of the Q-band is quite large, different series of probe-pump measurements as function of time delays had to be performed, keeping the spectrometer grating position at fixed different values. For the measurements with pump photon energy at 1.823 eV (680 nm), the grating positions were fixed at 1.823, 2.066, and 2.254 eV (680, 600, and 550 nm), which cover the spectral range of the probe beam from 1.722 eV to 2.470 eV (720–502 nm).

In the case of the pump photon energy of 2.032 eV (610 nm), the grating positions chosen were 1.653, 1.823, 2.066 and 2.254 eV (750, 680, 600, and 550 nm), which cover the detection range from 1.570 eV to 2.470 eV (790–502 nm). For successive grating positions the transmitted intensities were matched to each other in the overlapping region. We first measure the transmitted intensity of the probe pulses with excitation of the sample by the pump pulses ($I_t(t)$) and without excitation (I_t^0) as function of the probe photon energy. We then calculate the differential transmission rate by

$$\Delta T(t)/T = (I_t(t) - I_t^0) / I_t^0 \qquad (4.1)$$

as function of time delay t between the pulses. Positive values of t indicate that the pump pulses precede the probe pulses. Similar measurements of the differential transmission have been performed for several metal Pc's, showing dynamics that include bimolecular recombination processes [Mi03, Zhou04].

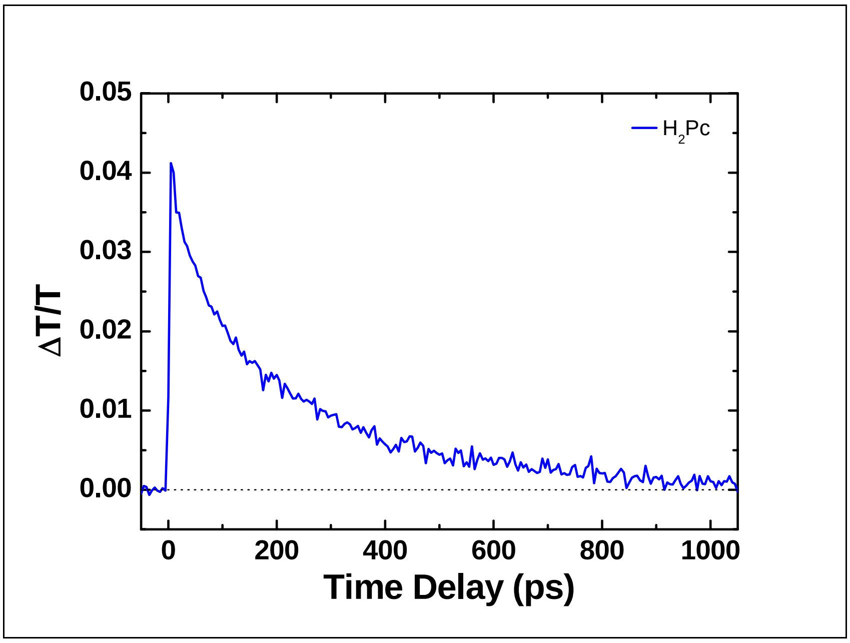

Fig. 4.9. *The bleaching dynamics of* H_2Pc *thin film.*

Figure 4.9 shows the bleaching dynamics of H_2Pc for a long time delay. We fit the differential transmission $\Delta T(t)/T$ curves measured for the H_2Pc sample by a single exponential decay and a constant contribution in the form

$$\Delta T(t)/T = A_1 \, exp\,(\,-\,t/t_1) + C \qquad (4.2)$$

where A_1, and t_1 are the contributions and lifetimes of the exponential decay and C is a constant value to which the curves converge at long time delay. It describes a slow decay process occurring in a nanosecond time range that is too long to be measured in our experiments.

In the case of metal phthalocyanine (CoPc), such a simple analysis is not sufficient since the $\Delta T(t)/T$ dynamics shows at least two different contributions on a sub-nanosecond time scale and we analyse the transmission dynamics using a double exponential decay and a constant contribution:

$$\Delta T(t)/T = A_1 exp(-t/t_1) + A_2 exp(-t/t_2) + C \qquad (4.3)$$

where A_1, A_2 and t_1 and t_2 are the contributions and lifetimes of the two corresponding components, respectively, and C is a constant contribution corresponding to a decay that is not resolved in our experiment and that gives rise to transmission change even at long delay times.

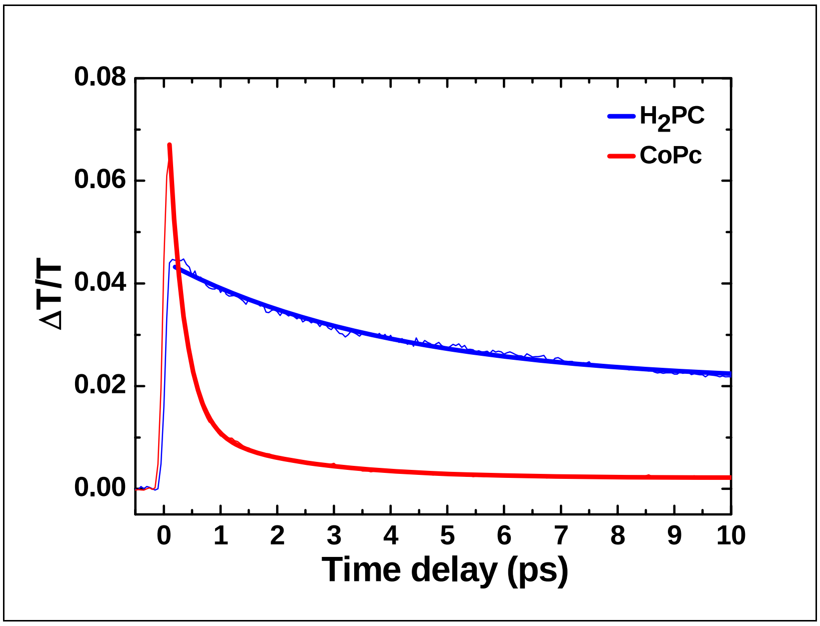

Fig. 4.10. *The bleaching dynamics of* H_2Pc *and CoPc films determined from degenerate pump-probe measurements at 2.066 eV with the pump intensity of 6.54 GW/cm*^{2}.

The relaxation dynamics of the excited states of H_2Pc and CoPc films is shown in Fig. 4.10. $\Delta T(t)/T$ is measured at room temperature by degenerate femtosecond pump-probe technique when exciting at a photon energy of 2.066 eV (600 nm). We find that the excited states for the H_2Pc film decay through two processes: a slow process on a time scale of tenths of picoseconds (ps) and a very slow process with a recovery time of several hundreds of ps as shown in Fig. 4.9. On the contrary, the excited states of CoPc decay much faster through several processes: an ultrafast process on a fs time scale, a fast one (on a ps time scale), and a long-living population with recovery time of hundreds of picoseconds.

To determine the origin of the increase of the relaxation rate when changing from H_2Pc to CoPc, we have studied the $\Delta T(t)/T$ dependence on the excitation intensity. In the degenerate configuration described above, the transient bleaching at 2.066 eV (600 nm) is measured on CoPc films when exciting with various intensities. The result is depicted in Fig. 4.11.

As shown in Fig. 4.12, the maximum of the bleaching signal varies linearly with the excitation intensity. The linear variation of the peak signal as a function of the excitation intensity indicates that the pump intensity is not high enough to give rise to saturation effects [Mi03, Zhou04]. In addition, we have fitted the curves of Fig. 4.10 using eq. (4.3).

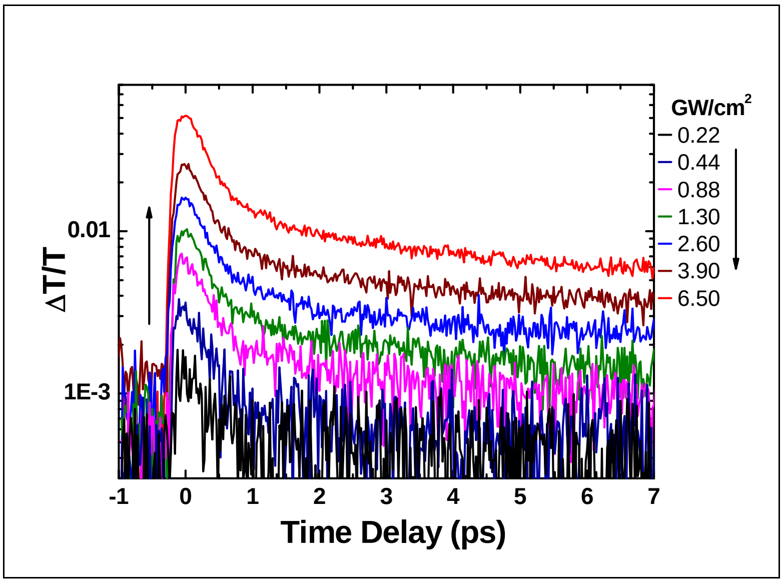

Fig. 4.11. *Excitation intensity dependence of bleaching dynamics of CoPc film at 2.066 eV (600 nm).*

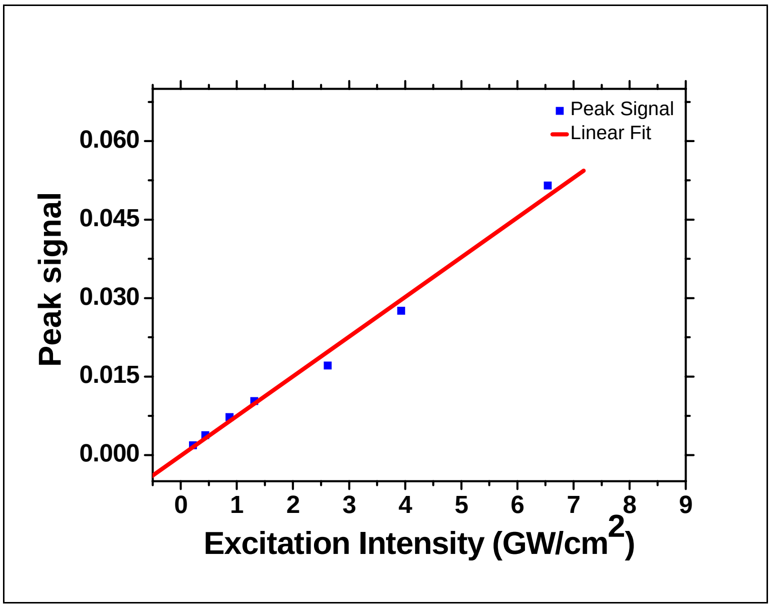

Fig. 4.12. *Peak signal intensity as a function of the excitation intensity for CoPc film.*

As summarized in Table 4.2, the values of C, A_1, and A_2 vary also linearly with excitation intensity, and those of t_1 and t_2 are almost constant. Fluctuations of t_1 with increasing intensity are not systematic and not significant. They are due to the fitting procedure and reasonable results are also obtained when fixing t_1 and t_2 at their mean value and adjusting only the amplitudes C, A_1, and A_2.

The linear variation of the peak signal with excitation intensity leads us to conclude that exciton-exciton scattering processes (which depend on the excitation intensity) are not responsible for the increase of the relaxation rates with respect to H_2Pc films. The latter scenario was observed in other metal phthalocyanine films [Mi03].

Table 4.2. *Parameters of the Decay Process of CoPc at Different Excitation Intensity for a Pump Photon Energy of 2.066 eV (600 nm).*

Excitation Intensity (W/cm^2)	C	A_1	t_1 (ps)	A_2	t_2 (ps)
0.22	0.00037	0.00014	6.2	0.00084	0.32
0.44	0.00051	0.00024	3.8	0.00253	0.36
0.88	0.00085	0.00104	3	0.00508	0.35
1.3	0.00092	0.00189	4.7	0.00803	0.34
2.6	0.00221	0.00234	2.5	0.01245	0.35
3.9	0.00335	0.00403	2.8	0.02113	0.32
6.5	0.00443	0.00829	3.8	0.04314	0.35

Let us now discuss the spectrally and temporally resolved differential transmission of the films as a function of the time delay between the pulses. Figure 4.13a and b shows the result using an excitation centered at 2.032 eV (610 nm). The different colors indicate $\Delta T(t)/T$ values in a linear scale. In the case of H_2Pc (Fig. 4.13a), variations are observed between black, corresponding to induced absorption with $\Delta T(t)/T = -0.02$, and red, corresponding to $\Delta T(t)/T = 0.02$ and indicating an absorption bleaching or induced transmission. We observe that the differential transmission rate depends on the spectral position and varies from absorption bleaching to induced absorption for both H_2Pc and CoPc as clearly depicted in Fig. 13a and b.

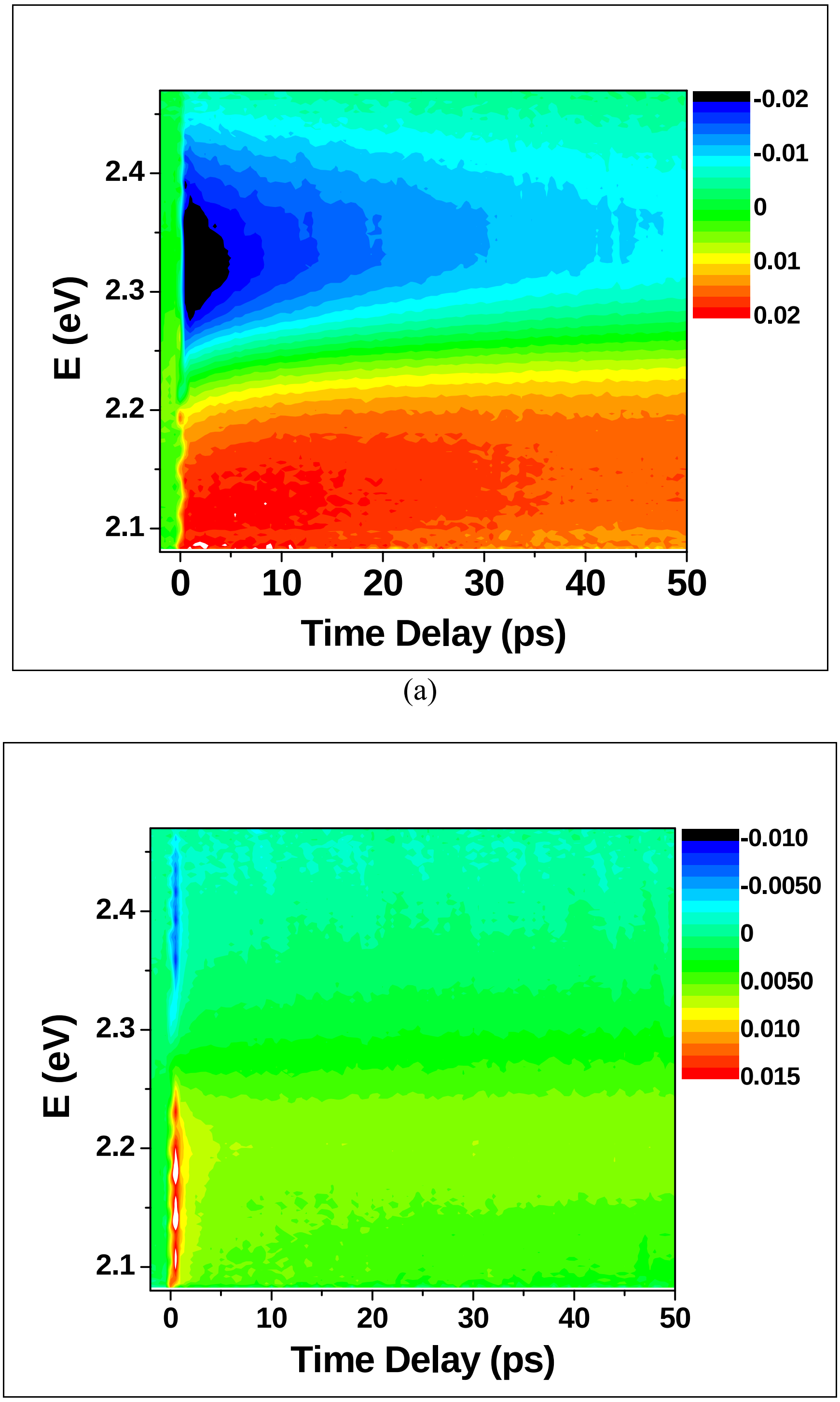

(a)

(b)

Fig. 4.13. *Differential transmission of* (a) *H_2Pc and* (b) *CoPc films as a function of the time delay between the pulses and as a function of the photon energy of the transmitted light for the spectrometer centered at 2.254 eV (550 nm). The photon energy of the exciting pump pulses is 2.032 eV (610 nm).*

The next sections will be devoted to study, in more details, the spectrally and temporally variation of the differential transmission rate *ΔT(t)/T* of both H_2Pc and CoPc when exciting at two different photon energies (1.823 and 2.032 eV) and to explain how the Co atoms affect on the excited state relaxation dynamics of the phthalocyanine films.

4.3.1 H_2Pc: Pump photon energy at 1.823 eV (680 nm)

If pump and probe pulses are overlapping in time on the sample, we observe, when plotting the differential transmission rate *ΔT(t)/T*, strong interference structures, which are due to coherent wave mixing processes [Joffre88, Brimont08]. Therefore, we restrict ourselves to positive time delays.

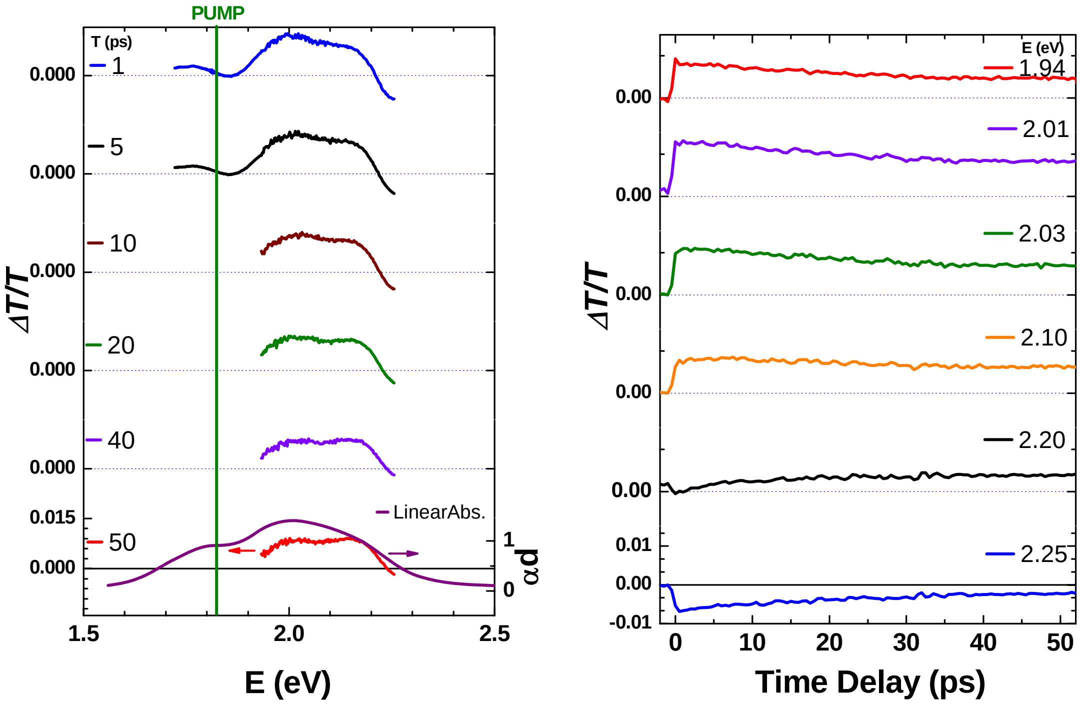

(a) (b)

Fig. 4.14a(b). *Spectral (temporal) variation of the differential transmission rate ΔT(t)/T of metal-free* H_2Pc *for several time delays (probe photon energies) when exciting at a pump photon energy of 1.823 eV (680 nm). The green line shows the central photon energy of the pump pulses. The spectral shape of the linear absorption is given for comparison.*

Figure 4.14a shows typical results of the differential transmission rate *ΔT(t)/T* of metal-free phthalocyanine (H_2Pc) as function of probe photon energy for several time delays, when exciting with a pump photon energy of 1.823 eV (680 nm). The spectra show absorption bleaching due to Pauli blocking (positive values), and induced absorption (negative values) in the region of the Q- band. The spectral shape of the $\Delta T(t)/T$ curves depend on the time delay and, for a fixed spectral position, it can turn from absorption bleaching to induced absorption in a very complex way. Such spectral variations of the time resolved absorption have already been reported for several metal-phthalocyanine films [Williams92, Mi03, Zhou04].

Here, we clearly see that the changes from absorption bleaching to induced absorption with changing the probe photon energy are not due to the metal atoms but intrinsically to the phthalocyanine molecules. When comparing, for long delays *t*, $\Delta T(t)/T$ with the linear absorption, which is given in Fig. 4.14a for comparison, we remark that, for long time delay the absorption bleaching $\Delta T(t)/T$ shows maxima around 1.990 eV (623 nm) and 2.160 eV (574 nm). Its structure is quite broad and the separation of the maxima similar to that of the linear absorption of the films. This is close to the results reported in Fluoroaluminium phthalocyanine (FAlPc) films, where the differential transmission has a similar spectral shape as the absorbance of the molecules [Williams92].

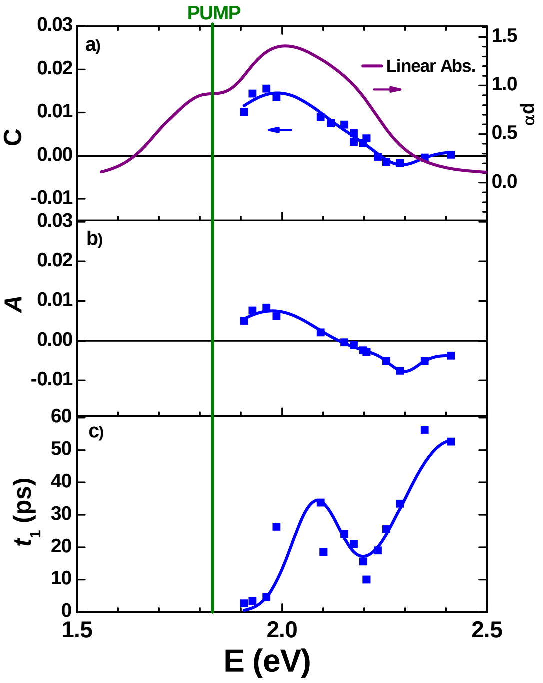

Fig. 4.15. *The constant contribution C* (a) *and the dynamical parameters* A_1 (b) *and* t_1 (c) *of* $\Delta T(t)/T$ *curves fitted with eq.* (4.2) *as function of photon energy when exciting at a pump photon energy of 1.823 eV (680 nm). The spectral shape of the linear absorption is given for comparison. The green vertical line shows the central photon energy of the pump pulses. The blue lines are guides for the eyes showing the evolution of the fitting parameters as a function of the probe photon energy.*

As shown in Fig. 4.14b, the absorption bleaching / induced absorption properties present at least two contributions, one on a tenths of ps and the other, described by the constant *C*, on a nanosecond time scale (>100 ps). This indicates that qualitatively different states are populated by the pump pulse after a relaxation process. We tentatively ascribe these states of the films as originating from molecular singlet and triplet states, which have very different lifetimes. In molecules, transitions between the series giving rise to intersystem crossing, are only weakly allowed [Lehn85, Ma61].

The result of the adjustment using eq. (4.2) is indicated in Fig. 4.15, which gives the values of *C*, A_1 and t_1 as function of photon energy. The value of the decay time is smoothly photon energy dependent and varying between 10 and 50 ps. Besides the absorption bleaching, a small induced absorption is observed around 2.3 eV. We have verified that assuming a double exponential decay (eq.(4.3)) does not improve the quality of the fit.

4.3.2 H_2Pc: Pump photon energy at 2.032 eV (610 nm)

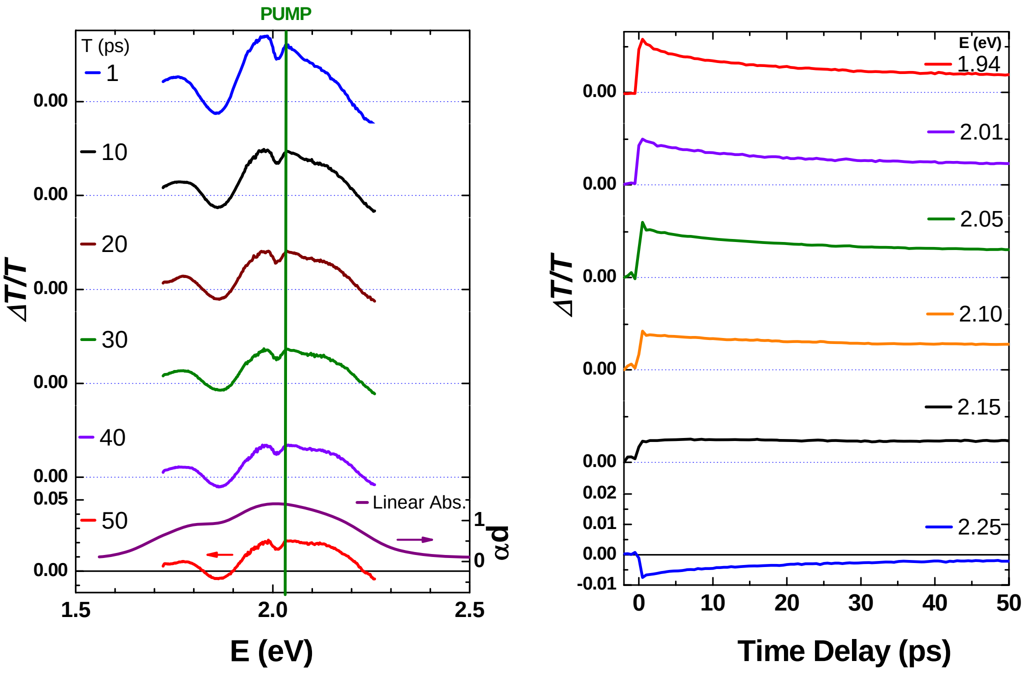

(a) (b)

Fig. 4.16a(b). *Spectral (temporal) variation of the differential transmission rate ΔT(t)/T of metal-free H_2Pc for several time delays (probe photon energies) when exciting at a pump photon energy of 2.032 eV (610 nm). The spectral shape of the linear absorption is given for comparison. The green vertical line shows the central photon energy of the pump pulses.*

When the pump photon energy is tuned to the maximum absorption of the Q-band at 2.032 eV (610 nm), the results for the differential transmission $\Delta T(t)/T$ are very similar to the former case, with nevertheless an increase of the absolute value of the differential transmission for fixed pump pulse intensity. We find that $\Delta T(t)/T = 0$ or slightly negative around 1.860 eV (667 nm) and slightly positive above 1.750 eV (708 nm). (This spectral region has not been studied in detail with the excitation conditions described in 4.3.1) The maximum observed around 1.785 eV (695 nm) is consistent with the finding mentioned above: the absorption bleaching has again a shape similar to that of the linear absorption.

When compared to 4.3.1, the only important difference is a structure, which appears at 2.015 eV (615 nm) (i.e. around the spectral position of the exciting pump pulses) as a local decrease of the induced transmission. The absorption change at this photon energy is already present 1 ps after the excitation. As shown in Fig. 4.16a, the structure has a FWHM of 26 meV and is completely absent when pumping at 1.823 eV (680 nm).

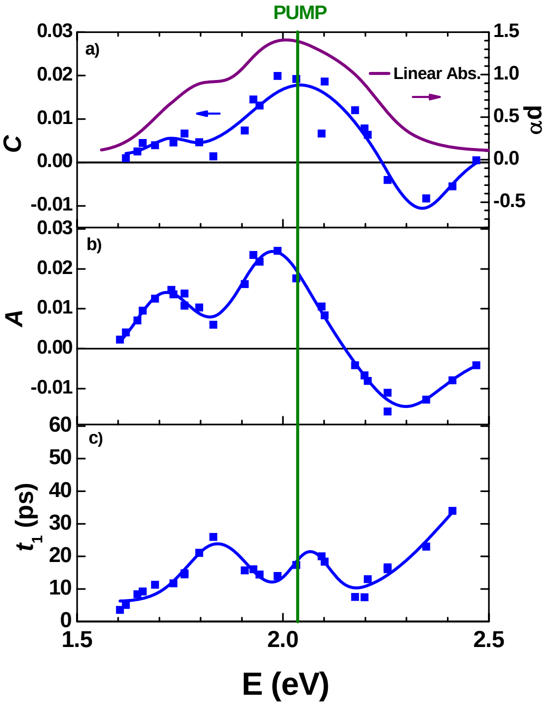

Fig. 4.17. *The constant contribution C* (a) *and the dynamical parameters* A_1 (b) *and* t_1 (c) *of* $\Delta T(t)/T$ *curves fitted with eq. (4.2) as function of photon energy when exciting at a pump photon energy of 2.032 eV (610 nm). The spectral shape of the linear absorption is given for comparison. The green vertical line shows the central photon energy of the pump pulses. The blue lines are guides for the eyes showing the evolution of the fitting parameters as a function of the probe photon energy.*

The modification of the differential transmission around 2.015 eV (615 nm) can have two possible origins: either the photon energy of the pump beam is high enough that initial states are populated, from which an induced absorption to a doubly-excited state occurs. Then, the photon energy of 2.015 eV (615 nm) corresponds to the energy of the optical transition from the first excited state to this doubly-excited state. An example would be that the population of an exciton state gives rise to an induced absorption and to create biexcitons. The other possibility is that the excited molecules can relax from states at 2.015 eV to dark states and thus diminish the absorption bleaching around 2.015 eV. In both cases, the initial states have a well defined energy since the structure at 2.015 eV has a narrow spectral width.

In addition the structure disappears also with a time constant of the order of 30 ps, lasting longer than the surrounding absorption bleaching. In any case, the comparison of the spectral shapes of the structure and that of the pump laser pulses shows that they have similar widths. We tentatively assume that the transition is resonantly excited and selected by the laser within the inhomogeneous width of the Q- bands. We have analysed the $\Delta T(t)/T$ decays using eq. (4.2) and plot the results in Fig. 4.17. Again, the result is very similar to that obtained for a pump photon energy of 1.823 eV (680 nm) and the induced absorption structure around 2.3 eV is even more pronounced.

4.3.3 CoPc: Pump photon energy at 1.823 eV (680 nm)

Figure 4.18a shows the differential transmission $\Delta T(t)/T$ as function of photon energy for several time delays and Fig. 4.18b its temporal variation for several probe photon energies when exciting the CoPc sample at a pump photon energy of 1.823 eV (680 nm). Comparing to the H_2Pc sample (see section 4.3.1), it turns out that the differential transmission dynamics has one very fast contribution (on a fs time scale), a slower part (several 10s of ps) and a sub-nanosecond contribution. In order to determine the origin of the increase of the relaxation rate when changing from H_2Pc to CoPc, we had studied the $\Delta T(t)/T$ dependence on the excitation intensity in the degenerate configuration [Gadalla10]. It turned out that the maximum of the bleaching signal varies linearly with the excitation intensity (see section 4.3) and the time constants are independent of it. On the contrary to the results discussed in Ref. [William92, Zhu04] our excitation intensity for nondegenrate pump-probe experiment (8.7 GW/cm^2) is kept such low that exciton-exciton interaction does not influence the differential transmission dynamics.

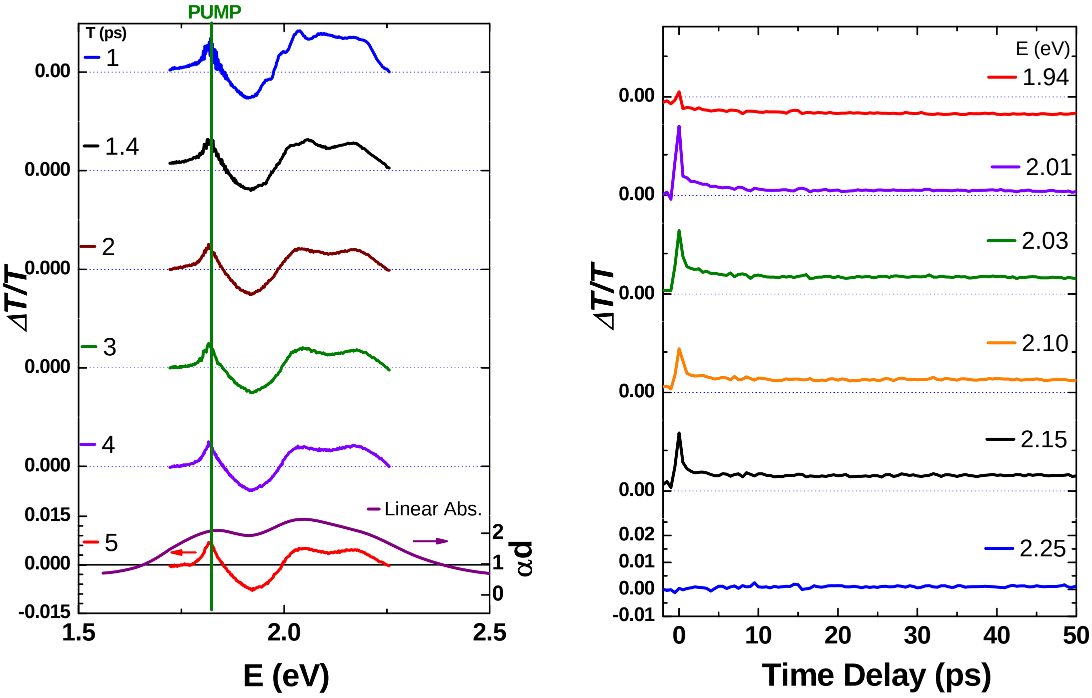

(a) (b)

Fig. 4.18a(b). *Spectral (temporal) variation of the differential transmission rate $\Delta T(t)/T$ of CoPc for several time delays (probe photon energies) when exciting at pump photon energy at 1.823 eV (680 nm). The spectral shape of the linear absorption is given for comparison. The green vertical line shows the central photon energy of the pump pulses.*

Since the ultrafast contribution is absent for H_2Pc, we attribute it to the presence of the Co atoms. This result is similar to the findings in other phthalocyanine molecules containing transition-metal ions, which where shown to accelerate drastically the relaxation dynamics of excited states [Nikolaitchik99]. This is due to the fact that coupling between the π- orbitals and the d- electrons can provide additional channels of energy relaxation or give rise to a fast relaxation via charge transfer states [Yan06, Tait83, Chung01].

As shown in Fig. 4.18a the spectrum has similar features as the H_2Pc sample but a striking difference is the presence of a strong induced absorption band which arises at 1.920 eV (646 nm) with a FWHM of 100 meV in the central part of the Q-band. It is completely absent in H_2Pc. This induced absorption builds up very rapidly (in less than 1 ps) during the excitation by the pump beam. On the contrary to the absorption bleaching in its vicinity, the $\Delta T(t)/T$ value at 1.920 eV does not evolve during the measuring time. Therefore we conclude that the population of the state giving rise to the induced absorption is saturated and constant on a timescale of the order of 100 ps. If a recombination occurs, the initial states are immediately repopulated from the other populated states. Since this induced absorption at 1.920 eV is absent in H_2Pc samples, at least one state involved in the transition has its origin in Co metal atomic orbitals. Another feature is the induced transmission signal that is localized close to the laser excitation around 1.82 eV (680 nm). It appears as a hole burning, showing again that the Q-band is inhomogeneously broadened.

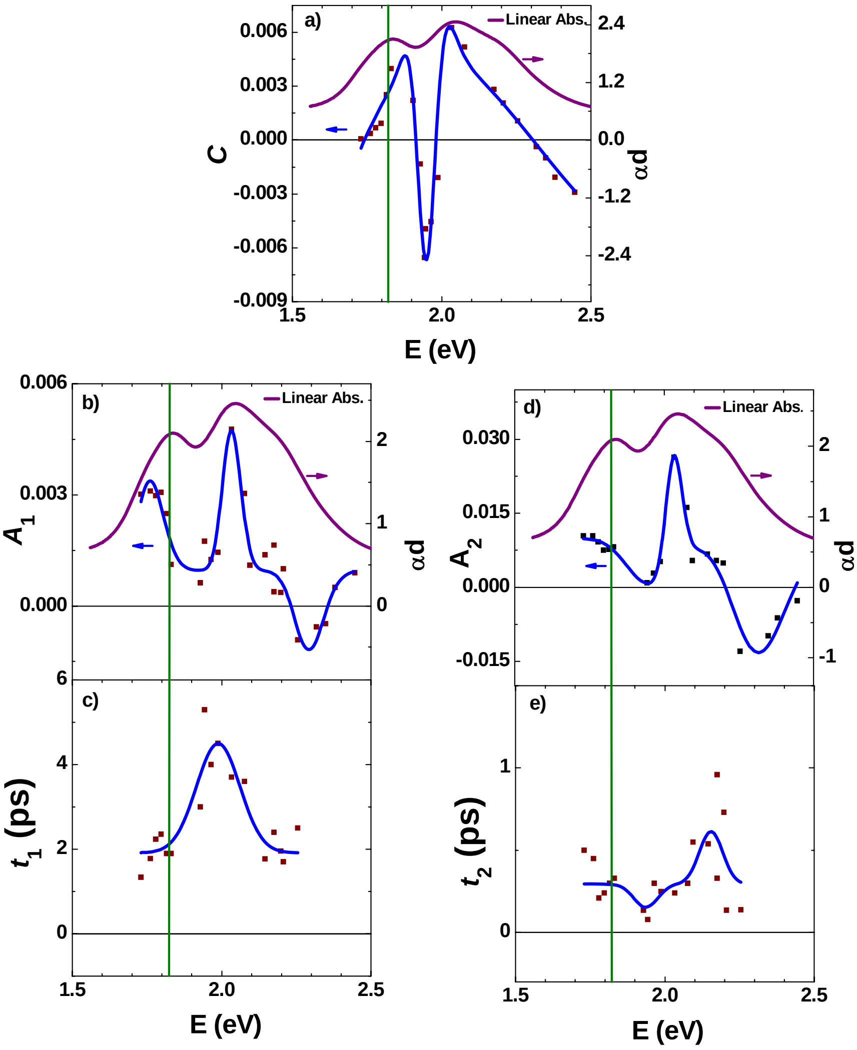

Fig. 4.19. *The constant contribution C* (a) *and the dynamical parameters* (A_1, t_1) *(Figs.* b *and* c*) and* (A_2, t_2) *(Figs.* d *and* e*) of the* $\Delta T(t)/T$ *curves fitted with eq. (4.3) as function of photon energy when exciting at pump photon energy of 1.823 eV (680 nm). The spectral shape of the linear absorption is given for comparison. The green vertical line shows the central photon energy of the pump pulses. The blue lines are guides for the eyes showing the evolution of the fitting parameters as a function of the probe photon energy.*

Figure 4.19 summarizes the temporal analysis of our results. It shows the values obtained when fitting the differential transmission dynamics $\Delta T(t)/T$ with the double exponential decay of eq. (4.3). We have verified that the use of a single exponential decay (eq. (4.2)) does not lead to a satisfactory fit of the data. Besides the strong induced absorption band, which arises at 1.920 eV in the central part of the Q-band we find an additional transient induced absorption band around 2.30 eV with a FWHM of about 100 meV, part of which vanishes on a ps timescale.

It is important to notice here that at all photon energies the $\Delta T(t)/T$ peak signal values increase linearly with increasing intensity of excitation[Gadalla10]. On the contrary to the results discussed in Ref. [Williams92, Zhou04] our excitation intensity is kept such low that bimolecular exciton decay does not influence the differential transmission dynamics and that collision between excitons are not efficient enough to modify their dynamics. This is a further argument which makes us believe that the presence of the Co atoms gives rise to a fast intermolecular excitation transfer and increases the relaxation rate as discussed above.

4.3.4 CoPc: Pump photon energy at 2.032 eV (610 nm)

Similar to Fig. 4.16a, Fig. 4.20a shows the differential transmission $\Delta T(t)/T$ of the CoPc sample as function of photon energy for several time delays when the pump photon energy is tuned to 2.032 eV (610 nm). Figure 4.20b gives its temporal variation for several probe photon energies. This spectral position is close to the maximum of the Q-band and corresponds to the maximum of absorption bleaching discussed in 4.3.3. when exciting at 1.823 eV (680 nm).

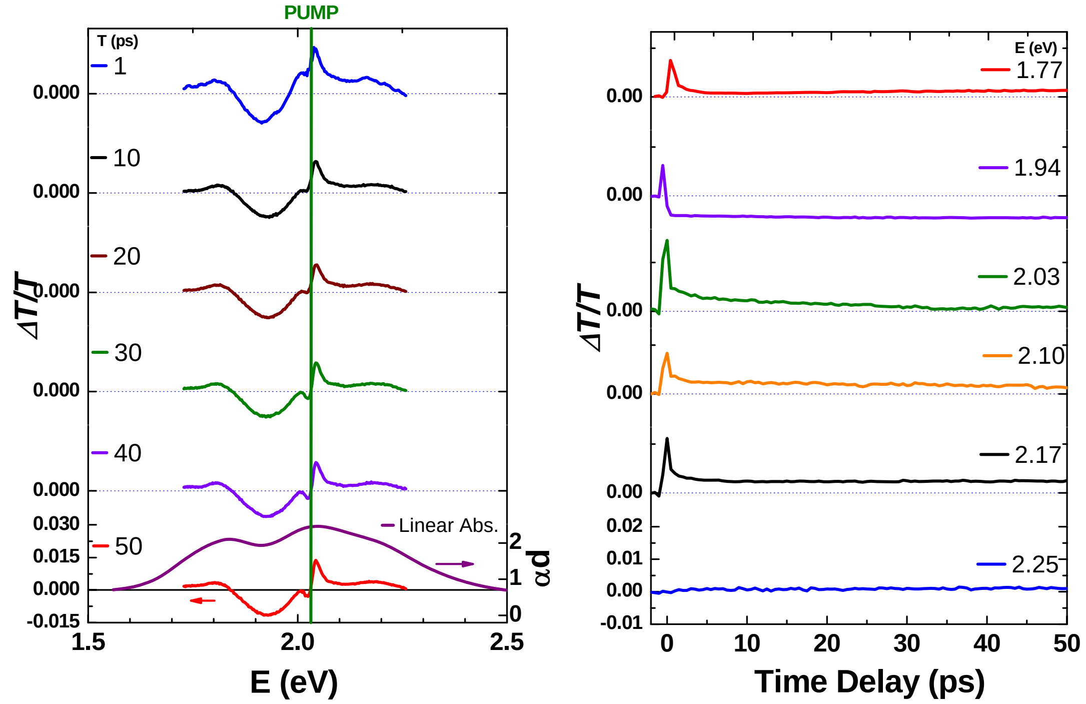

(a) (b)

Fig. 4.20a(b). *Spectral (temporal) variation of the differential transmission rate $\Delta T(t)/T$ of CoPc for several time delays (probe photon energies) when exciting at pump photon energy at 2.032 eV (610 nm). The spectral shape of the linear absorption is given for comparison. The green vertical line shows the central photon energy of the pump pulses.*

Figure 4.21 summarizes the temporal analysis of our results. As in Fig. 4.18 we show the values obtained when fitting the differential transmission dynamics $\Delta T(t)/T$ with the double exponential decay of eq. (4.3). The results are similar to those obtained in 4.3.2. Besides the induced absorption bands at 1.920 eV (646 nm) and around 2.30 eV (539 nm) discussed above, which have a long lifetime or are vanishes on a ps timescale, respectively, we find an additional induced absorption band centered between 1.63 and 1.710 eV (761 to 725 nm), which was not studied in 4.3.3. In the transient region, its time constant is quite long, ranging from several ps up to 100 ps at its maximum.

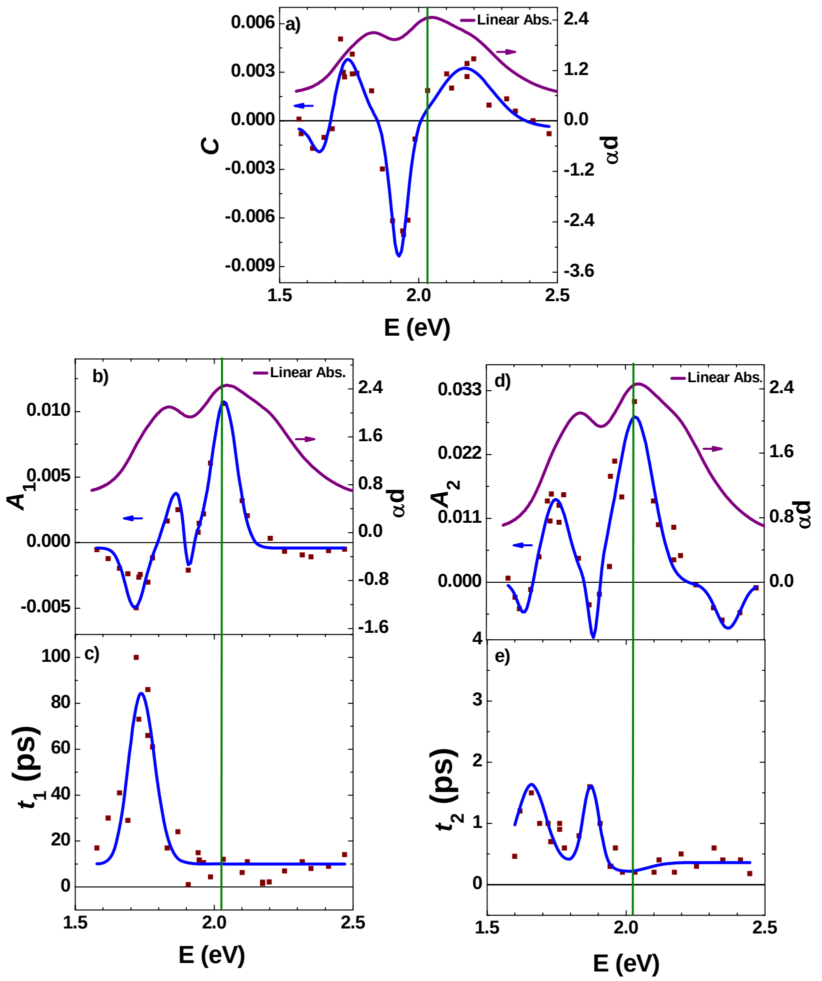

Fig. 4.21. *The constant contribution C* (a) *and the dynamical parameters (A_1, t_1) (Figs. b and c) and (A_2, t_2) (Figs. d and e) of the ΔT(t)/T curves fitted with eq. (4.3) as function of photon energy when exciting at pump photon energy of 2.032 eV (610 nm). The spectral shape of the linear absorption is given for comparison. The green vertical line shows the central photon energy of the pump pulses.*

4.4 Comparison between H_2Pc and CoPc relaxation dynamics

The $\Delta T(t)/T$ relaxation dynamics of the H_2Pc sample is summarized in Fig. 4.22a for several time delays as function of photon energy. It indicates that the transmission changes cover the entire Q-band of the thin film: There is absorption bleaching at certain photon energies and induced absorption in the high photon energy range of the Q-band. Nevertheless, two features dominate the spectra. First, broad induced transmission signals can be observed. They coincide approximately with the two wide absorption bands centred respectively at 1.800 eV (688.8 nm) and 2.015 eV (615.3 nm). Superimposed, an induced absorption signal appears as a hole in the previous band. It is located close to the laser excitation and shows a narrow linewidth.

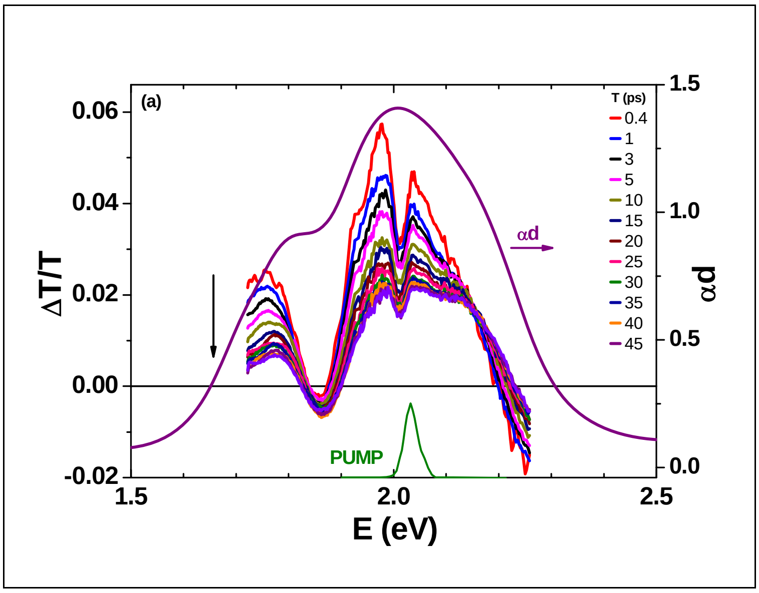

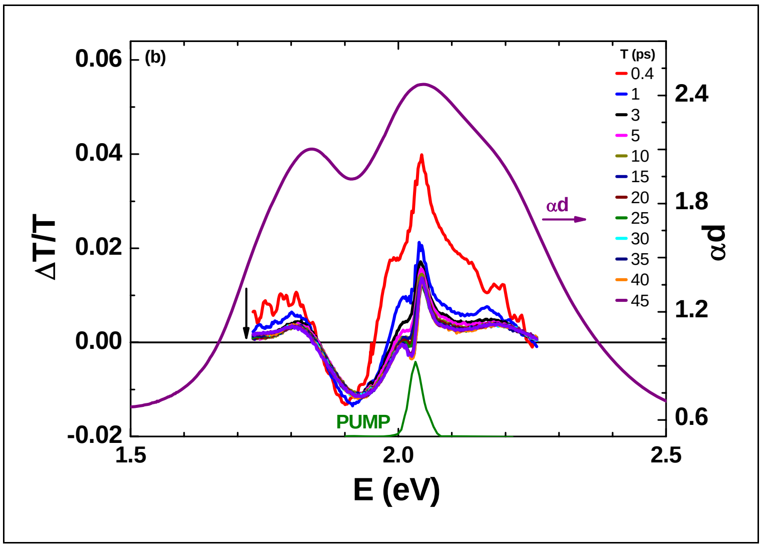

Fig. 4.22. *Spectral variation of the differential transmission rate of* (a) *H_2Pc and* (b) *CoPc films probed at different energies of ~1.5-2.5 eV (826–496 nm). The photon energy of the exciting pump pulses is 2.032 eV (610 nm). The pump spectral shape is shown on the bottom of the graph (green line), and the purple curves show the linear absorptions of the samples. The black vertical arrow indicates the direction of longer delay time.*

Concerning CoPc, we observe from Fig. 4.22b that there is an induced transmission change in the spectral region of the Q-band as in the case of H_2Pc. One notices the presence of a stronger induced absorption around 1.93 eV (642.4 nm), that is, in between the two absorption maxima of the Q-band. As observed previously in Fig. 4.13a and b, the signal decay is faster than that in the case of H_2Pc. Another difference is the shape of the spectrally narrow feature observed close to the excitation pump laser. It evolves more slowly and shows an asymmetrical shape. These differences can be attributed to the presence of Co atoms in the phthalocyanine matrix.

In both cases, there is a broad induced transmission signal and a sharper induced absorption signal. The latter is situated close to the pump excitation energy. As shown in Fig. 4.8, the Q-band of the phthalocyanine film is strongly broadened. This is due to intermolecular coupling that gives rise to a band of delocalized states. As shown in Fig. 4.22, this band can be saturated leading to an induced transmission signal. On the other hand, the strong disorder that is usually observed in phthalocyanine films should give rise to a strong inhomogeneous broadening of the optical transitions. This can explain why a spectrally localized induced absorption is observed: The exciting pump laser spectrally selects the levels that are involved in this signal.

In addition to the features discussed above, the spectrum shows an asymmetric band, which develops around 2.040 eV (608 nm), i. e. around the photon energy of the exciting pump pulses. It has the shape characteristic of a Fano-type resonance [Fano 61] with a negative asymmetry parameter q. We have carefully verified that the structure observed here is not due to residual light from the laser excitation. As it is shown more clearly in Fig. 4.22b, the structure evolves in time. We isolated approximately the Fano resonance from the background in the following way: we took the data of Fig. 4.18a for a delay of 5 ps and multiply them by a factor such that the curves coincide at the maximum of the induced absorption band at 1.920 eV (646 nm). This gives approximately a reference curve if the Fano resonance is absent. We then determined the difference between the curves of Fig. 4.22b and the reference curve and obtained the set of curves shown in Fig. 4.23b. We have fitted them using the formula of Fano:

$$\Delta\alpha^{F} = \frac{q^{2} - 1 + 2q\varepsilon'}{1 + \varepsilon'} \qquad (4.4)$$

and $\varepsilon' = \dfrac{E - E_{\varphi} + F}{{}^{1}\!/_{2}\Gamma}$

where ε' is the photon energy of the probe photons, E_{φ} that of the resonance, Γ a damping constant, F represents a shift of the resonance position with respect to E_{φ} and q is the Fano asymmetry factor.

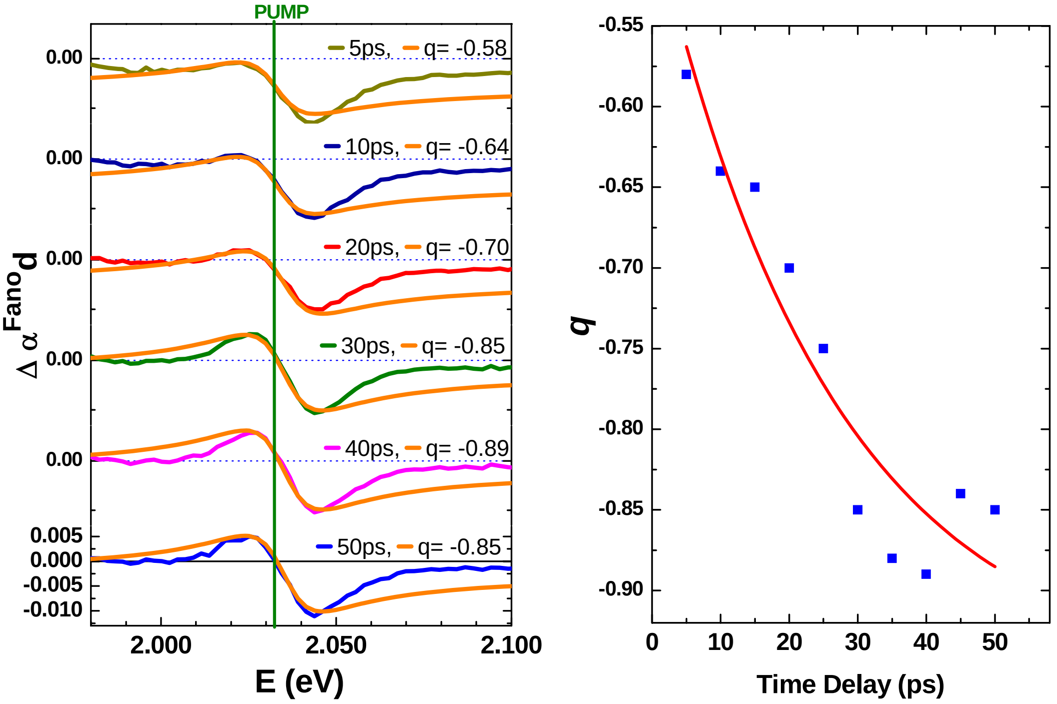

(a) (b)

Fig. 4.23. (a) *The Fano absorption for CoPc using a pump at 2.032 eV (610 nm) and* (b) *the variation of q with the time delay. The green vertical line shows the central photon energy of the pump pulses.*

We find a constant value for the damping $\Gamma = 0.020$ eV. A shift (given by F) of the resonance can be neglected. The asymmetry factor q, however, decreases in time. It has fully developed after about 30 ps, and remains stable up to 50 ps. Figure 4.23b shows the resulting time dependence of q.

In order to describe the induced transmission structures of H_2Pc and CoPc films, a model, depicted in Fig. 4.24, is suggested. This model shows states of the film originating from the HOMO molecular states (S_0) and from molecular excited states (S_1, CT, T_1). They have partly kept their molecular orbital characteristics: optical transitions to states originating from molecular singlet states are allowed and those deriving from triplet states are forbidden.

The optically allowed states are split into two bands, originating from the HOMO - LUMO transitions in the molecules. They are labelled S_1^0 and S_1^1 but, if we do not differentiate between them, S_1. A multitude of vibronic states is associated with each electronic state of the molecule. The vibronic states are indicated by the thin lines above each of the thicker ones representing the zero-vibration electronic states [Hirasawa04].

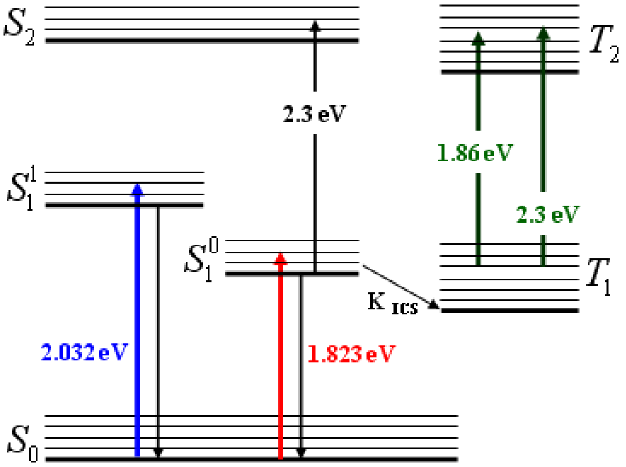
S_2
S_1^1
S_1^0
S_0
T_2
T_1
2.3 eV
1.86 eV
2.3 eV
K ICS
2.032 eV
1.823 eV

(a) H_2Pc

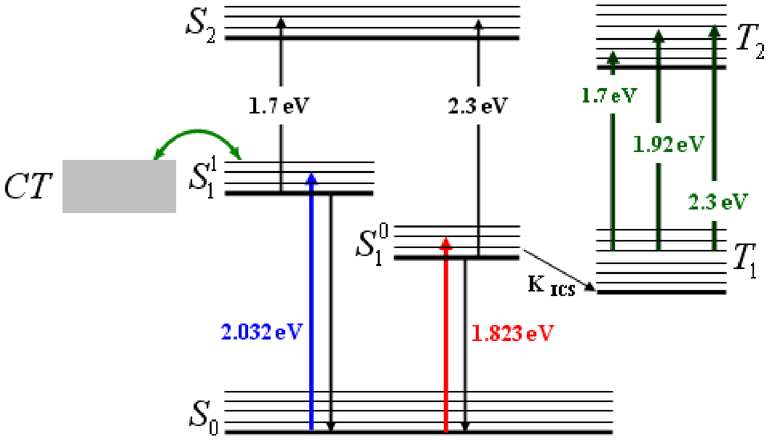
CT
S_2
S_1^1
S_1^0
S_0
T_2
T_1
1.7 eV
2.3 eV
1.7 eV
1.92 eV
2.3 eV
K ICS
2.032 eV
1.823 eV

(b) $CoPc$

Fig. 4.24. *Energy-level model of* (a) H_2Pc *and* (b) *CoPc describing the induced absorption and induced transmission.*

The S_0 to S_1 transitions correspond to the Q- band which has its absorption maxima at 1.823 eV and 2.032 eV, respectively. The Q- band and the states involved are inhomogeneously broadened due to the interactions of the molecules forming the films and to their various orientations.

Similar to triplet states in the molecule, the first T_1 state is lying energetically below the first excited optically active state S_1^0. The states T_1 can be considered as a permanent long-lived state, as relaxation to the ground state needs a spin-flip [Schell98] in the case of molecules. Under photo-excitation in the visible region, the incident photon excites the molecules to one of the vibronic sub-states of $S_{1.}$ Some part of the molecules undergo intersystem crossing to the long-lived T_1 state (>100 ps), the rest relaxes directly back to the ground state S_0. As discussed in Ref. [Yan06 and Antipas83], the presence of charge transfer states (CT) may increase the intersystem crossing rate. Such polar CT states have been identified in Phthalocyanine thin crystalline films by electroabsorption [Saito93] or electroreflectance [Yoshida86] measurements. They are not present in amorphous films where only localized Frenkel excitons have been observed [Saito93]. Charge transfer exciton states are less important in H_2Pc than in CoPc films because of the unpaired electron in the latter material.

Differential transmission changes lead either to absorption bleaching or to induced absorption. Absorption bleaching is obtained due to Pauli blocking in the S_0 states. Induced absorption is due to excitons in the S_1 state shortly after photo excitation (and at long delay times to those in the T_1 state) involving transitions between S_1 and higher energy singlet states S_2 (or the T_1 state and higher energy triplet states T_2). The absorption bleaching may follow more or less the spectral shape of the linear absorption of the crystallized material, while the induced absorption bands involve states, which do not contribute to the linear absorption spectrum but to states, populated after the pump pulse excitation. Bleaching and induced absorption of the charge transfer states are not considered in our model.

In Fig. 4.24 we have discussed a Fano type absorption structure, which is induced by the pump beam around 2.040 eV. It evolves on a long lasting time scale. Since the singlet contributions to the differential transmission are on ps to 10 ps time scales (Fig. 4.21) we attribute it also to the triplet manifold. In optical experiments, a Fano resonance results usually from quantum interference between two different transitions. One, for example, from the ground state of a system to a discrete state, the other to a continuum of states in which the discrete state is embedded and to which it is coupled [Fano61]. Since the interference changes rapidly with energy when passing the resonance of the discrete level, an asymmetric line shape is obtained, depending on the oscillator strength of the transition.

The Fano effect was first introduced when analysing the inelastic scattering of electrons by He atoms. In this case, a 2s2p level (discrete state) of double excitation He was observed, which autoionizes to a He^+ (1s) ion and a free electron (continuum of states). It has been shown that the formalism also applies to other, very different systems: e. g. when analysing transitions of impurity states embedded in a vibronic continuum of states [Sturge70] or to situations where the continuum is due to a vibronically large charge transfer states [Zhou97].

These examples are taken from linear spectroscopy studies, but the Fano effect shows also up in nonlinear spectroscopy [Zhang06, Kroner08]. In our case, the Fano resonance is not observed in linear absorption since the triplet states are not optically active. It shows up in our pump-probe experiments after excitation by the pump beam. We tentatively explain its observation in the CoPc layers in the following way: In the case of CoPc, several metal 3d-like orbitals are located near the Pc HOMO orbital, such that the HOMO of CoPc molecules is of metal $3d_\pi$ and $3d_z$ type [Liao01, Derkowska07].

The $3d_\pi$ orbitals (as the π- orbitals of the Pc molecules) lie within the plane of the molecules. The $3d_z$ Co atomic orbitals, however, are orientated perpendicular to the molecular plane and extend further outside when compared to the Pc orbitals. They may give rise to a delocalized exciton state (DE), which allows efficient excitation energy transfer in the crystalline film, perpendicular to the molecular planes. As other resonances in the film, the DE states may be inhomogeneously broadened. In that case, similar to spectral hole burning, we suppose that the pump pulse populates selectively those DE states which are in resonance with its photon energy.

4.5 Conclusion (Part I)

This study presents the structural and optical properties and the ultrafast dynamics of H_2Pc and CoPc films of thickness ~ 170 nm prepared on fused silica substrate at room temperature. The XRD, AFM and TEM electron diffraction patterns show that both H_2Pc and CoPc films are polycrystalline and have orthorhombic α-polymorph structure.

4.5.a H_2Pc: Induced transmission changes

As discussed above, the differential transmission $\Delta T(t)/T$ relaxation dynamics of H_2Pc can be analysed in the framework of eq (4.2), considering a constant contribution and another contribution, decaying exponentially in time. The results of the adjustment are summarized in Figs. 4.15 and 4.17 for excitation photon energies of 1.832 eV and 2.032 eV, respectively. We suggest in the following that the constant contribution to the differential transmission change is the signature of the triplet states and the time dependent one that of the singlet states. Around their maxima, both contributions C and A follow nicely the linear absorption spectra, indicating that the induced transmission is due to a bleaching of the ground state S_0 through the pump pulse excitation.

The molecules excited in the S_1 states either recombine back to S_0 or populate the triplet states after an intersystem crossing. In this case they may pass through CT states [Kobayashi04, Chung01]. In addition, we observe at energies around 2.3 eV an absorption increase, which is slightly different for the two contributions. It can be due to transitions between single and double excited states, which are different in both subsystems (singlet or triplet). This difference in induced absorption can also be at the origin of the slight red shift of the singlet contribution when compared to the triplet one. An additional induced absorption around 1.86 eV is observed in the triplet but not in the singlet subsystem.

The main difference between Figs. 4.14 and 4.16 is a slight structure, which shows up around 2.015 eV when exciting at 2.032 eV, and which does not considerably change with time delay. As mentioned above, the absorption linewidth of the molecule in solution as well as that of the pump laser pulses are close to the width of this structure. It is thus a signature of a selective excitation inside the inhomogeneously broadened Q- band.

4.5.b CoPc: Induced transmission changes

As stated above, when phthalocyanine molecules are modified by adding Co atoms, the samples show a much faster recombination dynamics [Yan06, Tait83, Chung01]. Due to an admixture of Co states, the HOMO states of the molecules are drastically modified when compared to H_2Pc orbitals. This admixture is resonantly enhanced since the HOMO states are almost degenerate with the Co $3d^7$ states [Liao01]. This modification leads to a global reduction of the relaxation time in the entire Q-band. It ranges from about ~ 0.3 ps to several ps, which is fast when compared with H_2Pc, and has an average relaxation time constant ~ 20 ps. In addition, the charge-transfer states are different in CoPc and H_2Pc. As discussed in Ref. [Hirasawa04 and Kobayashi04], they result in strong coupling between neighbouring molecules in the plane of the films in metal phthalocyanine. They contribute to the linear absorption spectrum in the high photon energy side of the Q-bands. These states are optically active and form a continuum that is degenerate with the Pc exciton transitions [Chung01], i. e. around 2.032 eV (610 nm) in our experiments.

Besides the increase of the relaxation rate due to the Co atoms, the most striking difference in the induced transmission spectra is the appearance of the important induced absorption band with its maximum at 1.920 eV (646 nm). When comparing Figs. 4.19 and 4.21, we can see that it shows up in the constant contribution to the $\Delta T(t)/T$ relaxation dynamics while it is absent in Figs. 4.15 and 4.17. We therefore attribute it to an induced absorption involving the triplet states modified by the Co atoms. This resonance is almost absent in the singlet manifold. After excitation by the pump beam, the triplet population is saturated and if these states recombine, they are immediately refilled from other populated states. In addition, the induced absorption around 2.3 eV in the singlet manifold, which is already observed in H_2Pc, is more pronounced due to the presence of the Co atoms.

As indicated in Fig. 4.24b, the delocalized (DE) states are degenerated with the singlet Pc exciton states in the high energy part of the Q- band. Since both systems are strongly coupled via the CT states, they develop into a strongly mixed Pc and delocalized exciton state. Thus, oscillator strength is transferred from the Pc exciton states to delocalized state and the optical transitions in the vicinity of the laser photon energy are modified. This results into an induced transmission change, which has the shape of a Fano-type resonance where the asymmetry value of q is time dependent. This effect is absent in the H_2Pc films where the coupling between molecules in adjacent planes is much smaller. Our model is quite similar to the one proposed in Ref. [Zhou97] where the vibronically broadened CT states play the role of the continuum and a pure molecular exciton state is the discrete state. In our case, however, the discrete state cannot be a selectively excited singlet exciton state since it has a very short relaxation time. Pure molecular triplet states can also be excluded since they give rise to spectrally broad bands.

Chapter
5
Results and Discussion
Part II
GaN/AlGaN QW

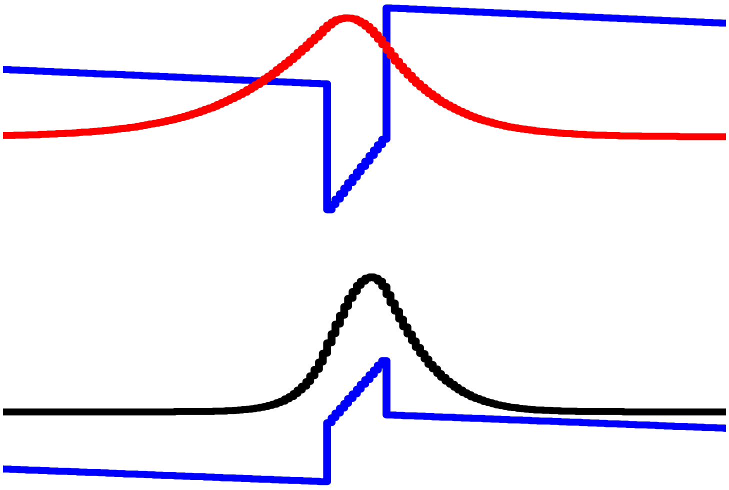

GaN/AlGaN Quantum Well

Chapter 5

Results and discussion (Part II): GaN/AlGaN Quantum Well

5.1 Sample characteristics

The sample is a GaN/AlGaN quantum well (QW) grown by metal organic vapor phase epitaxy (MOVPE) on *c*-plane sapphire substrate. The template is composed of a standard 3 µm GaN buffer layer and a 200 nm thick $Al_xGa_{1-x}N$ layer. A single GaN QW with a thickness of 2.6 nm was then deposited and capped with a 50 nm thick $Al_xGa_{1-x}N$ layer with x = 5%. Its schematic design is shown in Fig.5.1.

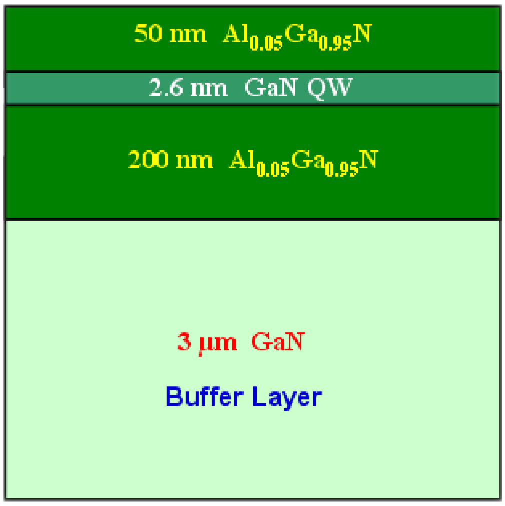

Fig. 5.1. *Schematic drawing of our GaN/AlGaN quantum well structure.*

5.1.1 Linear Spectroscopy

The linear reflectivity and photoluminescence (PL) spectra of the GaN/AlGaN QW are shown in Fig. 5.2. These spectra, taken at the same position on the sample at 10 K, show that there are three different regions on the reflectivity spectrum: the sharp spectral structures at 3.49 eV are related to the A- and B- excitons in the GaN buffer layer, two spectral structures (HH_1 and LH_1), characteristic of the QW excitons, are centered at 3.54 eV above the GaN bandgap. These excitons are built from the first heavy- and light- hole confined states (HH_1 and LH_1) but share the same first confined electronic state e_1. Their energies are split by 10 meV and the AlGaN barrier also presents a reflectivity signature at 3.59 eV.

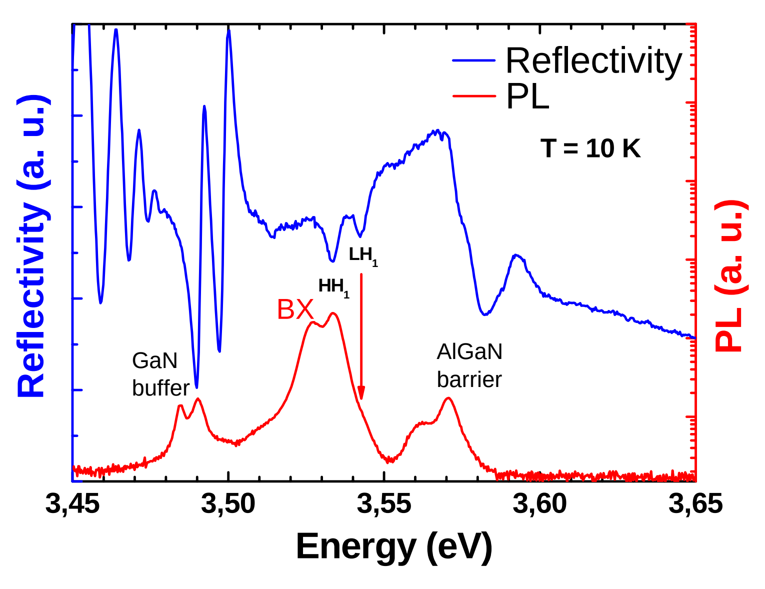

Fig. 5.2. *Linear reflectivity and photoluminescence (PL) spectra of GaN/AlGaN QW.*

The barrier PL shows a Stokes shift probably because of exciton localization on alloy disorder. While the two excitons HH$_1$ and LH$_1$ are observed in the reflectivity spectrum, only HH$_1$ is quite visible in the PL spectrum and LH$_1$ appears only as a shoulder on the higher energy side of HH$_1$ (marked by the arrow in Fig. 5.2) likely due to thermalization effects. We will see in the following that the line labelled BX 10 meV below the HH$_1$ line can be attributed to the recombination of biexcitons in the QW. The features visible on the low-energy side of the PL spectrum (3.9 eV) can be explained as follows: one is in resonance with the sharp spectral structure in the reflectivity spectrum which is attributed to the A- exciton of the GaN buffer layer and the lowest energy PL-band is ascribed to two independent contributions, namely, the biexciton and the neutral donor bound excitation of the GaN buffer layer, which spectrally overlap [Martin06].

In order to indentify with no ambiguity the PL lines, we performed PL measurements as a function of the excitation power. As described above for the photoluminescence spectrum shown in Fig. 5.2, Fig. 5.3 shows the PL spectra at different excitation intensities at temperature of 4 K when exciting at a photon energy of 3.542 eV. The PL shows three different regions: the GaN buffer layer, the quantum well centered at 3.54 eV, and the AlGaN barrier at higher photon energies. We subtract the background and use Gaussian functions to fit the X and BX bands. This fitting procedure was repeated for all spectra at different excitation power (from P_0 up to $P_0/512$). We have found that the PL intensity of the X line increases linearly in the beginning with increasing excitation power and tends to saturate as it is expected for exciton recombination.

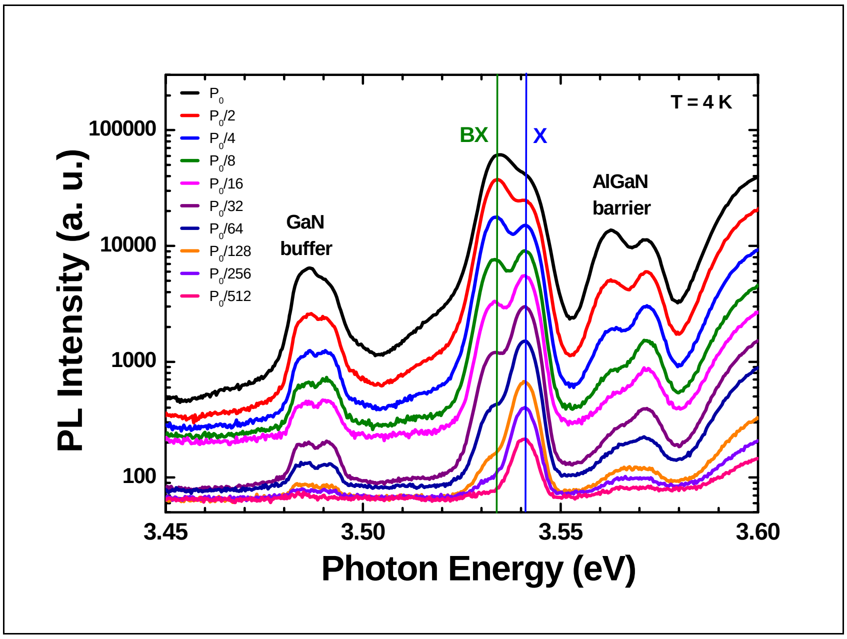

Fig. 5.3. *PL at different excitation intensities of GaN/AlGaN QW when exciting at a photon energy of 3.542 eV at* T= 4 K.

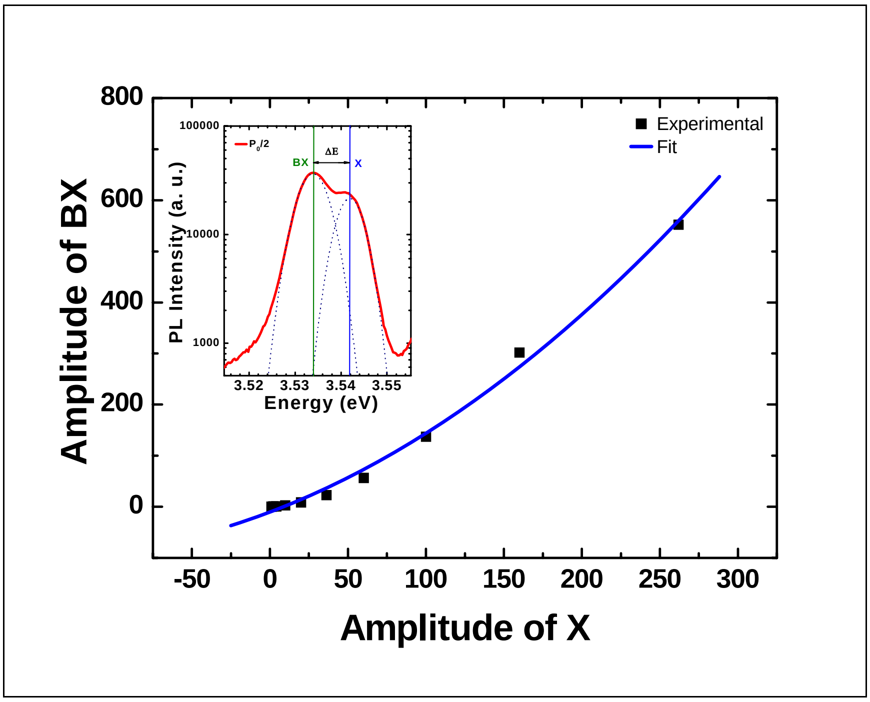

Fig. 5.4. *The amplitude of the Gaussian fit for the biexciton (BX) as a function of that of the exciton (X) of GaN/AlGaN QW at different excitation intensities. The inset shows the spectral fitting of the X and BX bands in the QW.*

The dependence of the amplitude of the Gaussian fit for the BX line as a function of that of the exciton (X) at different excitation intensities varies with the order of 1.56 as shown in Fig. 5.4. This result indicates that the BX lines due to biexciton recombination as previously observed in similar QWs [Stokker08]. The fact that the biexciton density does not vary as the square of the exciton density can be explained by considering that the exciton and the biexciton have short recombination times when compared to the thermalization time of populations [Gourley82, Yamada04]. The energy difference between the Gaussian fits of both X and BX bands was taken as biexciton binding energy (ΔE), as shown in the inset of Fig. 5.4. It has the value of ~ 8 meV which is comparable to the result of Stokker-Cheregi et al. [Stokker08].

The barrier PL exhibits a low energy tail that could be due either to exciton localization by alloy disorder or to biexciton recombination. To clarify this point, we have studied how the intensity of the low energy component of the barrier PL behaves when the power density varies. At low excitation power, the PL intensity increases linearly with the excitation power indicating that exciton recombination tends to dominate. We also attribute to exciton localization the fact that this luminescence band is shifted to lower energies compared to the AlGaN bandgap. However, a quadratic dependence of the PL intensity appears with increasing power density showing that biexciton recombination dominates the low energy side of the barrier PL for high excitation powers. The PL lineshape also becomes more structured enabling us to extract a biexciton binding energy equal to 10 meV, in good agreement with values determined in Ref. [Yamada04].

5.1.2 Photoluminescence excitation (PLE)

The photoluminescence excitation (PLE) spectrum allows, through the variation of the excitation photon energy, to study the higher energy states from which electron-hole pairs relax. The efficiency of photoluminescence excitation depends on the relaxation time and channel from the higher states, to which the sample is excited, to the states from which photoluminescence is emitted and the signal detected. The excitation and the detection photon energies were situated in the spectral range 3.52 - 3.62 eV at 7 K. More details about the PLE experiment can be found in section 3.6. The emission spectrum of the GaN/AlGaN QW sample is shown in Fig. 5.5, where the emission intensity is plotted as a function of excitation energy and detection energy. The spectra of PL and PLE can be extracted from Fig. 5.5a by cutting along the vertical and horizontal axes, respectively. The Rayleigh scattering of the excitation source is observed along the diagonal. The PLE measured at photon energy 3.541 eV is shown in Fig. 5.5b.

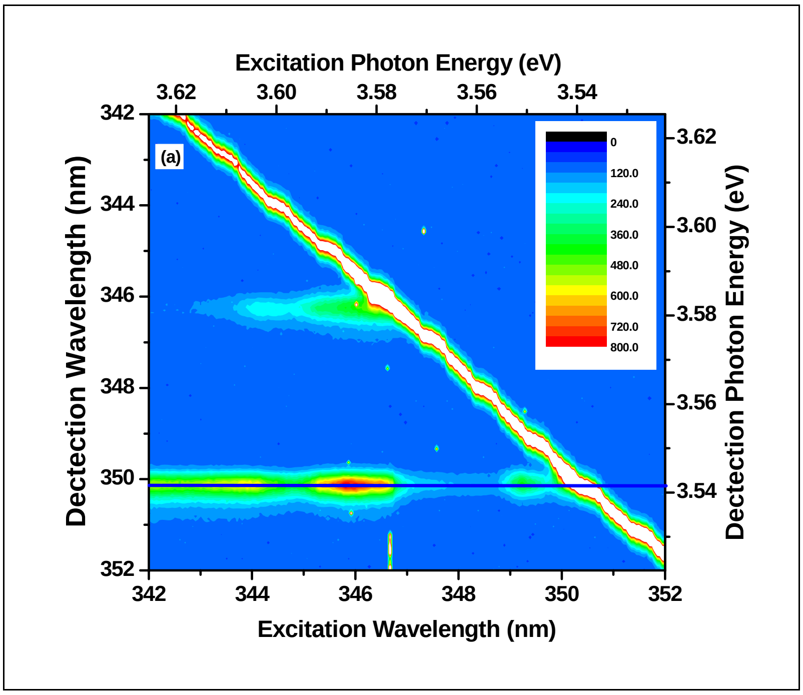

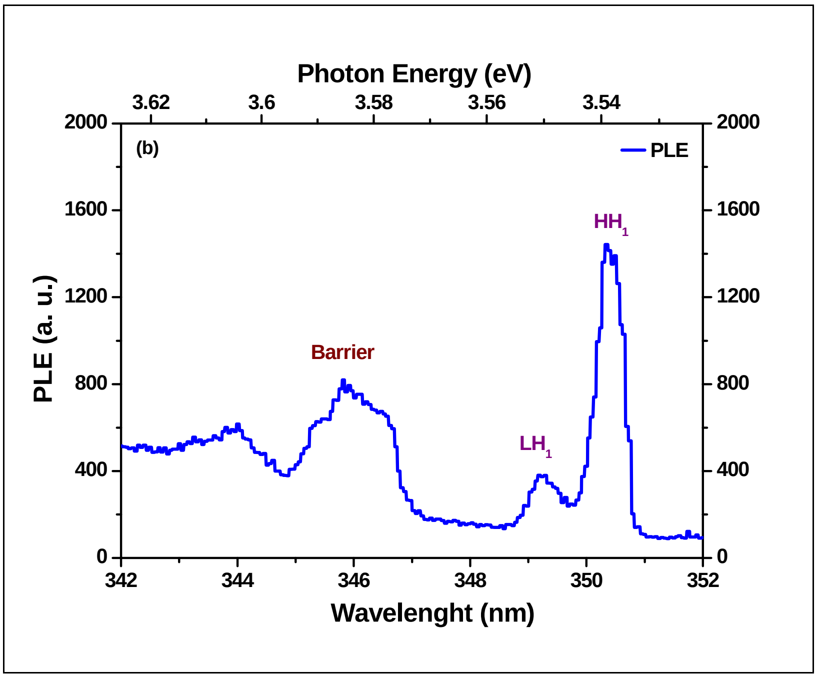

Fig. 5.5. (a) *Emission intensity of GaN/AlGaN QW plotted as a function of excitation photon energy and detection photon energy. The Rayleigh scattering of the excitation source is observed along the diagonal and* (b) *Photoluminescence excitation (PLE) measured at photon energy 3.541 eV at T= 7K.*

The photoluminescence excitation spectrum recorded at the HH$_1$- exciton PL energy exhibits the signatures of the HH$_1$- and LH$_1$- excitons as well as that of the barrier and reveals that no additional confined excitonic states are present in the QW.

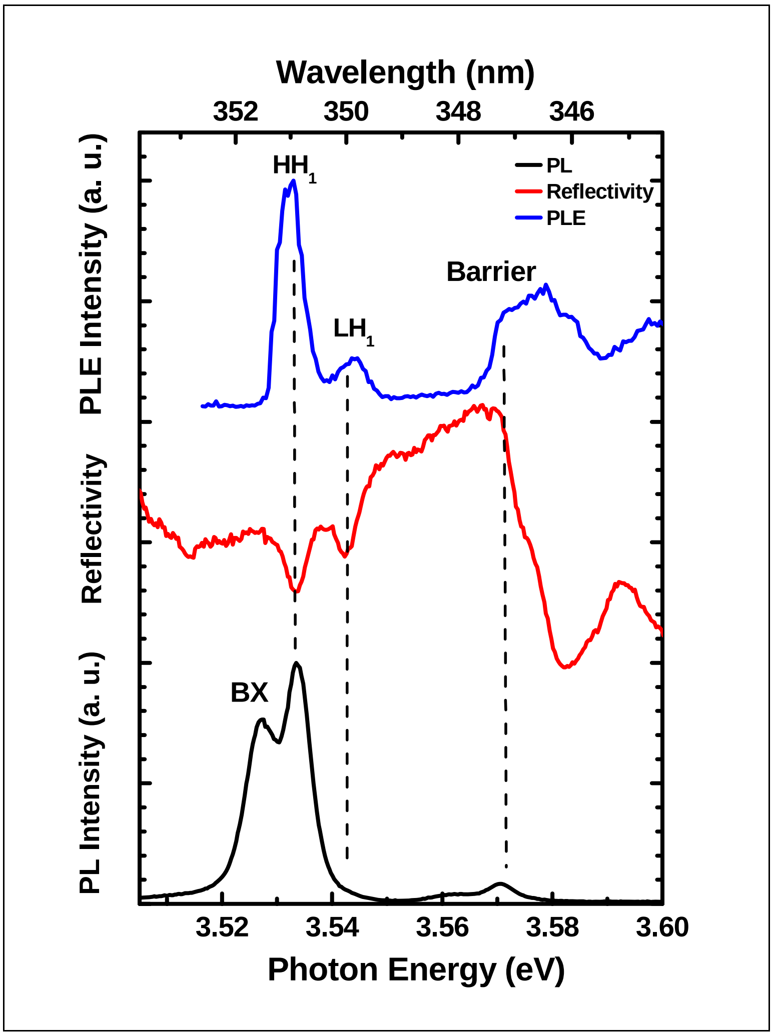

Fig. 5.6. *Photoluminescence, reflectivity and photoluminescence excitation spectra when detecting at 3.541 eV at T= 7K.*

Figure 5.6 summarizes the photoluminescence, the reflectivity and the PLE spectra for the GaN/AlGaN QW. The PLE spectrum corresponds to a detection energy equal to 3.541 eV. No Stokes shift is observed between these three spectra.

5.2 Exciton lifetime.

The exciton lifetimes were measured using the pump-and-probe experimental set-up with linearly polarized beams. Figure 5.7a depicts the $\Delta R/R$ time evolution of HH$_1$,

LH_1 and barrier excitons for excitation with photon energy larger than the barrier bandgap. When the excitons are created in the barrier, the $\Delta R/R$ signals of HH_1 and LH_1 exhibit a risetime characteristic of the population relaxation from the barrier towards the quantum well. It takes about 30 ps before the signal begins to decay.

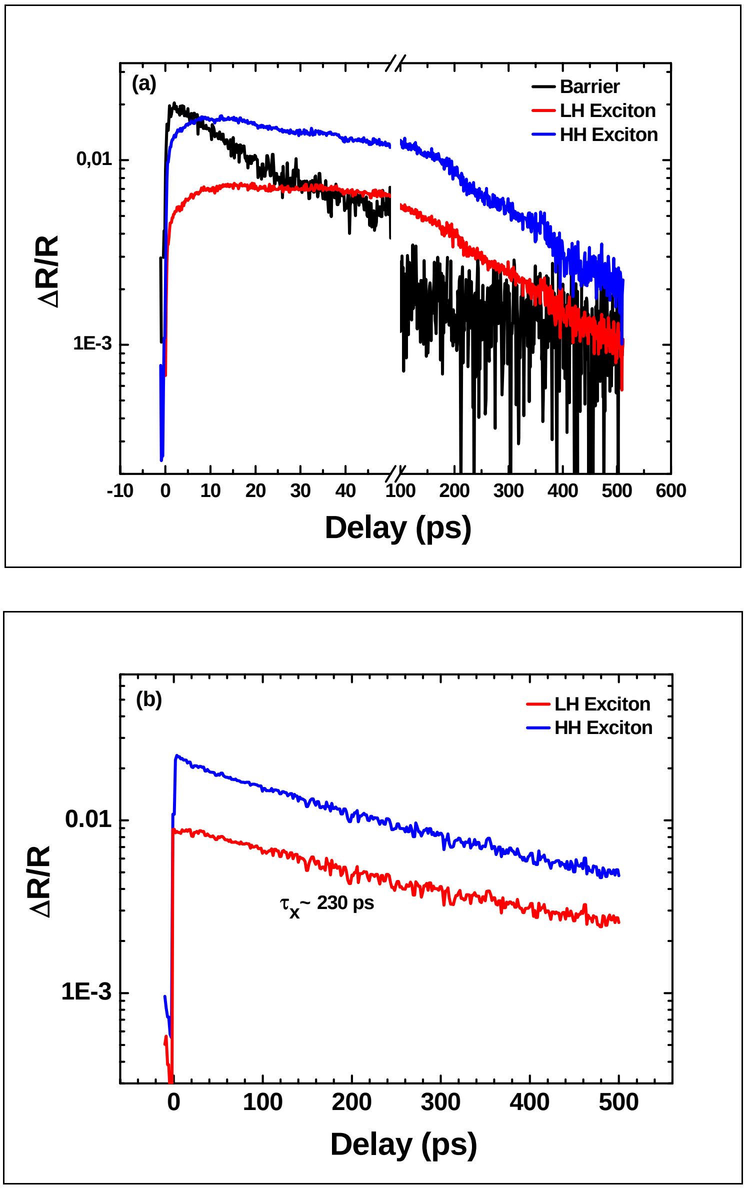

Fig. 5.7. *$\Delta R/R$ as a function of time delay of (a) HH_1, LH_1, and barrier excitons for excitation above the barrier and of (b) HH_1, LH_1 for resonant excitation in the QW at 4K.*

Figure 5.7b shows the time evolution of $\Delta R/R$ signals when resonantly exciting the QW excitons. Whatever the excitation condition (resonant or non-resonant), the decay is monoexponential for both heavy and light hole excitons with a time constant equal to 230 ps which is in good agreement with time-resolved photoluminescence experiments [Stokker09]. This short lifetime indicates that in spite of the quantum confined Stark effect (QCSE), the QW is sufficiently narrow to conserve a strong overlap of the electron and hole envelope functions along the growth axis of the QW and the exciton oscillator strength is large and consequently, the lifetime remains short.

5.3 Introduction to spin dynamics measurements

5.3.1 Principle of the polarized pump-probe experiment

We determine the spin dynamics of a population of photo-created excitons by using the optical selection rules presented in section 2.2.5. We create not only a population of excitons with a definite angular momentum, but we measure also its temporal evolution. We present here a simplified model of three excitonic levels and use it to interpret our results.

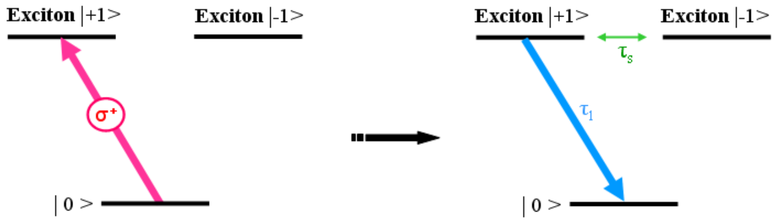

Fig. 5.8. *Three excitonic levels model.*

A circularly polarized pump pulse with polarization σ^+ creates a population of exciton with angular momentum |+1>. This population may relax with time (see Fig. 5.8) and return to the ground state |0> through recombination with a radiative lifetime τ_1. In the simplest case, where the spin of the electron and hole are simultaneously reversed, the spin relaxation is passed from an exciton state |+1> to the state |-1> with a characteristic time of spin τ_S. The existence of a population of angular momentum |+1> or |-1> changes the oscillator strength and hence the differential reflectivity of a probe pulse with polarization σ^+ or σ^-, respectively. Thus, the existence of a population of spin polarized excitons causes different signals for the two polarizations of the probe beam.

Experimentally, the two circular components of the probe pulse can be detected simultaneously as two different spectra, giving information on the population of the two excitonic levels |+1> and |-1>. For each pump-probe delay, the reflectivity of the probe beam is recorded in the presence and then in the absence of the pump pulse. The differential reflectivity spectrum is given by:

$$\frac{\Delta R}{R} = \frac{R_{with\_pump} - R_{without\_pump}}{R_{without\_pump}} \tag{5.1}$$

The signal of *ΔR/R* obtained from the probe beam with polarization σ^+ and σ^- is proportional to the population of states |+1> and |-1> and the configurations of polarization $\sigma^+\sigma^+$ and $\sigma^+\sigma^-$ indicate the polarizations of the pump and probe beams, respectively. The system of coupled differential equations, describing the dynamics of the three excitonic levels, is given as follows:

$$\frac{dn_{|+1>}}{dt} = -n_{+1} \times (\frac{1}{\tau_1} + \frac{1}{\tau_s}) + n_{-1} \times \frac{1}{\tau_s} \tag{5.2}$$

$$\frac{dn_{|-1>}}{dt} = n_{+1} \times \frac{1}{\tau_s} - n_{-1} \times (\frac{1}{\tau_1} + \frac{1}{\tau_s}) \tag{5.3}$$

with $n_{|\pm 1>}$ the population of the excitonic level of spin $|\pm 1>$.

If n_0 is the initial exciton population |+1> created by the pump pulse with σ^+ polarization, the solution of the above system is given by:

$$n_{|+1>} = \frac{n_0}{2} \times e^{-\frac{t}{\tau_1}} \left(1 + e^{-\frac{2t}{\tau_S}} \right), \tag{5.4}$$

and

$$n_{|-1>} = \frac{n_0}{2} \times e^{-\frac{t}{\tau_1}} \left(1 - e^{-\frac{2t}{\tau_S}} \right) \tag{5.5}$$

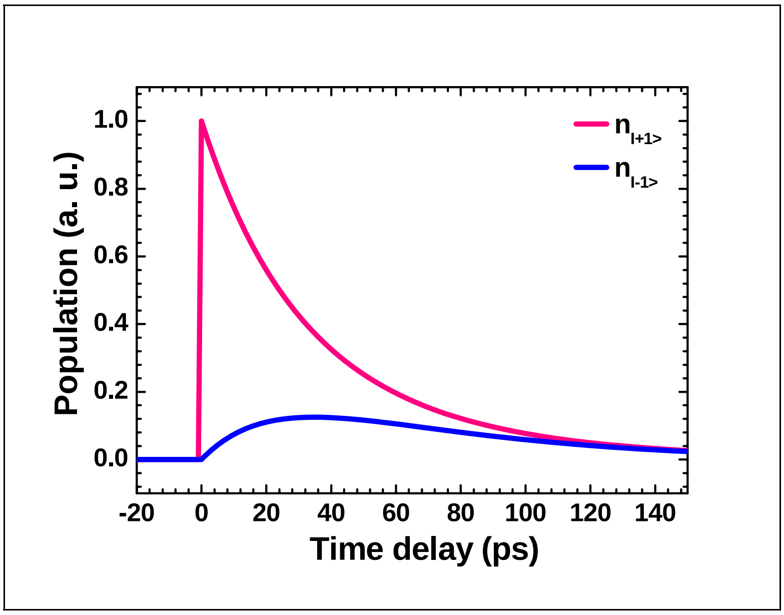

Fig. 5.9. *Temporal evolution of populations* $n_{|+1>}$ *and* $n_{|-1>}$.

Figure 5.9 depicts the population evolution of the two excitonic levels, $n_{|+1>}$ and $n_{|-1>}$, respectively. The population of the |+1> state increases abruptly with the arrival of the pump pulse, of polarization σ^+, and then relaxes by radiative recombination and spin relaxation. The population of the state |-1> is zero at the arrival of the pump pulse since the creation of exciton |-1> is not allowed for polarization σ^+. Then it increases gradually with a characteristic spin relaxation time τ_S since this state is populated by the n_+ excitons which reverse their spin.

5.3.2 Four level exciton model [Vinattieri94, Soleimani05]

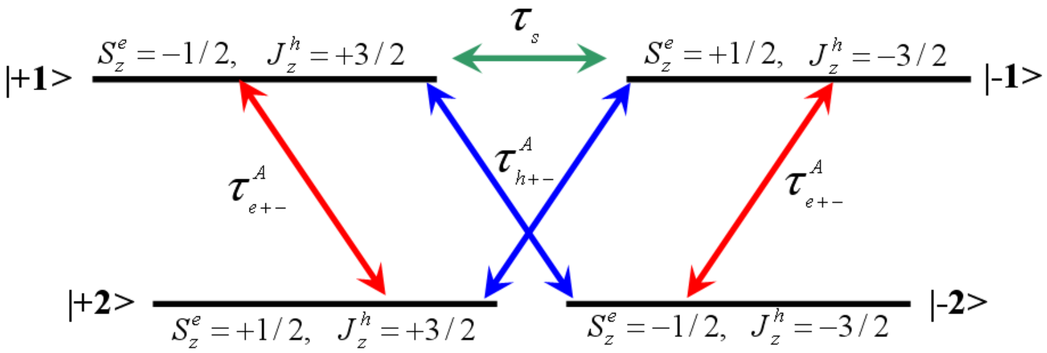
τ_s
|+1>
$S_z^e = -1/2, \quad J_z^h = +3/2$
$S_z^e = +1/2, \quad J_z^h = -3/2$
|-1>
τ_{e+-}^A
τ_{h+-}^A
τ_{e+-}^A
|+2>
$S_z^e = +1/2, \quad J_z^h = +3/2$
$S_z^e = -1/2, \quad J_z^h = -3/2$
|-2>

Fig. 5.10. *Simple four level model for the exciton dynamics.*

We present here a more realistic model for the spin relaxation that takes into account the exciton fine structure in the GaN/AlGaN QW. We consider the heavy holes (HH) valence band with spin ± 3/2 and the conduction band with electrons of spin ± 1/2. From these two levels of holes and electrons, four excitonic levels of pseudo-spin $|\pm 1\rangle = |\mp 1/2, \pm 3/2\rangle$ and $|\pm 2\rangle = |\pm 1/2, \pm 3/2\rangle$ are built. Only $|\pm 1\rangle$ states can be excited optically, and the $|\pm 2\rangle$ states are optically inactive. The exciton states are assumed to be degenerate. Spin relaxation equilibrates the populations of excitons within its four spin states $|\pm 1\rangle$ and $|\pm 2\rangle$. The exciton spin relaxation between the optically-allowed states can occur in a direct, single-step process driven by the electron-hole exchange interaction. In addition, the electron or the hole within an exciton can flip its spin and lead to transition between an optically-allowed and forbidden states.

When the incident photons generate excitons in the optically active |+1> radiative state, exciton spin-relaxation, with rate τ_S, populates |-1> state, i.e. by a simultaneous spin-flip of electron and hole. If only an electron or hole spin flip takes place within the exciton, this populates the dipole-inactive $|\pm 2\rangle$ dark states with transition rates τ^{A}_{e+-} and τ^{A}_{h+-} for electrons and holes, respectively. The different relaxation processes are depicted in Fig. 5.10. The exchange interaction between the excitonic dark states |+2> and |-2> is weak, so the relaxation between these states can be neglected. Moreover, we must also consider the relaxation due to radiative recombination with a time τ^{R} and the non-radiative relaxation to impurities states with characteristic time τ^{NR}. The total relaxation rate of the excitonic population is given by:

$$\frac{1}{\tau_A} = \frac{1}{\tau^R} + \frac{1}{\tau^{NR}} \tag{5.6}$$

5.3.3 The role of biexcitons

Biexcitons can be created by the absorption of two circularly polarized photons according to the optical selection rule as indicated schematically in Fig. 5.11. The creation of the biexcitons starting from a $|+1>_{HH1}$ exciton can be done by the absorption of a σ^- probe photon or by spin-flip followed by the absorption of σ^+ photon.

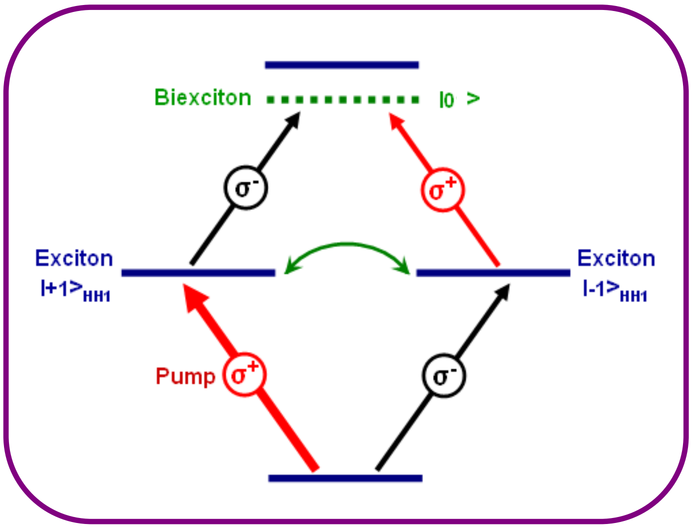

Fig. 5.11. *Biexciton optical selection rules.*

The *ΔR/R* signal for σ^+ (σ^-) probe is proportional to the |-1> (|+1>) population. In other words, the two signals corresponding to the two different probe helicities become equal after a certain time. If the spin-relaxation of the exciton as a whole is the main spin-relaxation process, the time needed for this is precisely the relaxation time of the exciton spin [Soleimani04].

5.4 Optical orientation experiments: excitation with a spectrally broad pump pulse

5.4.1 Differential reflectivity spectra

Differential reflectivity (*ΔR/R*) spectra for the same and opposite circular polarizations of the probe pulses with respect to the circularly polarized pump at time delay Δt = 0.5 ps and at Δt = 7 ps are shown in Fig. 5.12a and b, respectively. The positive time delay indicates that the pump pulse arrives before the probe pulse on the sample.

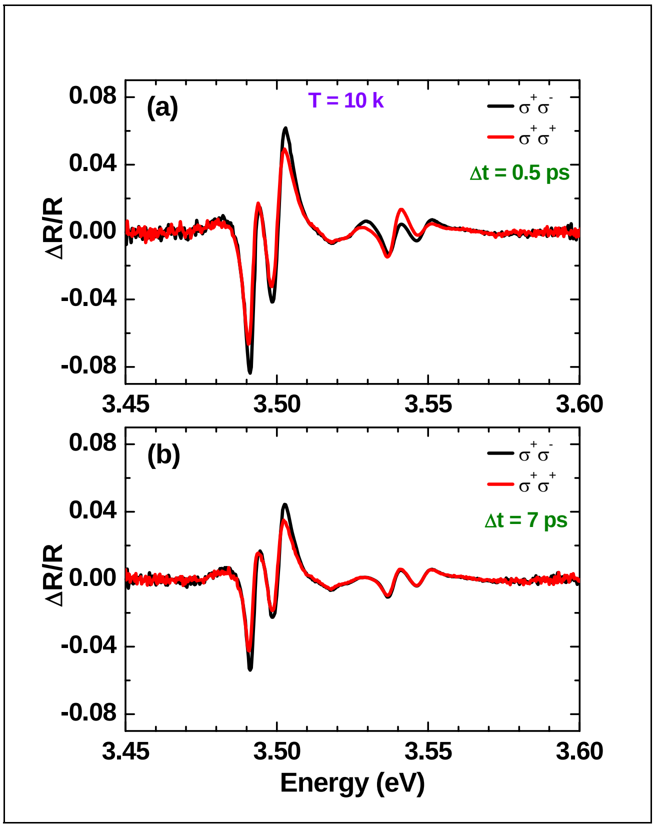

Fig. 5.12. *Differential reflectivity (ΔR/R) spectra covering the GaN buffer layer and the QW regions for co- and counterpolarized configurations of the pump and probe pulses at time delay 0.5 ps (a) and at 7 ps (b).*

The sharp spectral structures at the low energy part of the differential reflectivity spectrum (around 3.50 eV), as shown in Fig. 5.12, are ascribed to the heavy- and light-hole excitons in the GaN buffer layer and the two spectral structures centered at 3.54 eV are characteristics of the HH_1- and LH_1- excitons in the QW.

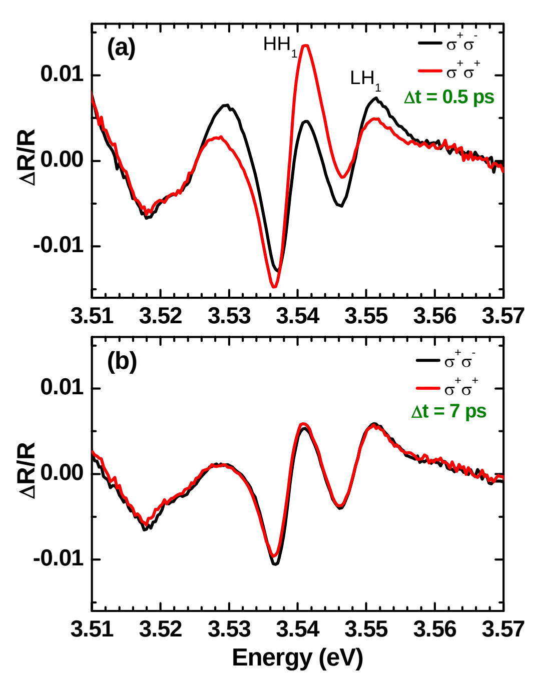

Fig. 5.13. *ΔR/R spectra for co- and counterpolarized configurations of the pump and probe pulses at time delay 0.5 ps* (a) *and at 7 ps* (b) *for* HH_1 *and* LH_1 *in the QW at 10 K.*

According to the optical selection rules of the quantum well shown in Fig. 5.14 for the resonant transitions, the phase space filling is responsible for a non linear signal of which the amplitude depends on the probe polarization as shown in Fig. 5.13a. This indicates that a spin polarized population of excitons is actually photocreated. For longer time delays, the optical orientation disappears and the two spectra become identical for the HH_1- and LH_1- excitons in the QW as depicted in Fig. 5.13b.

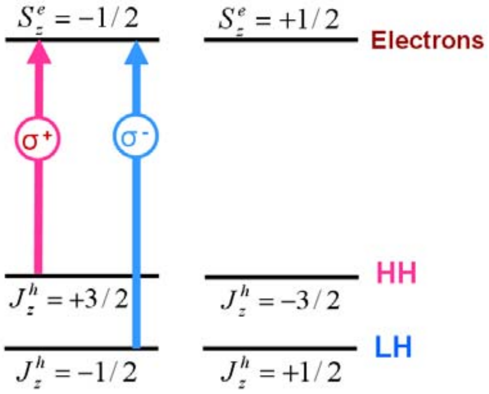

Fig. 5.14. *Optical selection rules.*

Because the HH_1- and LH_1- excitons share the same conduction band, a population of $|+1>_{HH1}$ exciton modifies not only the $|+1>_{HH1}$ oscillator strength but also the $|-1>_{LH1}$ one by the occupation of a spin state S_z^e= -1/2 in the conduction band as shown in Fig. 5.14.

We have also plotted in Fig. 5.15 the difference (*ΔR/R*)($\sigma^+\sigma^+$) - (*ΔR/R*)($\sigma^+\sigma^-$) for different pump-probe delays. This quantity is positive when the *ΔR/R* signal is stronger for the σ^+ polarized probe component than for σ^- polarized one and this can lead us to observe three different transitions: the signals at 3.541 and 3.552 eV originate from the saturation of the HH_1- and LH_1- excitons, respectively. One also notices a signal, ~10 meV below the HH_1 resonance, which is stronger in the counter polarized configuration of the pulses. This is a characteristic of an induced exciton-biexciton transition [Brimont08, Brimont09a]. Note that both the exciton energies and the biexciton binding energy that can be extracted from the data in Fig. 5.15 are different from those determined from luminescence spectroscopy (Fig. 5.6). It is due to the fact that the PL- measurements and the non-linear experiment were not performed on the same region of the sample and also due to the thickness gradient of the QW leading to different energies of the exciton resonances.

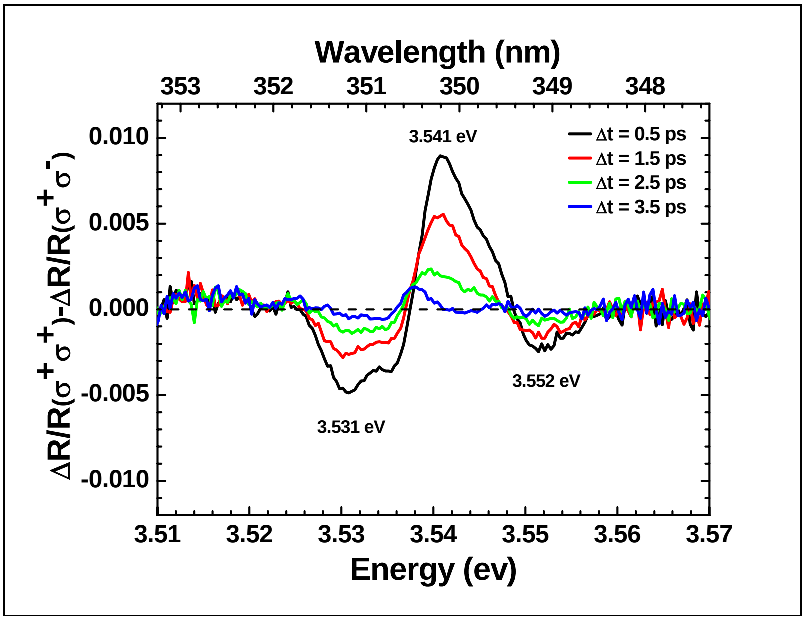

Fig. 5.15. *Difference between the differential reflectivity at positive time delay of 0.5 ps for the two different probe helicities* (*ΔR/R*)($\sigma^+\sigma^+$) - (*ΔR/R*)($\sigma^+\sigma^-$) *at different pump-probe delay at* 10 K.

As expected, the non linear signal is larger at the HH_1-exciton energy when the probe is σ^+ polarized, while it is the opposite for the LH_1 exciton. At short delay times (0.5 ps), the HH_1 signal is broad, showing that the photocreated exciton distribution that participates in the *ΔR/R* changes extends over a wide spectral region (~ 10 meV). For longer time delays, a narrow distribution persists at lower energy on a time > 10 ps. This suggests that the main part of the *ΔR/R* signal originates from free excitons that relax their pseudo-spin within a few ps while a small portion of localized excitons keeps its optical orientation on a longer timescale.

F. Stokker-Cheregi et al. [Stokker08] have observed the biexciton recombination by using time resolved-photoluminescence (TR-PL) experiments and showed that the biexciton emission can be easily distinguished for such GaN/$Al_{0.05}Ga_{0.95}N$ quantum well samples having high optical quality. TR-PL images recorded by a streak camera for different positions on the sample at 10 K are shown in Fig. 5.16 (a-c). They extracted the energy position of the exciton and biexciton recombination bands by fitting the experimental data of TP-PL spectra, related to the images in Fig. 5.16, using two Gaussian line shapes (see Fig. 5.17).

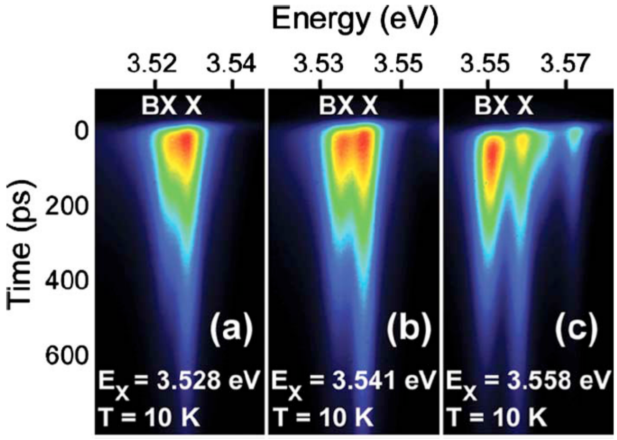

Fig. 5.16(a-c). *TR-PL images for GaN/$Al_{0.05}Ga_{0.95}N$ QW recorded by the streak camera. The energy of the exciton recombination band (E_x) is indicated in each figure:* (a) *E_x=3.528 eV,* (b) *E_x=3.541 eV and* (c) *E_x=3.558 eV.* [Stokker08]

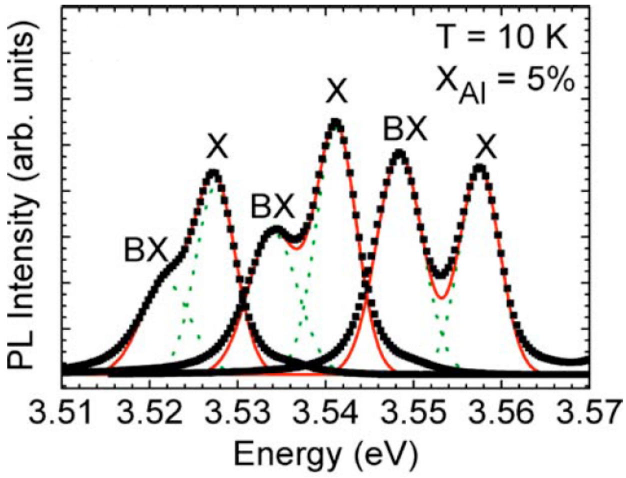

Fig. 5.17. *TR-PL spectra measured at short delays relative to the Fig. 5.13. The squares represent the experimental data and the red full lines are the sum of the fitting Gaussian line shapes (dotted lines).* [Stokker08]

The energy difference between the Gaussian fits of the exciton (X) and biexciton (BX) bands was taken as the biexciton binding energy. The highest measured value of the biexciton binding energy is 9.1 meV for a GaN/$Al_{0.05}Ga_{0.95}N$ QW.

5.4.2 Model for the amplitude of the ΔR/R signals

Because HH_1 and LH_1 excitons share the same conduction band, a population of $|+1>_{HH1}$ excitons modifies also the oscillator strength of the $|-1>_{LH1}$ excitons. Quantitatively, the *ΔR/R* signal, as a function of the electron and hole occupation numbers, f_e and f_h, yields [Soleimani05]:

$$\left(\frac{\Delta R}{R}\right)(\sigma^{\pm}) \propto F_{OSC}(HH_1)\left[f_e\left(\mp\frac{1}{2}\right)+f_h\left(\pm\frac{3}{2}\right)\right] \tag{5.7}$$

$$\left(\frac{\Delta R}{R}\right)(\sigma^{\pm}) \propto F_{OSC}(LH_1)\left[f_e\left(\mp\frac{1}{2}\right)+f_h\left(\mp\frac{1}{2}\right)\right] \tag{5.8}$$

F_{OSC} denotes the exciton oscillator strength. We introduce $n|\pm1>_{HH1}$ and $n|\pm1>_{LH1}$ the number of heavy- and light- hole excitons respectively. The parameter ±1 refers to the total angular momentum. $|\pm2>_{HH1}$ and $|\pm0>_{LH1}$ are dark excitons. The signals thus become:

$$\left(\frac{\Delta R}{R}\right)_{HH_1}(\sigma^{\mp}) \propto F_{OSC}^{HH_1}\times\left(2n|\mp1\rangle_{HH_1}+n|\pm1\rangle_{LH_1}+n|+2\rangle_{HH_1}+n|-2\rangle_{HH_1}+n|0\rangle_{LH_1}\right) \tag{5.9}$$

and

$$\left(\frac{\Delta R}{R}\right)_{LH_1}(\sigma^{\mp}) \propto F_{OSC}^{LH_1}\times\left(n|\pm1\rangle_{HH_1}+n|\mp2\rangle_{HH_1}+2n|\mp1\rangle_{LH_1}+n|+0\rangle_{LH_1}+n|-0\rangle_{LH_1}\right) \tag{5.10}$$

The LH_1- and HH_1- excitons are populated by the pump pulse and, at zero delay time, before any spin-flip occurs, no dark excitons are present. The signal reads:

$$\left(\frac{\Delta R}{R}\right)_{HH_1}(\sigma^{\mp}) \propto F_{OSC}^{HH_1}\times\left(2n|\mp1\rangle_{HH_1}+n|\pm1\rangle_{LH_1}\right) \tag{5.11}$$

$$\left(\frac{\Delta R}{R}\right)_{LH_1}(\sigma^{\mp}) \propto F_{OSC}^{LH_1}\times\left(2n|\mp1\rangle_{LH_1}+n|\pm1\rangle_{HH_1}\right) \tag{5.12}$$

Using these expressions, it is easy to see that, even in the absence of LH_1-excitons, a signal is expected at the LH_1- exciton energy for a σ^- polarized probe. The amplitude is equal to the amplitude of the HH_1 signal multiplied by the factor $F_{OSC}(LH_1) / 2F_{OSC}(HH_1)$.

For a σ^+ pump excitation, at zero delay time, the populations of |-1> excitons are zero: $n|-1>_{LH1} = n|-1>_{HH1} = 0$. It is straightforward that, for one type of exciton, the ratio $(\Delta R/R)(\sigma^+) \div (\Delta R/R)(\sigma^-)$ simply depends on $n|+1>_{HH1}$ and $n|+1>_{LH1}$ and this can be rewritten as

$$\left(\frac{\Delta R}{R}\right)_{HH_1}^{\sigma^+} \Bigg/ \left(\frac{\Delta R}{R}\right)_{HH_1}^{\sigma-} \propto 2\frac{n|+1\rangle_{HH_1}}{n|+1\rangle_{LH_1}} \tag{5.13}$$

for HH_1- exciton while for the LH_1- exciton as

$$\left(\frac{\Delta R}{R}\right)_{LH_1}^{\sigma^+} \Bigg/ \left(\frac{\Delta R}{R}\right)_{LH_1}^{\sigma-} \propto 2\frac{n|+1\rangle_{LH_1}}{n|+1\rangle_{HH_1}} \tag{5.14}$$

We deduce from the experimental data that $n|+1>_{HH1} \approx 3.5 \times n|+1>_{LH1}$. Then we conclude that the ratio $F_{OSC}(LH_1) / F_{OSC}(HH_1)$ is close to 1 which would correspond to nearly equal radiative lifetimes of HH_1 and LH_1 excitons.

5.4.3 Dynamics of the circular degree of polarization and spin relaxation

The spectrally-integrated *ΔR/R* decays for the three transitions are displayed in Fig. 5.18. The circular degree of polarization (P_c) of the signals is also plotted. P_c is calculated from polarization changes in the right and left circularly polarized reflected probes as

$$P_c = \frac{\frac{\Delta R}{R}(\sigma^+) - \frac{\Delta R}{R}(\sigma^-)}{\frac{\Delta R}{R}(\sigma^+) + \frac{\Delta R}{R}(\sigma^-)} \tag{5.15}$$

As defined in eq. 5.15, P_c is the difference between the two signals normalized by their sum and it directly reflects the spin polarization of the exciton population. We investigate the induced transition at the biexcitonic resonance. It reaches a maximum in $\sigma^+ \sigma^-$

configuration after a rise time of ~ 0.8 ps. For a $\sigma^+ \sigma^+$ polarization sequence, it progressively increases when the $\sigma^+ \sigma^-$ *ΔR/R* decreases. The two signals are equal after about 4 ps.

According to the optical selection rules, there are two possible scenarios for the creation of a biexciton starting from a $|+1>_{LH1}$ exciton. It can be done by the absorption of a σ^- probe photon or by a spin-flip followed by the absorption of a σ^+ photon. Consequently, the *ΔR/R* signal for σ^+ (σ^-) probe is proportional to the |-1> (|+1>) population.

The time decays evidence that the loss of the $|+1>_{HH1}$ excitonic population directly feeds the $|-1>_{HH1}$ pseudo-spin state via a simultaneous spin-flip of electron and hole. In other words, the time needed to equal the two signals, corresponding to the two different probe helicities gives directly the relaxation time τ_s of the exciton spin [Soleimani04] as discussed in section 5.3.1. Very similar are the decays related to the HH_1 exciton. Here again, the signal, when pump and probe are co-polarized, reaches its highest value after a rise time on the picosecond range. When it is achieved the counter-polarized signal is three times smaller than the co-polarized. Then, as fast as the exciton spin relaxes, the two signals evolve to become equal. The degree of polarization decays exponentially with a time constant close to 2 ps which is quite comparable to what was measured in GaN epilayers.

The optical orientation decay can be due the spin-flip of the exciton as a whole, characterized by a time τ_s, or to the spin relaxation of the individual carriers, characterized by the times τ_e and τ_h. Here, the similarities between the dynamics at the HH_1 energy and at the biexciton energy suggest that the spin relaxation occurs mainly because of the spin relaxation of the exciton as a whole. In this case, the circular degree of polarization simply presents an exponential decay characterized by the time constant τ_s / 2. This is different from the previous results on GaN epilayers [Brimont08, Brimont09a] in which the spin relaxation of the individual carriers was more efficient than the exciton spin-flip.

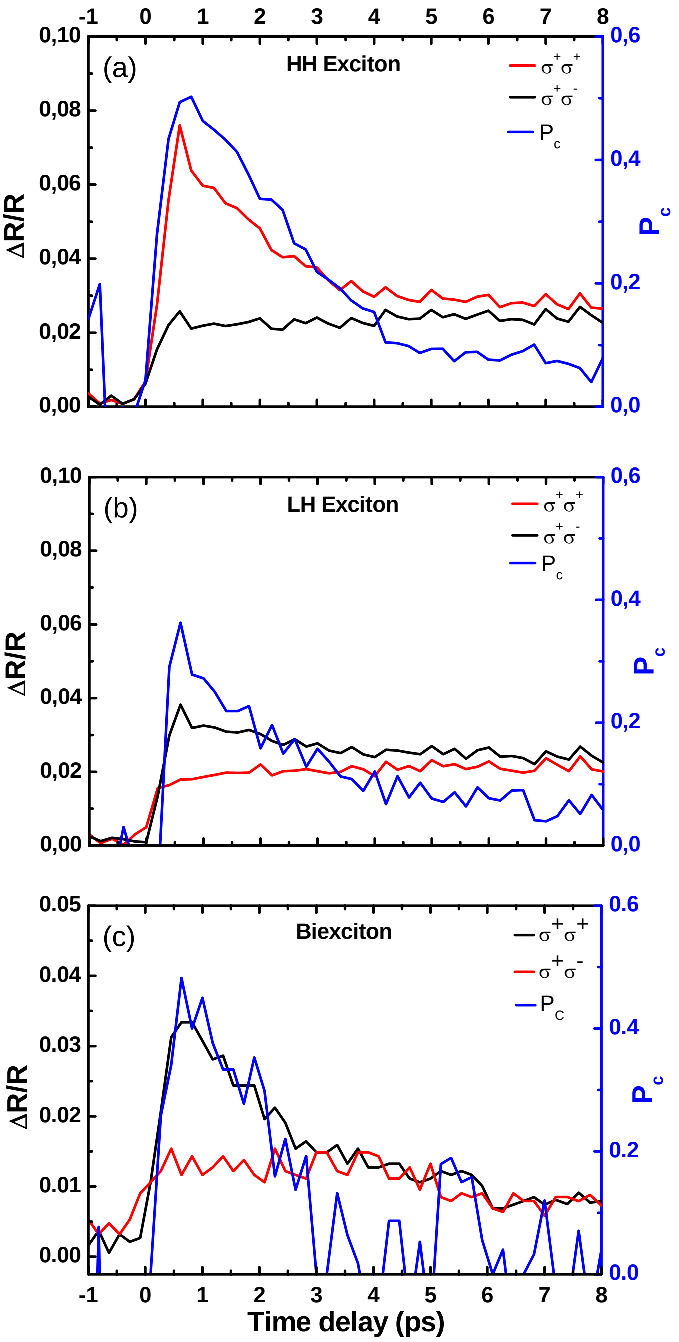

Fig. 5.18. *Spectrally integrated ΔR/R decays for the three transitions:* HH_1*,* LH_1 *and BX. The circular degree of polarization* (P_c) *is also plotted.*

Another difference is the initial value of the degree of polarization, close to 60 %, which is larger than that in bulk material (~ 50 % in the case of the best sample of Ref. [Brimont09a]) and that is, to our knowledge, the highest value measured in nitride compounds. At the LH_1- exciton energy, the time evolution of the pump-probe signals is comparable to the one of HH_1- excitons. However, the maximum amplitudes are smaller as already discussed above.

5.5 Optical orientation using selective excitonic excitation

To be able to excite selectively the excitonic transition, the pump pulses are spectrally filtered through a Fabry-Perot cavity. The Fabry-Perot transmittance is described by the Airy function, which is the periodic succession of peaks whose spectral profile is quasi-Lorentzian. This corresponds, in the time domain, to the sum of multiple pulse reflections. The Fabry-Perot cavity is tuned by minimizing the photoluminescence of the light-hole (LH_1) excitons.

The circularly polarized pump pulses selectively excite the heavy-hole (HH_1) excitonic transition with total angular momentum $|+1>_{HH1}$ and the differential reflectivity ($\Delta R/R$) spectra at a positive time delay of 0.4 ps are measured for the two different probe helicities. The phase space filling at the heavy-hole exciton energy is responsible for a non linear signal, the amplitude of which depends on the probe polarization, as expected from the optical selection rules. This indicates that a spin polarized population of excitons is actually photocreated. For longer time delays, the optical orientation disappears and the two spectra become identical and we do not observe any induced signal related to the biexciton formation.

As shown in Fig. 5.19, the $\Delta R/R$ ratio decays at the heavy-hole (HH_1) exciton energy for the two reflected components of the probe. As fast as the exciton spin relaxes, the two signals evolve to become equal after few picoseconds.

The amount of circular degree of polarization depends on the difference between $|+1>_{HH1}$ and $|-1>_{HH1}$ populations, as well as on the other exciton populations (such as $|\pm2>_{HH1}$ dark states). This quantity decays exponentially with a time constant ~ 3 ps. However, the initial value of the degree of polarization (P_c) is close to 80%, as indicated in Fig. 5.20, which is much higher than that is in bulk material [Brimont09]. This high percentage of degree of polarization can be deduced using eq. 5.11 and eq. 5.15 at zero time delay which gives high value for selective excitonic excitation of the HH_1

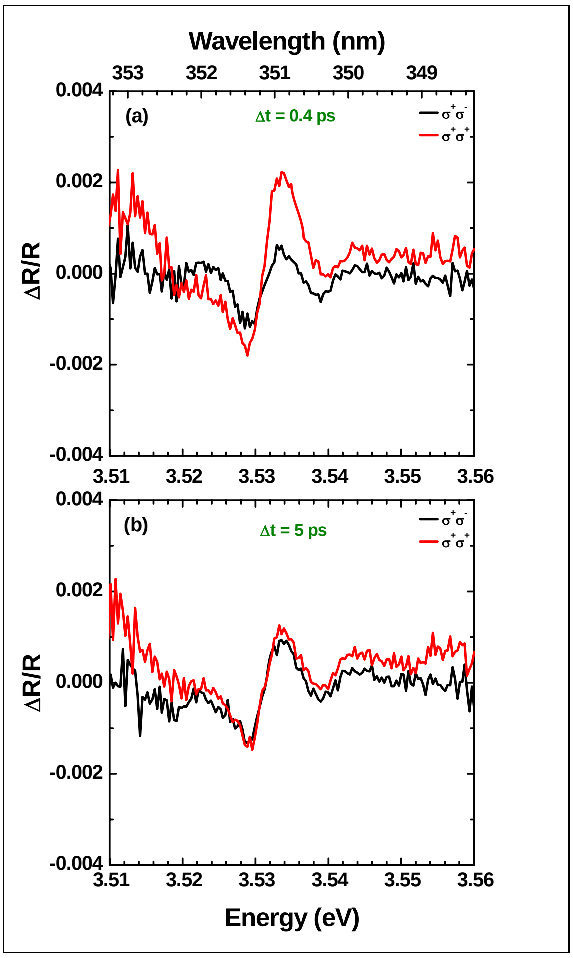

Fig. 5.19. *Differential reflectivity spectra for selective excitation of* HH_1 *in the QW for co- and counterpolarized configurations at time delay (a) 0.4 ps and at (b) 5 ps.*

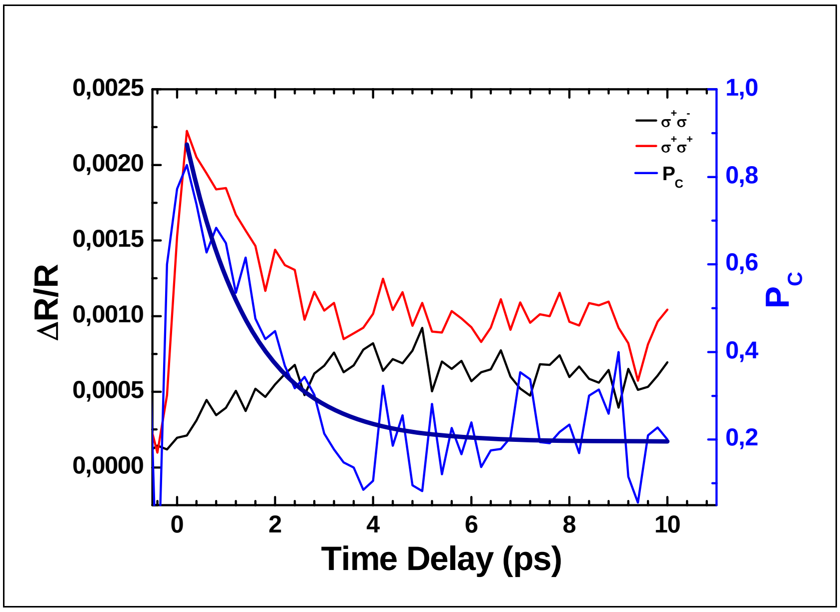

Fig. 5.20. *ΔR/R decays and circular degree of polarization* (P_c) *for the selective excitation of* HH_1 *in the QW.*

5.6 Power and temperature dependences

In order to have more information on the relaxation process, we have performed experiments for different excitation powers and for different sample temperatures. These complementary studies are limited to the HH_1- exciton case, the signal to noise ratio related to the other transitions being severely reduced when decreasing the incident power or increasing the sample temperature. In these measurements the pump pulse is spectrally broad.

5.6.1 Power dependence

Figure 5.21 shows the Differential reflectivity spectra (*ΔR/R*) at a fixed time delay (0.5 ps) for different pump intensity from P_0 to $P_0/16$ and P_0 corresponds to an average power which equals to 600 μW. We can see that the differential reflectivity is decreasing when decreasing the average power of the excitation pump pulses.

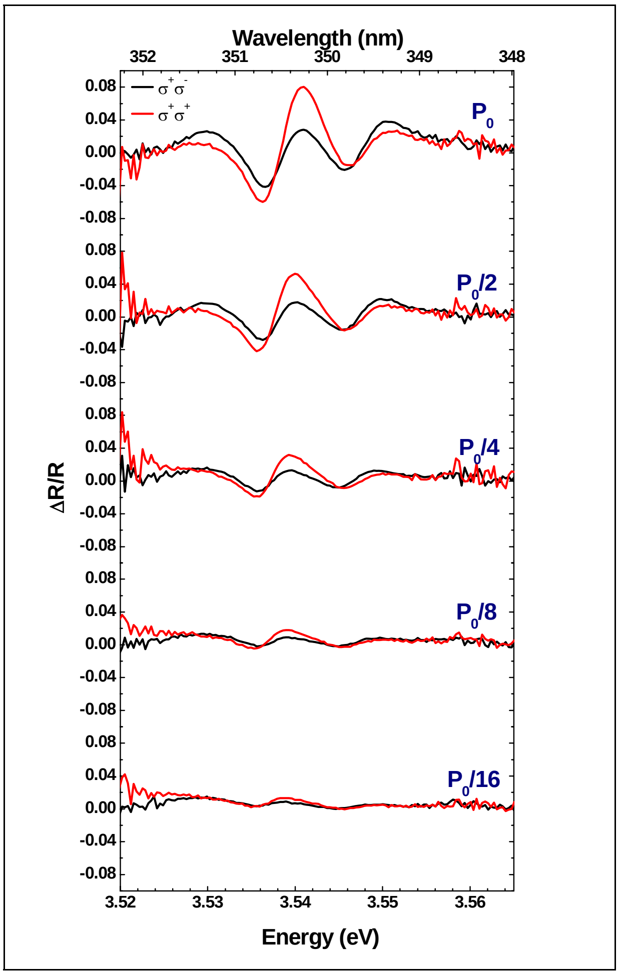

Fig. 5.21. *Differential reflectivity spectra (ΔR/R) for different pump intensity from P_0 to $P_0/16$, P_0 corresponds to an average power equal to 600 μW.*

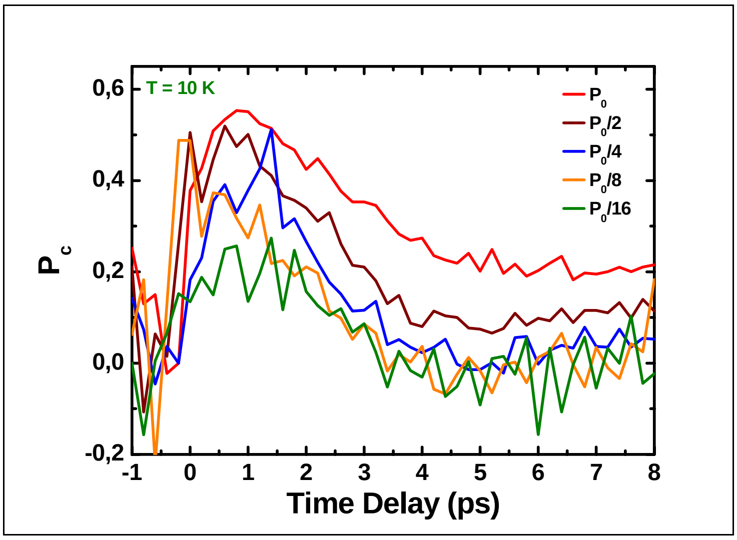

Fig. 5.22 *Time evolution of the circular degree of polarization, at the HH_1 exciton energy, for different pump intensities from P_0 to $P_0/16$.*

The time evolution of the circular degree of polarization (P_c), given by equation 5.15, for different pump intensities from P_0 to $P_0/16$ is displayed in Fig. 5.22. No change in the dynamics is observed for the circular degree of polarization as a function of exciton density, but only the initial value of the degree of polarization is affected showing that the exciton-exciton collisions are not responsible for the spin relaxation.

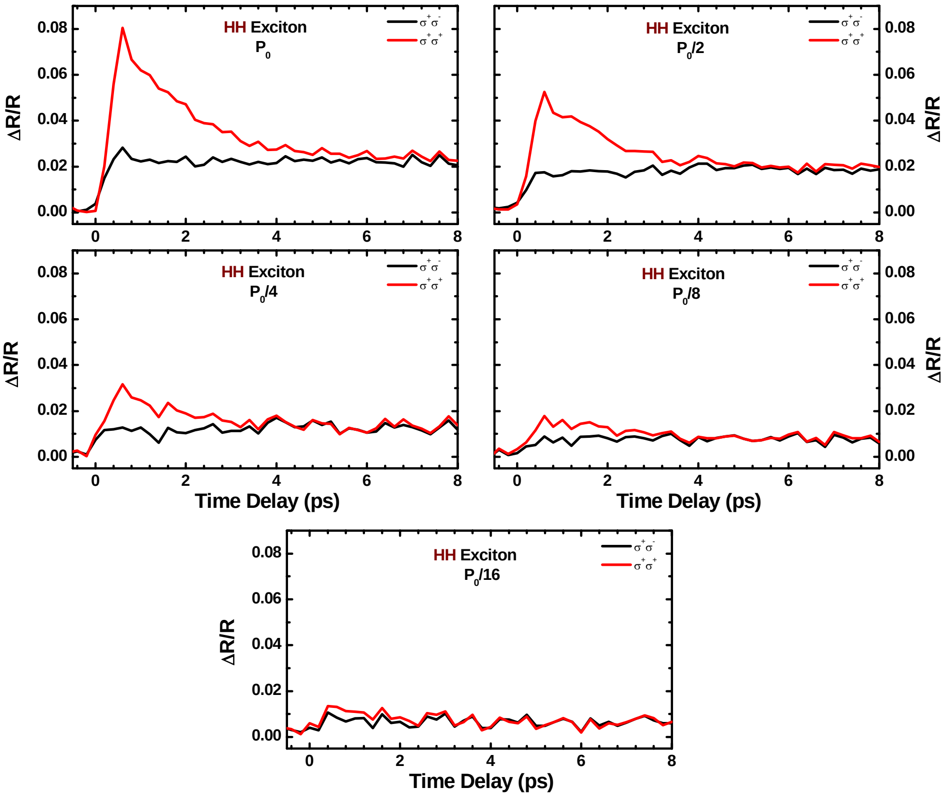

Fig. 5.23. *ΔR/R decays for the heavy hole exciton (HH_1) at different pump intensities.*

Figures 5.23 and 5.24 display the differential reflectivity decays for the heavy-hole exciton (HH_1) and for the light-hole exciton (LH_1) at different pump intensities from P_0 to $P_0/16$, respectively. The decays related to the HH_1- and LH_1- exciton are very similar. The signal, when pump and probe are co-polarized, reaches its highest value after a rise time on the picosecond range and become equal after a few ps.

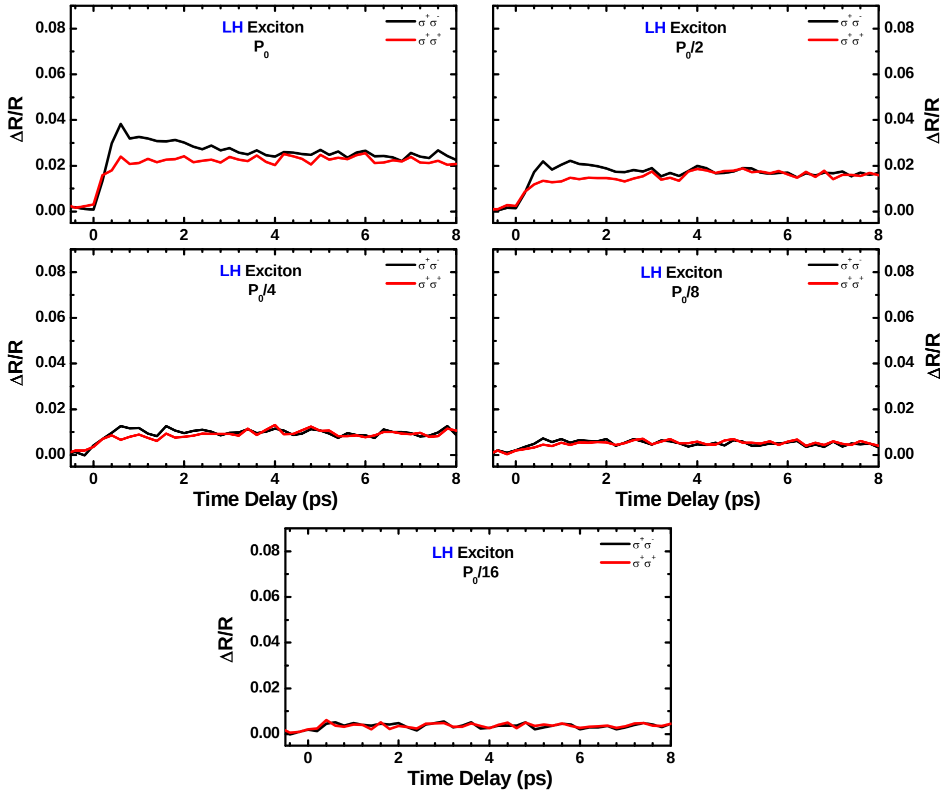

Fig. 5.24. *$\Delta R/R$ decays for the light hole exciton (LH_1) at different pump intensities.*

5.6.2 Temperature Effect

We present here a study based on the temperature effect on the differential reflectivity and circular degree of polarization for GaN/AlGaN QW. We selected measurements in the pump-probe experiments with the best signal to noise ratio. The experiment for measuring $\Delta R/R$ was carried out at different temperatures ranging from 10 K and 120 K as shown in Fig. 5.25. Above this temperature the signal to noise ratio becomes too weak to extract reliable quantities since the confinement energy varies across the sample surface because of the gradient of the well width.

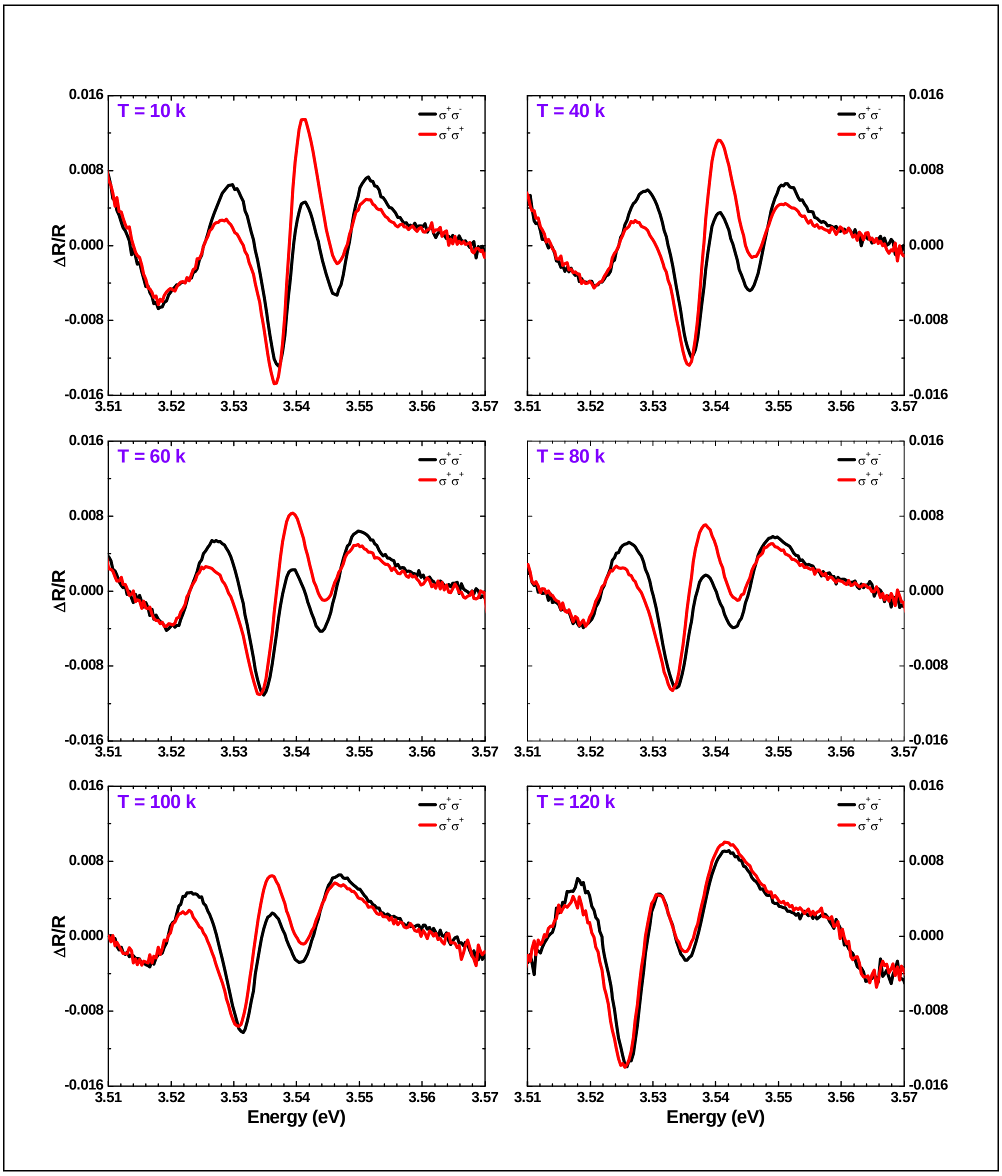

Fig. 5.25. *Differential reflectivity spectra at different temperatures for co- and counterpolarized configurations of the pump and probe pulses at a positive time delay of 0.5 ps.*

The spin relaxation is determined from the circular degree of polarization (P_c) of the signal. The temporal behaviour of the P_c at different temperatures is depicted in Fig. 5.26, which shows that there is only a small temperature dependence of the initial values of P_c that varies from around 0.45 to 0.6. During the experiment it was difficult to get high stabilization and to keep the same sample position with changing the temperature.

Figure 5.27 displays the decay time of the degree of polarization as a function of temperature for the HH_1- exciton. The decays present a strong dependence on sample temperature. The spin lifetime remains slightly constant up to ~ 80 K and then decreases.

Above 100 K the relaxation was shorter than the experimental time resolution. The initial value of the degree of polarization remains constant.

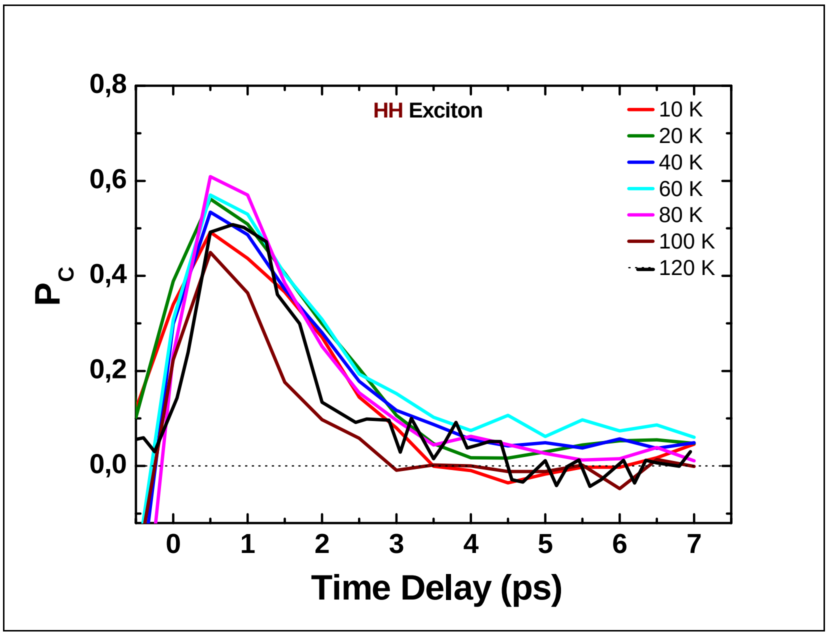

Fig. 5.26. *Circular degree of polarization (P_c) spectra at different temperatures for HH_1.*

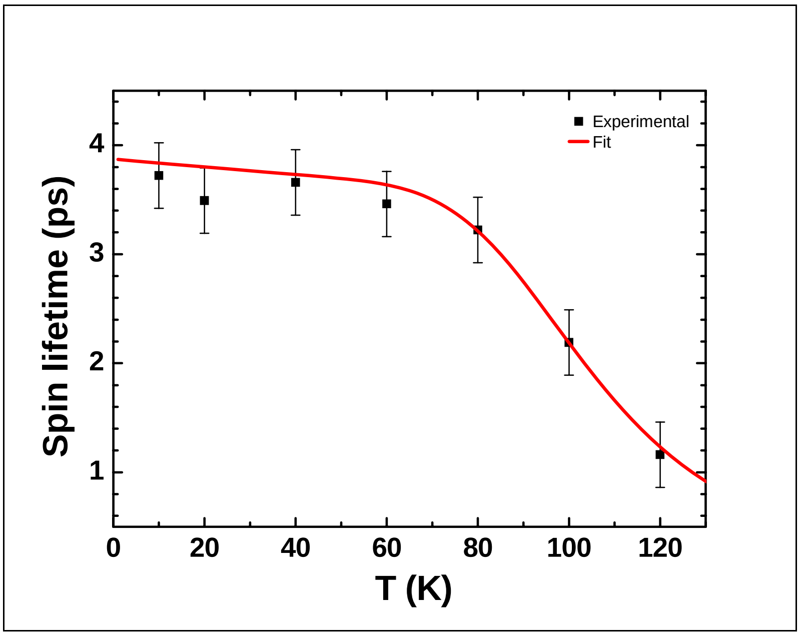

Fig. 5.27. *Time decay of the degree of polarization, at the HH_1 exciton energy, as a function of temperature.*

5.7 Discussion

We have shown above that the ΔR/R signals mainly originate from free HH_1- and LH_1- excitons and that the spin relaxation implies a simultaneous flip of both electron- and hole- spins that connect the two optically active states |+1> and |-1> (we will recall in the following how the electron-hole exchange interaction is responsible for the spin-flip of an exciton that propagates in a QW). This process was evoked by several groups of authors to interpret spin-dynamics experiments on excitons in GaAs-based QWs [Tackeushi90]. However, as this mechanism appears to be negligible in GaN epilayers [Brimont08, Brimont09a], we deduce that exchange interaction is considerably larger in the present QW than that in the bulk case.

Theoretical work has demonstrated that quantum confinement [Chen88, Andreani90], can actually enhance exchange interaction provided that the wave vector of the exciton center of mass $\boldsymbol{K}$ fulfills the condition $\boldsymbol{K}L \gg 1$, where L is the well width [Andreani90]. Taking into account that the initial, out of equilibrium, population of excitons presents a momentum distribution centered on $\boldsymbol{K} = 0$, we assume that elastic exciton-exciton scattering is responsible for the thermalization of excitons to finite $\boldsymbol{K}$ states. The thermalization process takes place during the risetime of the nonlinear signal and conserves both energy and total momentum of the two quasi-particles and their spin orientation. The energy excess that is equally distributed between excitons is precisely the energy difference between HH_1 and LH_1 bands multiplied by the total number of excitons. The final $\boldsymbol{K}$ distribution and, therefore, the exchange term in the exciton Hamiltonian that is responsible for the coupling between excitons with opposite pseudo-spins (see next paragraph) are independent of the exciton density. This is why the experimental dynamics of the ΔR/R circular degree of polarization is independent of the excitation intensity.

Theoretically, the exchange spin-flip mechanism in QWs was worked out by Maialle et al. [Maialle93]. At a finite center of mass wavevector, the spin exchange interaction couples the optically active HH_1- excitons (|+1> and |-1>) [Maialle93]. The coupling terms in the Hamiltonian can be looked upon as an effective magnetic field around which the exciton pseudo-spin precesses with a frequency Ω. If the center of mass wave vector $\mathbf{k}$ is kept fixed, the direction of the effective magnetic-field is constant and the precession leads to a spin relaxation. Comparing Ω with the dephasing time $\grave{T}_2$, when the condition $\Omega\ \grave{T}_2 << 1$ is fulfilled, the relaxation is hindered by motional narrowing as in the D'yakonov-Perel mechanism and $\tau_s \sim (\Omega^2\ \grave{T}_2)^{-1}$ with $\tau_s > \grave{T}_2$.

On the contrary, when $\Omega\ \grave{T}_2 > 1$ then $\tau_s \sim 2\grave{T}_2$. We assume the $\grave{T}_2$ time in GaN/AlGaN QWs to be close to the bulk value. Thus, a comparison between the measured value of the spin lifetime τ_s in the present QW and the experimental dephasing times in GaN epilayers, [Fischer97, Zimmermann97, Pau97, Pau98, Aoki99, Haag99] suggests that τ_s behaves as $2\grave{T}_2$(To the best of our knowledge, no data concerning the dephasing time of excitons in GaN/AlGaN QWs are available. Nevertheless, in GaAs, it was shown that exciton dephasing times in bulk material as well as in QWs are in the picosecond range for a low excitation density at liquid helium temperature [Shah96]). Moreover, when increasing the temperature, a dramatic enhancement of the dephasing process is expected through interaction with acoustic and optical phonons [Shah96]. It would lead to an increase of τ_s if the relaxation took place in the motional narrowing regime. This is not as what is observed in temperature dependent experiments. We therefore conclude that the spin relaxation of excitons occurs in a regime where $\Omega\ \grave{T}_2 > 1$ as discussed above and that τ_s is proportional to $\grave{T}_2$. Understanding spin relaxation implies determining which mechanisms are responsible for the momentum relaxation. This is the purpose of the next paragraphs.

At low temperatures, typically between 10 K and 50 K, the excitons are free to propagate in the QW plane. Even if fluctuations of the confining potential in the *xy*- plane are small, they can scatter the exciton center of mass and consequently, dephase them. These fluctuations can be due to the well interface roughness or to concentration fluctuations of the barrier alloy. In particular, it has been shown that the interface roughness root mean square (rms) is around 1 nm on a $5\times5\ \mu m^2$ area [Feltin07]. The threading dislocations also play a role in exciton scattering because of the coulomb potential and the strain field that they produce [Jena04]. The experimental manifestation of these scattering processes is the broadening of the main optical transition which is ~ 5 meV for the HH_1- exciton at 7 K.

At high temperatures, a thermally activated process is responsible for the shortening of the dephasing time and therefore shortening of the spin lifetime. In order to extract some quantitative parameters, we fit the temperature evolution of τ_s by the expression:

$$\tau_s = 2\,\grave{T}_2 = 2\hbar\,[\Gamma_0 + a \times \mathbf{T} + b \times \exp(\,-\,\Delta E / k_B\,\mathbf{T}\,)]^{-1}$$

where Γ_0 is the homogeneous broadening at 0 K, a stands for the interaction between excitons and acoustic phonons, and $b \times \exp(-\Delta E/k_B T)$ is the broadening due to a thermally activated process with an activation energy ΔE. Longitudinal optical phonons are not taken into account because of the high LO- phonon energy in III-nitrides (~ 92 meV in bulk GaN).

The best agreement between the fit and the experimental data is obtained for $\Gamma_0 = 0.34$ meV, $a = 0.32$ µeV/K, $b = 167.7$ meV and $\Delta E = 56.5$ meV. So, when temperature is increased, the main dephasing mechanism is an escape process of excitons implying a localization energy $\Delta E = 56.5$ meV. It appears that the situation is very similar to what was obtained by Brown *et al.* in InGaN/GaN QWs [Brown08]. These authors showed that increasing the temperature enhances the exciton dephasing by interaction through acoustic phonons and by exciton delocalization from potential fluctuations due to alloy disorder.

However, even if the intrinsic parameters (exchange interaction, phonon energies) responsible for spin relaxation are close to each other when comparing GaN and InGaN, the two systems are fundamentally different. Indeed, the present GaN quantum well is made of a binary compound and in-plane fluctuations are expected to be much smaller in GaN wells than in InGaN wells leading to small in-plane localization energies. They lie within a few meV as confirmed by the small Stokes shift between PL and PLE (3 meV) [Stokker08].

Consequently, if the thermally activated dephasing process in the present GaN/AlGaN QW sample was also caused by in-plane delocalization of excitons, it would imply a characteristic energy in the meV range which is not the case. Nevertheless, as $\Delta E = 56.5$ meV is very close to the difference between the energy of excitonic transitions in the QW and in the AlGaN barrier (as measured in PL and PLE experiments), we propose the following mechanism to explain the shortening of the spin lifetime at high temperature: when the temperature is increased there is a non-zero probability for QW excitons to escape to the barrier and relax back into the QW. In the meantime, excitons are scattered in the AlGaN barrier where they relax their momentum and, therefore, their spin. The spin relaxation is then driven by delocalization of excitons from the QW toward the AlGaN barrier.

5.8 Conclusion (Part II)

We have performed linear spectroscopic measurements of a GaN/AlGaN quantum well (QW). Photoluminescence (PL) spectra show three different regions: the GaN buffer layer, the quantum well centered at 3.54 eV, and the AlGaN barrier at a higher photon energy. The PL intensity of the exciton increases linearly in the beginning and tends to saturate with increasing the excitation power while the biexciton density does not vary as the square of the exciton density but rather varies with the order of 1.56. This can be explained by considering that the exciton and the biexciton have short recombination times compared to the thermalization time. The biexciton binding energy (ΔE) has the value of ~ 8 meV.

We have shown that the spin-relaxation of the exciton as a whole is the main process responsible process for the spin relaxation in the QW. This is different from previous work on GaN epilayers where this mechanism was negligible. The enhancement of this process is due to quantum confinement that increases the exciton exchange interaction when compared to the bulk value. Also, the spin relaxation time is connected to the optical dephasing time via $\tau_s = 2\ \grave{T}_2$. Thus, even if the excitons are confined in the growth direction of the QW, they are sensitive to scattering events when they propagate in the QW plane. The spin orientation is then lost in a few picoseconds as confirmed by the time evolution of the circular degree of polarization.

Because the dynamics of the $\Delta R/R$ circular degree of polarization is independent of the excitation intensity, we can exclude exciton-exciton scattering from the list of the possible dephasing processes that can be responsible for the spin relaxation. We have explained this fact by introducing a thermalization process where the exciton kinetic energy does not depend on the total number of photocreated excitons.

We have shown that increasing temperature enhances the spin relaxation. The spin-relaxation time follows an activation law that implies an escape energy $\Delta E = 56.5$ eV. It shows that excitons are dephased and loose their optical orientation mainly through delocalization into the AlGaN barrier However, compared to bulk GaN the optical orientation is preserved up to 100 K. Therefore, moving toward GaN/AlGaN QWs with a similar optical quality, in terms of linewidth, but with higher Al content could allow both decreasing the spin relaxation rate and potentially preserving the optical orientation up to room temperature.

References

References

[Brimont09] C. Brimont, M. Gallart, A. Gadalla, O. Crégut, B. Hönerlage, and P. Gilliot, *J. Appl. Phys.* **105**, 023502 (2009).

[Fano61] U. Fano, *Phys. Rev.* **124**, 1866 (1961).

[Gadalla10] A. Gadalla, O. Crégut, M. Gallart, B. Hönerlage, J.-B. Beaufrand, M. Bowen, S. Boukari, E. Beaurepaire, and P. Gilliot, *J. Phys. Chem. C* **114**, 4086 (2010).

[Gadalla10a] A. Gadalla, J.-B. Beaufrand, M. Bowen, S. Boukari, E. Beaurepaire, O. Crégut, M. Gallart, B. Hönerlage, P. Gilliot, submitted to *J. Phys. Chem. C* (Accepted September 2010).

[Gadalla10b] A. Gadalla J. Besbas, M. Gallart, O. Crégut, B. Hönerlage, P. Gilliot, submitted to *Phys. Rev. B* (2010).

[Mi03] J. Mi, L. Guo, Y. Liu, W. Liu, G. You, S. Qian, *J. Phys. Lett. A* **310**, 486 (2003).

[Soleimani04] H. R. Soleimani, S. Cronenberger, O, Crégut, J.-P. Likforman, M. Gallart, T. Ostatnicky, P. Gilliot, and B. Hönerlage, *Appl. Phys. Lett.* **85**, 5263 (2004).

[Stokker08] F. Stokker-Cheregi, A. Vinattieri, E. Feltin, D. Simeonov, J.-F. Carlin, R. Butté, N. Grandjean, and M. Gurioli, *Phys. Rev. B* **77**, 125342 (2008).

[Zhou04] J. Zhou, J. Mi, B. Li, S. Qian, *J. Opt. Mater.* ***27***, 377 (2004).

(CH1)

[Brimont08] C. Brimont, M. Gallart, O. Crégut, B. Hönerlage, and P. Gilliot, *Phys. Rev. B* **77**, 125201 (2008).

[Brown08] J. Brown, J.-P. R. Wells, D. O. Kundys, A. M. Fox, T. Wang, P. J. Parbrook, D. J. Mowbray, and M. S. Skolnick, J. Appl. Phys. **104**, 053523 (2008).

[Collet00] J. Collet, O. Tharaud, A. Chapoton, D. Vuillaume, *Appl. Phys. Lett.* **76**, 1941 (2000).

[Collier00] C. P. Collier, G. Mattersteig, E. W. Wong, Y. Luo, K. Beverly, J. Sampaio, F. M. Raymo, J. F. Stoddart, J. R. Heath, *Science*. **289**, 1172 (2000).

[Dimitra02] C.D. Dimitrakopoulos, P.R.L. Malenfant, *Adv. Mater.* **14**, 99 (2002).

[Gould01] R. D. Gould, N. A. Ibrahim, *Thin Solid Films* **398–399**, 432 (2001).

[Harutyunyan95] A. R. Harutyunyan, *Chem. Phys. Lett.* **246**, 615 (1995).

[Harutyunyan99] A. R. Harutyunyan, A. A. Kuznetsov, O. A. Kuznetsov, O. L. Kaliya, *J. Magn. Mater*. **194**, 16 (1999).

[Iacovita08] C. Iacovita, M. V. Rastei, B. W. Heinrich, T. Brumme, J. Kortus, L. Limot, J. P. Bucher, *Phys. Rev. Lett.* **101**, 116602 (2008).

[Ishiguro07] T. Ishiguro, Y. Toda, and S. Adachi, *Appl. Phys. Lett.* **90**, 011904 (2007)

[Kornilovich01] P. E. Kornilovich, A. M. Bratkovski, *Phys. Rev. B.* **64**, 195413 (2001).

[Mckeown98] N. B. Mckeown, *Phthalocyanine Materials: Synthesis, Structure, and Function*, Cambridge University Press, United Kingdom (1998).

[Miller06] K. A. Miller, R. D. Yang, M. J. Hale, J. Park, B. Fruhberger, C. N. Colesniuc, I. K. Schuller, A. C. Kummel and W. C. Trogler, *J. Phys. Chem. B* **110**, 361 (2006).

[Prince01] B. J. Prince, B. E. Williamson, R. J. Reeves, *J. Lumin*. **93**, 293 (2001).

[Ribeiro00] A. O. Ribeiro, J. C. Biazzotto, O. A. Serra, *J. Non-Cryst. Solids* **273**, 198 (2000).

[Stewart04] D. R. Stewart, D. A. A. Ohlberg, P. A. Beck, Y. Chen, R. S. Williams, J. O. Jeppesen, K. A. Nielsen, J. F. Stoddart, *Nano. Letters*. **4**, 133 (2004).

[Stokker09] F. Stokker-Cheregi, A. Vinattieri, E. Feltin, D. Simeonov, J.-F. Carlin, R. Butté, N. Grandjean, F. Sacconi, M. Povolotskyi, A. Di Carlo, M. Gurioli, *Phys. Rev. B* **79**, 245316 (2009)

[Tang86] C.W. Tang, *Appl. Phys. Lett.* **48**, 183 (1986).

[Tang87] C. W. Tang and S. A. VanSlyke, *Appl. Phys. Lett.* **51**, 913 (1987).

[Venugopal02] S. Venugopal Rao, D. Narayana Rao, *J. Porphyrins Phthalocyanines*, **6**, 233 (2002).

[Zhou01] X. Zhou, M. Pfeiffer, J. Blochwitz, A. Werner, A. Nollau, T. Fritz, K. Leo, *Appl. Phys. Lett.* **78**, 410 (2001).

[Zhou02] X. Zhou, M. Pfeiffer, J. S. Huang, J. Blochwitz-Nimoth, D. S. Qin, A. Werner, J. Drechsel, B. Mannig, K. Leo, *Appl. Phys. Lett.* **81**, 922 (2002).

[Stokker08] F. Stokker-Cheregi, A. Vinattieri, E. Feltin, D. Simeonov, J.-F. Carlin, R. Butté, N. Grandjean, and M. Gurioli, *Phys. Rev. B* **77**, 125342 (2008)

(CH2)

[Alfredsson05] Y. Alfredsson, B. Brena, K. Nilson, J. Åhlund, L. Kjeldgaard, M. Nyberg, Y. Luo, N. Mårtensson, A. Sandell, C. Puglia, H. Siegbahn, *J. Chem. Phys.* **122**, 214723 (2005).

[Ashcroft76] N. W. Ashcroft and N. D. Mermin, *Solid State Physics*, Saunders College Publishing (1976).

[Bir72] G. L. Bir and W. Kohn. *Symmetry and Strain-Induced Effects in Semiconductors*. Wiley, (1972).

[Bir76] G. L. Bir, A. G. Aronov, and G. E. Pikus. *Sov. Phys. JETP* **42**, 705 (1976).

[Cho76] K. Cho, *Physical Review B* **14**, 4463 (1976).

[Dietl08] T. Dietl, W. Dobrowolski, E. C. Fernandes da Silva, B. Hönerlage, B. K. Meyer, U. Rössler and T. Story, *Semiconductors*,Vol **44**, Springer-Verlag Berlin Heildelberg, (2008).

[Dufour94] G. Dufour, C. Poncey, F. Rochet, H. Roulet, M. Sacchi, M. D. Santis, and M. D. Crescenzi, *Surf. Sci.* **319**, 251 (1994).

[Dyakonov04] M. I. D'yakonov, *Spintronics*, *LANL e-print archive, Cond.-Mat.*, 0401369 (2004).

[D'yakonov71] M. I. D'yakonov and V. I. Perel. *Sov. Phys. JETP* **33**,1053 (1971).

[Edgar94] J. H. Edgar, *Properties of Group III Nitrides (Electronic Materials Information Service (EMIS)*, London, (1994).

[Elliott54] R. J. Elliott. *Phys. Rev.* **96**, 266 (1954).

[Fabian99] J. Fabian and S. Das Sarma. *J. Vac. Sci. Technol. B* **17**, 1708 (1999).

[Frenkel31] J. Frenkel, *Phys. Rev.* **37**, 17 (1931).

[Ibach03] H. Ibach and H. Lueth. *Solid-State Physics*. Springer Verlag, (2003).

[Ishiguro07] T. Ishiguro, Y. Toda and S. Adachi, *Appl. Phys. Lett.* **90**, 011904 (2007).

[Iwatsu88] F. Iwatsu, *J. Phy. Chem.* **92**, 1678 (1988).

[Klingshirn97] C. F. Klingshirn. *Semiconductor Optics*. Springer, Berlin, (1997).

[Knox63] R. S. Knox. *Theory of excitons*. Academic Press New York, (1963).

[Kuroda04] T. Kuroda, T. Yabushita, T. Kosuge, A. Tackeuchi, K. Taniguchi, T. Chinone, and N. Horio, *Appl. Phys. Lett.* **85**, 3116 (2004).

[Lagarde08] D. Lagarde, A. Balocchi, H. Carrère, P. Renucci, T. Amand, X. Marie, S. Founta, and H. Mariette, *Phys. Rev. B* **77**, 041304 (2008).

[Leznoff89] C. C. Leznoff and A. B. P. Lever, "*Phthalocyanines: Properties and Applications*", Vol-I, New York, NY (1989).

[Liao01] M.-S. Liao, S. Scheiner, *J. Chem. Phys.* **114**, 9780 (2001).

[Long68] D. Long. *Energy Bands in Semiconductors*. John Wiley and Sons, INC., (1968).

[Luttinger55] J. M. Luttinger and W. Kohn. Motion of electrons and holes in perturbed periodic fields. *Phys. Rev.*, **97**, 869 (1955).

[Majewski96] J. A. Majewski, M. Städele, and P. Vogel, *MRS Internet Journal of Nitride Semiconductor Research*, Vol. **1**, Article No. 1, (1996).

[Meier84] F. Meier and B. P. Zakharchenya. *Optical orientation modern problems in condensed matter sciences*. North-Holland, (1984).

[Mizugushi95] J. Mizugushi, G. Rihs, and H. R. Karfunkel, *J. Phys. Chem.* **99**, 16217 (1995).

[Mohammed92] S. N. Mohammed, A. A. Salvador, and Hadis Morkoç, *J. Vac. Sci. Technol.* **B10**, 1237 (1992).

[Orti92] E. Orti, J.-L. Brédas, *J. Am. Chem. Soc.* **114**, 8669 (1992).

[Otake06] H. Otake, T. Kuroda, T. Fujita, T. Ushiyama, A. Tackeuchi, T. Chinone, J.-H. Liang, and M. Kajikawa, *Appl. Phys. Lett.* **89**, 182110 (2006).

[Ottaviano97] L. Ottaviano, S. D. Nardo, L. Lozzi, M. Passacanttando, P. Ricozzi, and S. Santucci, *Surf. Sci.* **373**, 318 (1997).

[Petalas95] J. Petalas , S. Logothetidis, and S. Boultadakis, M. Alouni, J. M. Wills, *Phys. Rev. B* **52**, 8082 (1995).

[Shah96] J. Shah, *Ultrafast spectroscopy of Semiconductors and Semiconductor Nanostructures*, Springer-Berlin, (1996).

[Stokker08a] F. Stokker-Cheregi, A. Vinattieri, E. Feltin, D. Simeonov, J. Levrat, J.-F. Carlin, R. Butté, N. Grandjean, and M. Gurioli, *Appl. Phys. Lett.* **93**, 152105 (2008).

[Suzuki95] M. Suzuki, T. Uenoyama, and A. Yanase, *Physical Review B* **52**, 8132 (1995).

[Tackeuchi06] A. Tackeuchi, H. Otake, Y. Ogawa, T. Ushiyama, T. Fujita, F. Takano, and H. Akinaga, *Appl. Phys. Lett.* **88**, 162114 (2006).

[Vainshtien82] B. K. Vainshtien, *Structure of Crystals*, Springer, Berlin, (1982).

[Wagner82] H. Wagner, R. Loutfy, C-K. Hsiao, *Journal of materials science* **17**, 2781 (1982).

[Wannier37] G. H. Wannier. The structure of electronic excitation levels in insulating crystals. *Phys. Rev.* **52**,191 (1937).

[Yeh94] C.-Y. Yeh, S.-H. Wei, and A. Zunger, *Phys. Rev. B* **50**, 2715 (1994).

[Zutic04] I. Zutic, J. Fabian, S. Das Sarma. *Rev.Mod. Phys.* **76**, 323 (2004).

(CH4)

[Antipas83] A. Antipas, M. Gouterman, *J. Am. Chem. Soc.* **105**, 4896 (1983).

[Brimont08] C. Brimont, M. Gallart, O. Crégut, B. Hönerlage, and P. Gilliot, *Phys. Rev. B* **77**, 125201 (2008).

[Chau93] L. K. Chau, C. D. England, S. Chen, N. R. Armstrong, *J. Phys. Chem.* **97**, 2699 (1993).

[Chung01] S. J. Chung, T. C. Lin, K. S. Kim, J. Swiatkiewicz, P. N. Prasad, G. A. Baker, F. V. Bright, *Chem. Mater.* **13**, 4071 (2001).

[Davidson82] A. T. Davidson, *J. Chem. Phys.* **77**, 168 (1982).

[Derkowska07] B. Derkowska, M. Wojdyla, R. Czaplicki, W. Bala, B. Sahraoui, *Optics Commun.* **274**, 206 (2007).

[El-Nahas08] M. M. El-Nahass, A. A. Atta, H. E. A. El-Sayed, E. F. M. El-Zaidia, *Appl. Surf. Sci.* **254**, 2458 (2008).

[Endo99] A. Endo, S. Matsumoto, J. Mizuguchi, *J. Phys. Chem. A* **103**, 8193 (1999).

[Fano61] U. Fano, *Phys. Rev.* **124**, 1866 (1961).

[Farag07] A. A. M. Farag, *Opt. Laser Technol.* **39**, 728 (2007).

[Gadalla10] A. Gadalla, O. Crégut, M. Gallart, B. Hönerlage, J.-B. Beaufrand, M. Bowen, S. Boukari, E. Beaurepaire, and P. Gilliot, *J. Phys. Chem. C* **114**, 4086 (2010).

[Gadalla10a] A. Gadalla, J.-B. Beaufrand, M. Bowen, S. Boukari, E. Beaurepaire, O. Crégut, M. Gallart, B. Hönerlage, P. Gilliot, submitted to *J. Phys. Chem. C* (2010).

[Gulbinas96] V. Gulbinas, M. Chachisvilis, L. Valkunas, V. Sundström, *J. Phys. Chem.* **100**, 2213 (1996).

[Heutz00] S. Heutz, S. M. Bayliss, R. L. Middleton, G. Rumbles, T. S. Jones, *J. Phys. Chem. B* **104**, 7124 (2000).

[Hirasawa04] M. Hirasawa, Y. Sakazaki, H. Hane, T. Kobayashi, *Chem. Phys. Lett.* **392**, 390 (2004).

[Hirasawa04] M. Hirasawa, Y. Sakazaki, H. Hane, and T. Kobayashi, *Chem. Phys. Lett.* **392**, 390 (2004).

[Joffre88] M. Joffre, D. Hulin, A. Migus, A. Antonetti, C. Benoit à la Guillaume, N. Peyghambarian, M. Lindberg, and S. W. Koch, *Opt. Lett.* **13**, 276 (1988).

[Joseph08] B. Joseph, C. S. Menon, *E. J. Chem.* **5**, 86 (2008).

[Karasek52] F. W. Karasek, J. C. Decius, *J . Am. Chem. Soc.* **74**, 4716 (1952).

[Kobayashi04] T. Kobayashi M. Hirasawa, Y. Sakazaki, and H. Hane, *Chem. Phys. Lett.* **400**, 301 (2004).

[Kobayashi04] T. Kobayashi, M. Hirasawa, Y. Sakazaki, H. Hane, *Chem. Phys. Lett.* **400**, 301 (2004).

[Kroner08] M. Kroner, A. O. Govorov, S. Remi, *Nature* **451**, 311 (2008).

[Lehn85] J. M. Lehn, Ch. W. Rees, *Molecular Semiconductor*, Springer-Verlag Berlin Heildelberg, P73 (1985).

[Leznoff89] C. C. Leznoff and A. B. P. Lever, "*Phthalocyanines: Properties and Applications*", Vol-I, New York, NY (1989).

[Liao01] M.-S. Liao, S. Scheiner, *J. Chem. Phys.* **114**, 9780 (2001).

[Liu08] G. Liu, T. Gredig, I. K. Schuller, *EPL* **83**, 56001P1(2008) .

[Ma61] G. Ma, J. He, C. H. Kang, S. H. Tang, *Chem. Phys. Lett.* **370**, 293 (2003).

[Mi03] J. Mi, L. Guo, Y. Liu, W. Liu, G. You, S. Qian, *J. Phys. Lett. A* **310**, 486 (2003).

[Mizuguchi95] J. Mizuguchi, G. Ribs, H. R. Karfunkel, *J. Phys. Chem.* **99**, 16217 (1995).

[Mizuguchi99] J. Mizuguchi, S. Matsumoto, *J. Phys. Chem. A* **103**, 614 (1999).

[Nikolaitchik99] A. V. Nikolaitchik, O. Korth, M. A. J. Rodgers, *J. Phys. Chem. A* ***103***, 7587 (1999); O. Nikolaitchik, M. A. J. Rodgers, *J. Phys. Chem. A* ***103***, 7597 (1999).

[Saito93] T. Saito, W. Sisk, T. Kobayashi, S. Suzuki, T. Iwayanagi, *J. Phys. Chem.* **97**, 8026 (1993).

[Schell98] J. Schell, D. Ohlmann, D. Brinkmann, R. Lévy, M. Joucla, J. L. Rehspringer, and B. Hönerlage, *J. Chem. Phys.* **108**, 8599 (1998); J. Schell, D. Brinkmann, D.

Ohlmann, B. Hönerlage, R. Lévy, M. Joucla, J. L. Rehspringer, J. Serughetti, and C. Bovier, *J. Chem. Phys.* **111**, 5929 (1999).

[Shihub93] S. I. Shihub, Gould, R. D. *Phys. Stat. Sol. (a)* **139**, 129 (1993).

[Sturge70] M. D. Sturge, H. J. Guggenheim, M. H. L. Pryce, *Phys. Rev. B* **2**, 2459 (1970).

[Tait83] C. D. Tait, D. Holten, *Chem. Phys. Lett.* **100**, 268 (1983).

[Terasaki92] A. Terasaki, M. Hosoda, T. Wada, H. Tada, A. Koma, A. Yamada, H. Sasabe, A. F. Garito, T. Kobayashi, *J. Phys. Chem.* **96**, 10534 (1992).

[Tian98] M. Tian, S. Yanagi, K. Sasaki, T. Wada, H. J. Sasabe, *Opt. Soc. Am. B* **15**, 846 (1998).

[Williams92]V. S. Williams, S. Mazumdar, N. R. Armstrong, Z. Z. Ho and N. Peyghambarian, *J. Phys. Chem.* **96**, 4500 (1992).

[Yan06] Y. Yan, S. Lu, R. Zhu, J. Zhou, S. Wei, S. Qian, *J. Phys. Chem. A* **110**, 10757 (2006).

[Yim02] S. Yim, S. Heutz, and T. S. Jones, *J. Appl. Phys.* **91**, 810 (2002).

[Yoshida86] H. Yoshida, Y. Tokura, Y. Koda, *Chem. Phys.***109**, 375 (1986).

[Zhang06] W. Zhang, A. O. Govorov, G. W. Bryant, *Phys. Rev. Lett.* **97**, 146804 (2006).

[Zhou04] J. Zhou, J. Mi, B. Li, S. Qian, *J. Opt. Mater*. ***27***, 377 (2004).

[Zhou97] H. Zhou, S. G. Boxer, *J. Phys. Chem. B* **101**, 5759 (1997).

(CH5)

[Andreani90] L. C. Andreani and F. Bassani, *Phys. Rev. B* **41**, 7536 (1990).

[Aoki99] T. Aoki, G. Mohs, M. Kuwata-Gonokami, and A. A. Yamaguchi, *Phys. Rev. Lett.* **82**, 3108 (1999).

[Brimont08] C. Brimont, M. Gallart, O. Crégut, B. Hönerlage, and P. Gilliot, *Phys. Rev. B* **77**, 125201 (2008).

[Brimont09] C. Brimont, M. Gallart, O. Crégut, B. Hönerlage, P. Gilliot, D. Lagarde, A. Balocchi, T. Amand, X. Marie, S. Founta, and H. Mariette, *J. Appl. Phys.* **106**, 053514 (2009).

[Brimont09a] C. Brimont, M. Gallart, A. Gadalla, O. Crégut, B. Hönerlage, and P. Gilliot, *J. Appl. Phys.* **105**, 023502 (2009).

[Brown08] J. Brown, J.-P. R. Wells, D. O. Kundys, A. M. Fox, T. Wang, P. J. Parbrook, D. J. Mowbray, and M. S. Skolnick, *J. Appl. Phys.* **104**, 053523 (2008).

[Chen88] Y. Chen, B. Gil, P. Lefebvre, and H. Mathieu, *Phys. Rev. B* **37**, 6429 (1988).

[Feltin07] E. Feltin, D. Simeonov, J.-F. Carlin, R. Butté, and N. Grandjean, *Appl. Phys. Lett.* **90**, 021905 (2007).

[Fischer97] A. J. Fischer, W. Shan, G. H. Park, J. J. Song, D. S. Kim, D. S. Yee, R. Horning, and B. Goldenberg, *Phys. Rev. B* **56**, 1077 (1997).

[Gourley82] P. L. Gourley and J. P. Wolfe, Phys. Rev. B **25**, 6338 (1982).

[Haag99] H. Haag, B. Hönerlage, O. Briot and R. L. Aulombard, *Phys. Rev. B* **60**, 11624 (1999); H. Haag, P. Gilliot, R. Lévy, B. Hönerlage, O. Briot, S. Ruffenach-Clur, and R. L. Aulombard, *Appl. Phys. Lett.* **74**, 1436 (1999).

[Jena04] D. Jena, *Phys. Rev.* **70**, 245203 (2004).

[Maialle93] M. Z. Maialle, E. A. de Andrada e Silva, and L. J. Sham, *Phys. Rev. B* **47**, 15776 (1993).

[Martin06] D. Martin, J. Napierala, M. Ilegems, R. Butté, and N. Grandjean, *Appl. Phys. Lett.* **88**, 241914 (2006).

[Pau97] S. Pau, J. Kuhl, F. Scholz, V. Haerle, M. A. Khan, and C. J. Sun, *Phys. Rev. B* **56**, R12 718 (1997).

[Pau98] S. Pau, J. Kuhl, F. Scholz, V. Haerle, M. A. Khan, and C. J. Sun, *Appl. Phys. Lett.* **72**, 557 (1998).

[Shah96] J. Shah, *Ultrafast spectroscopy of Semiconductors and Semiconductor Nanostructures*, Springer-Berlin, (1996).

[Soleimani04] H. R. Soleimani, S. Cronenberger, O. Crégut, J.-P. Likforman, M. Gallart, T. Ostatnický, P. Gilliot, and B. Hönerlage, *Appl. Phys. Lett.* **85**, 5263 (2004).

[Soleimani05] H. R. Soleimani, S. Cronenberger, M. Gallart, P. Gilliot, J. Cibert, O. Crégut, B. Hönerlage, and J. P. Likforman, *Appl. Phys. Lett.* **87**, 192104 (2005).

[Stokker08] F. Stokker-Cheregi, A. Vinattieri, E. Feltin, D. Simeonov, J.-F. Carlin, R. Butté, N. Grandjean, and M. Gurioli, *Phys. Rev. B* **77**, 125342 (2008).

[Stokker09] F. Stokker-Cheregi, A. Vinattieri, E. Feltin, D. Simeonov, J.-F. Carlin, R. Butté, N. Grandjean, F. Sacconi, M. Povolotskyi, A. Di Carlo, M. Gurioli, *J. Phys. Rev. B* **79**, 245316 (2009).

[Tackeushi90] A. Tackeushi, S. Muto, T. Inata and T. Fujii, Appl. Phys. Lett. **56**, 2213 (1990); Ph. Roussignol, P. Rolland, R. Ferreira, C. Delalande, G. Bastard, A. Vinattieri, L. Carraresi, M. Colocci and B. Etienne, *Surf. Sci.* **267**, 360 (1992); T. C. Damen, K. Leo, J. Shah and J. E. Cunningham, *Appl. Phys. Lett.* **58**, 1902 (1991); A. Vinattieri, J. Shah, T. C. Damen, D. S. Kim, L. N. Pfeiffer, M. Z. Maialle, and L. J. Sham, *Phys. Rev. B* **50**, 10868 (1994).

[Vinattieri94] A. Vinattieri, Jagdeep Shah, T. C. Damen, and D. S. Kim, L. N. Pfeiffer, M. Z. Maialle and L. J. Sham, *Phys. Rev. B* **50**, 10868 (1994).

[Yamada04] Y. Yamada, Y. Ueki, K. Nakamura, T. Taguchi, *Appl. Phys. Lett.* **84**, 2082 (2004).

[Zimmermann97] R. Zimmermann, A. Euteneuer, J. Möbius, D. Weber, M.R. Hofmann, W.W. Rühle, E.O. Göbel, B.K. Meyer, H. Amano, and I. Akasaki, *Phys. Rev. B* **56**, R12 722 (1997).

(CH6)

[Chung01] S. J. Chung, T. C. Lin, K. S. Kim, J. Swiatkiewicz, P. N. Prasad, G. A. Baker, F. V. Bright, *Chem. Mater.* **13**, 4071 (2001).

[Derkowska07] B. Derkowska, M. Wojdyla, R. Czaplicki, W. Bala, B. Sahraoui, *Optics Commun.* **274**, 206 (2007).

[Liao01] M.-S. Liao, S. Scheiner, *J. Chem. Phys.* **114**, 9780 (2001).

[Tait83] C. D. Tait, D. Holten, *Chem. Phys. Lett.* **100**, 268 (1983).

[Yan06] Y. Yan, S. Lu, R. Zhu, J. Zhou, S. Wei, S. Qian, *J. Phys. Chem. A* **110**, 10757 (2006).

List of ……..

+ Abbreviations

+ Figures

+Tables

List of Abbreviations

A	Contributions of the exponential decay
AFM	Atomic Force Microscopy
AlGaN	Aluminium Gallium Nitride
BBO	Beta Barium Borate
BX	Biexciton
C	Constant for long time delay
CB	Conduction Band
CCD	Charge Coupled Device
CoPc	Cobalt Phthalocyanine
CT	Charge Transfer
CTE	Charge-transfer excitons
d_{hkl}	Lattice spacing
DE	Delocalized Exciton
DT	Normalized Differential Transmission
DTS	Differential Transmission Spectrum
e	Electron
ED	Electron Diffraction
f	Focal length
F	Shift of the resonance position
F_{OSC}	Exciton Oscillator Strength
fs	Femtosecond
FT	Fourier Transform
FWHM	Full Width at Half Maximum
GaN	Gallium Nitride
GVD	Group Velocity Dispersion
h	Planck’s constant
H_2Pc	Hydrogen Phthalocyanine
HF	Hydrofluoric
HH	Heavy Hole
HH_1	First Heavy Hole Excitons
HOMO	Highest Occupied Molecular Orbital

K	Kelvin
$\mathbf{k}$	Wavevector
$\boldsymbol{K}$	Exciton center of mass
$\mathrm{k_B}$	Boltzmann constant
kHz	killohertz
L	Well width
LBO	Lithium Triborate
LH	Light Hole
$\mathrm{LH_1}$	First Light Hole Excitons
LO	Longitudinal optical
LUMO	Lowest Unoccupied Molecular Orbital
MHz	Megahertz
meV	millielectron Volt
MLCT	Metal Ligand Charge Transfer
MO’s	Molecular Orbitals
MOVPE	Metal Organic Vapor Phase Epitaxy
MPcs	Metal Phthalocyanines
n_0	Initial exciton population
nm	Nanometer
OMC	Organic Molecular Crystal
OPA	Optical Parametric Amplifier
$\mathrm{P_0}$	Average power
$\mathrm{P_c}$	Circular polarization rate
Pc	Phthalocyanine
PDT	Photo Dynamic Therapy
PL	Photoluminescence
PLE	Photoluminescence excitation
ps	picosecond
q	Fano asymmetry factor
QW	Quantum Wells
$R(\omega)$	Reflectivity
RegA	Regenerative Amplifier
S_0	Singlet ground state
S_1^0	First excited optically active state

S_2	Second excited optically active state
SEM	Scanning Electron Microscope
SHG	Second Harmonic Generation
S_z	Electron angular momentum
t	Time
T	Temperature
T	Transmission
$\grave{T}$	Dephasing time
T_0	Permanent long-lived state
T_1	Higher energy triplet states
$\mathrm{T_D}$	Debye Temperature
TEM	Transmission Electron Microscope
Ti: Sa	Titanium: Sapphire
TR-PL	Time Resolved-Photoluminescence
UHV	Ultra High Vacuum
UV	Ultraviolet
VB	Valence Band
vdW	van der Waals
Vis	Visible
X	Exciton
$\mathrm{X_A}$	A- excitons
$\mathrm{X_B}$	B- excitons
XRD	X-Ray Diffraction
A	Absorption coefficient
α-	Alpha Phase
β-	Beta Phase
$\mathit{\Gamma}$	Damping constant
δ	Coherence length
Δ_{Cr}	Crystal field
$\Delta R/R$	Differential reflectivity
Δ_{SO}	Split-off
Δt	Time delay
$\mathit{\Delta} T/T$	Differential Transmission
έ	Photon energy of the probe photons

θ_B	Scattering Angle
λ	Wavelength
μ	Reduced mass
σ^-	Left circular polarized light
σ^+	Right circular polarized light
τ_c	Correlation time
ω_0	Resonance frequency
ΔE	Thermal Activation Energy
Ω	Precession frequency
τ_e	Electron spin relaxation time
τ_h	Hole spin relaxation time
τ_s	Exciton spin relaxation time
$\tilde{n}$	Complex index of refraction
ε	Dielectric constant
τ^A_{e+-}	Electron transition rate
τ^A_X	Exciton spin-relaxation rate
τ^A_{h+-}	Hole transition rate
τ^{NR}	Non-radiative recombination time
$n_{\lvert\pm 1>}$	Population of the excitonic level of spin $\lvert\pm 1>$
τ^R	Radiative recombination time
τ_A	Recombination time
E_φ	Resonance photon energy of the probe photons
R_y^*	Rydberg energy
J_z^h	Total hole angular momentum on to the *z*- axis
ε_0	Vacuum permittivity
$\lvert 0 >$	Zero Level
Φ	Tilt angle

List of Figures

Fig. 2.1 *Molecular structure of* (a) H_2Pc *and* (b) CoPc……………………………………7

Fig. 2.2 *Orbital energy levels for outer orbitals in different metallophthalocyanines*………9

Fig. 2.3. S*ublimation system setup and temperature distribution along the heated tube*…...10

Fig. 2.4. *Schematic diagram of the thermal evaporation technique*…………………………11

Fig. 2.5. (a) *Basic principle of the AFM technique* (b) *Schematic diagram showing the force between the tip and the sample and the regions used for different operating AFM modes*…13

Fig.2.6. *Energy gap of different compound s.c. as a function of lattice constant*..…………15

Fig. 2.7. *Crystallographic structure of* (a) *Zinc Blende and* (b) *Wurtzite*……..………….. 16

Fig. 2.8. *View from above of the first two layers in a stack of cannonballs. The first layer is arranged in a plane triangular lattice. Balls in the second layer are placed above alternate interstices in the first. The resulting structure will be close-packed hexagonal for inset (a) and face centered cubic for inset (b)*…………………………………………………….. 16

Fig. 2.9. *Band structure and symmetry of the valence band of cubic GaN at Γ- point*……...17

Fig. 2.10. *Band structure and symmetry of the valence band of hexagonal GaN at Γ-point*..18

Fig. 2.11. *A pair excitation in the scheme of valence and conduction band* (a) *and in the exciton picture of a direct band gap semiconductor* (b) ………………………………....21

Fig. 2.12 *A single quantum well* (a) *and energy level of an idealized quantum well* (b).…...23

Fig. 2.13. *Fine structure for HH-exciton states in a quantum well*……………………........25

Fig. 2.14. *Optical selection rule in hexagonal GaN*……………………………….........25

Fig. 2.15. *Reflectivity spectra with and without the pump pulses (a) and the differential reflectivity (b) as a function of photon energy for a given polarization of the probe pulses*..28

Fig. 3.1. *The different components of the Ti:Sapphire laser source*……………….............35

Fig. 3.2. *Optical scheme of the regenerative amplifier (RegA 9000)*……………….............37

Fig. 3.3. *Optical scheme of the optical parametric amplifier (OPA)* …………….............38

Fig. 3.4. *Two prisms Compensator for positive GVD*……………………………….............39

Fig. 3.5. *Schematic setup of an autocorrelation technique for measuring the pulse duration. Beams* $\mathbf{k_1}$ *and* $\mathbf{k_2}$ *are focused on a second-harmonic generating crystal like BBO with a variable time delay*……………………………………………………………………..41

Fig. 3.6a. *Autocorrelation signal of femtosecond laser pulses. The measured pulse duration is 66 fs*……………………………………………………………………………………42

Fig. 3.6b. *Spectral characterization of the femtosecond laser pulses. The spectral width (FWHM) of the pulses is 26.7 meV*…………………………………………………………42

Fig. 3.7. *The vacuum loading Microstat He cryostat*……………………………………..43

Fig. 3.8. *Scheme of the setup used in photoluminescence excitation experiment*…………...44

Fig. 3.9. *Optical setup of the temporally and spectrally resolved pump-probe experiment by measuring differential transmission of phthalocyanine films*………………………………45

Fig. 3.10. *Optical setup of the temporally and spectrally resolved pump-probe experiment, measuring differential reflectivity of a GaN/AlGaN quantum well*…………………………47

Fig. 4.1. *Crystal structures of α- and β- phase:* (a) *Schematic of α- and β -H_2Pc molecules projected on the (100) and (001) planes, respectively.* (b) *Schematic of the unit cells and molecular arrangement of α- and β -H_2Pc*…………………………………………………50

Fig. 4.2. *X-ray diffraction pattern of H_2Pc (blue line) and CoPc (red line) thin films*……...51

Fig. 4.3. *Scanning electron micrograph of (a) H_2Pc and (b) CoPc thin films of the same thickness ~ 170 nm*……………………………………………………………………..52

Fig. 4.4. *Tapping-mode AFM images of* (a) *H_2Pc and* (b) *CoPc films and their 3D images of the same thickness ~ 170 nm*…………………………………………………………...53

Fig. 4.5. *Electron diffraction patterns of* (a) *H_2Pc and* (b) *CoPc films*……………………..53

Fig. 4.6. *Absorption and reflection spectra of H_2Pc* (a) *and CoPc* (b) *films in the ultraviolet and visible regions*……………………………………………………………………..54

Fig. 4.7. *Absorption spectra of H_2Pc* (a) *and CoPc* (b) *films in the ultraviolet and visible regions. The Q-bands are adjusted using three Gaussian peaks*……………………………55

Fig. 4.8. *Absorption spectra in the Q-band region of* (a) *H_2Pc and* (b) *CoPc in solution compared to that of thin films*……………………………………………………………56

Fig. 4.9. *The bleaching dynamics of H_2Pc thin film*………………………………………...58

Fig. 4.10. *The bleaching dynamics of H_2Pc and CoPc films determined from degenerate pump-probe measurements at 2.066 eV with the pump intensity of 6.54 GW/cm^2*……….....59

Fig. 4.11. *Excitation intensity dependence of bleaching dynamics of CoPc film at 2.066 eV (600 nm)* ……………………………………………………………………………….60

Fig. 4.12. *Peak signal intensity as a function of the excitation intensity for CoPc film*…….60

Fig. 4.13. *Differential transmission of* (a) *H_2Pc and* (b) *CoPc films as a function of the time delay between the pulses and as a function of the photon energy of the transmitted light for the spectrometer centered at 2.254 eV. The photon energy of the exciting pump pulses is 2.032 eV*…………………………………………………………………………………...62

Fig. 4.14a(b). *Spectral (temporal) variation of the differential transmission rate $\Delta T(t)/T$ of metal-free H_2Pc for several time delays (probe photon energies) when exciting at a pump photon energy of 1.823 eV*……………………………………………………………..63

Fig. 4.15. *The constant contribution C (*a*) and the dynamical parameters A_1 (b) and t_1 (c) of $\Delta T(t)/T$ curves fitted with Eq. (2) as function of photon energy when exciting at a pump photon energy of 1.823 eV*……………………………………………………………..64

Fig. 4.16a(b). *Spectral (temporal) variation of the differential transmission rate $\Delta T(t)/T$ of metal-free H_2Pc for several time delays (probe photon energies) when exciting at a pump photon energy of 2.032 eV*……………………………………………………………..65

Fig. 4.17. *The constant contribution C (*a*) and the dynamical parameters A_1 (b) and t_1 (c) of $\Delta T(t)/T$ curves fitted with Eq. (2) as function of photon energy when exciting at a pump photon energy of 2.032 eV*……………………………………………………………..66

Fig. 4.18a(b). *Spectral (temporal) variation of the differential transmission rate $\Delta T(t)/T$ of CoPc for several time delays (probe photon energies) when exciting at pump photon energy at 1.823 eV.*…………………………………………………………………………....67

Fig. 4.19. *The constant contribution C (a) and the dynamical parameters (A_1 , t_1) (Figs. b and c) and (A_2 , t_2) (Figs. d and e) of the $\Delta T(t)/T$ curves fitted with Eq. (3) as function of photon energy when exciting at pump photon energy of 1.823 eV*………………………....69

Fig.. 4.20a(b). *Spectral (temporal) variation of the differential transmission rate $\Delta T(t)/T$ of CoPc for several time delays (probe photon energies) when exciting at pump photon energy at 2.032 eV.*…………………………………………………………………………....71

Fig. 4.21. *The constant contribution C (*a*) and the dynamical parameters (A_1 , t_1) (Figs. b and c) and (A_2 , t_2) (Figs. d and e) of the $\Delta T(t)/T$ curves fitted with Eq. (3) as function of photon energy when exciting at pump photon energy of 2.032eV*…………………………......72

Fig. 4.22. *Spectral variation of the differential transmission rate of* (a) *H_2Pc and* (b) *CoPc films probed at different energies of ~ 1.5-2.5 eV. The photon energy of the exciting pump pulses is 2.032 eV*…………………………………………………………………...73

Fig. 4.23. (a) *TheFano absorption for CoPc using a pump at 2.032eV and* (b) *the variation of q with the time delay. The green vertical line shows the central photon energy of the pump pulses.*…………………………………………………………………….............75

Fig. 4.24. *Energy-level model of in* (a) *H_2Pc and* (b) *CoPc describing the induced absorption and induced transmission*……………………………………………………...............76

Fig. 5.1. *Schematic drawing of GaN/AlGaN quantum well structure*……………................85

Fig. 5.2. *Linear reflectivity and photoluminescence (PL) spectra of GaN/AlGaN QW*..........86

Fig. 5.3. *PL Intensity at different excitation intensities of GaN/AlGaN QW when exciting at a photon energy of 3.542 eV at T=4K*…………………………………………………...............87

Fig. 5.4. *The amplitude of the Gaussian fit for the biexciton (BX) as a function of that of the exciton (X) of GaN/AlGaN QW at different excitation intensities. The inset shows the spectral fitting of the X and BX bands in the QW*………………………………….............87

Fig. 5.5. (a) *Emission intensity of GaN/AlGaN QW plotted as a function of excitation photon energy and detection photon energy. The Rayleigh scattering of the excitation source is observed along the diagonal and* (b) *Photoluminescence excitation (PLE) measured at photon energy 3.541 eV*……………………………...89

Fig. 5.6. *Photoluminescence, reflectivity and photoluminescence excitation spectra at low temperature*…………………………..90

Fig. 5.7. *Differential reflectivity as a function of time delay of (a) HH_1, LH_1, and barrier excitons for excitation above the barrier and of (b) HH_1, LH_1 for resonant excitation in the QW at 4K*………………………...91

Fig. 5.8. *Three excitonic levels model*…...92

Fig. 5.9. *Temporal evolution of populations $n_{|+1>}$ and $n_{|-1>}$*...93

Fig. 5.10. *Simple four level model for the exciton dynamics*.. 94

Fig. 5.11. *Biexciton optical selection rules*…...95

Fig. 5.12. *Differential reflectivity spectra covering the GaN buffer layer and the QW regions for co- and counterpolarized configurations of the pump and probe pulses at time delay 0.5 ps (a) and at 7 ps (b)* ………..96

Fig. 5.13. *ΔR/R spectra for co- and counterpolarized configurations of the pump and probe pulses at time delay 0.5 ps* (a) *and at 7 ps* (b) *for HH_1 and LH_1 in the QW at 10K*..............97

Fig. 5.14. *Optical selection rules*…………...97

Fig. 5.15. *Difference between the differential reflectivity at positive time delay of 0.5 ps for the two different probe helicities* (*ΔR/R*)($\sigma^+\sigma^+$) - (*ΔR/R*)($\sigma^+\sigma^-$) *at different pump-probe delay*…………………………………………………………………………………98

Fig. 5.16(a-c). *TR-PL images for GaN/$Al_{0.05}Ga_{0.95}$N QW recorded by the streak camera. The energy of the exciton recombination band (E_x) is indicated in each figure:* (a) *E_x=3.528 eV*, (b) *E_x=3.541 eV and* (c) *E_x=3.558 eV*…...99

Fig. 5.17. *TR-PL spectra measured at short delays relative to the Fig. 5.13. The squares represent the experimental data and the red full lines are the sum of the fitting Gaussian line shapes (dotted lines)* …..99

Fig. 5.18. *Spectrally integrated ΔR/R decays for the three transitions:* HH_1*,* LH_1 *and BX. The circular polarization rate (*P_c*) is also plotted*..103

Fig. 5.19. *Differential reflectivity spectra for selective excitation of* HH_1 *in the QW for co- and counterpolarized configurations at time delay (a) 0.4 ps and at (b) 5 ps*.....................105

Fig. 5.20. *ΔR/R decays and circular polarization rate (*P_c*) for the selective excitation of* HH_1 *in the QW*..105

Fig. 5.21. *Differential reflectivity spectra for different pump intensity from* P_0 *to* $P_0/16$*,* P_0 *corresponds to an average power equal to 600 µW*...106

Fig. 5.22. *Time evolution of the circular polarization rate, at the* HH_1 *exciton energy, for different pump intensities from* P_0 *to* $P_0/16$..107

Fig. 5.23. *ΔR/R decays for the heavy hole exciton (*HH_1*) at different pump intensities from* P_0 *to* $P_0/16$..107

Fig.5.24. *ΔR/R decays for the light hole exciton (*LH_1*) at different pump intensities from* P_0 *to* $P_0/16$..108

Fig.5.25. *Differential reflectivity spectra at different temperatures for co- and counterpolarized configurations of the pump and probe pulses at time delay of 0.5 ps*......109

Fig. 5.26. *Circular polarization rate spectra at different temperatures for* HH_1................110

Fig. 5.27. *Time decay of the polarization rate, at the* HH_1 *exciton energy, as a function of temperature*..110

List of Tables

Table 2.1. *Comparison of values for the fundamental band gap of zinc blende and wurtzite GaN*……………………………………………………………………………..19

Table 4.1. *Interplanar Distance of Molecules for H_2Pc and CoPc Thin Films with the Same Thickness ~ 170 nm*………………………………………………………………..51

Table 4.2. *Parameters of the Decay Process of CoPc at Different Excitation Intensity for a Pump Photon Energy of 2.066 eV*…………………………………………………..61